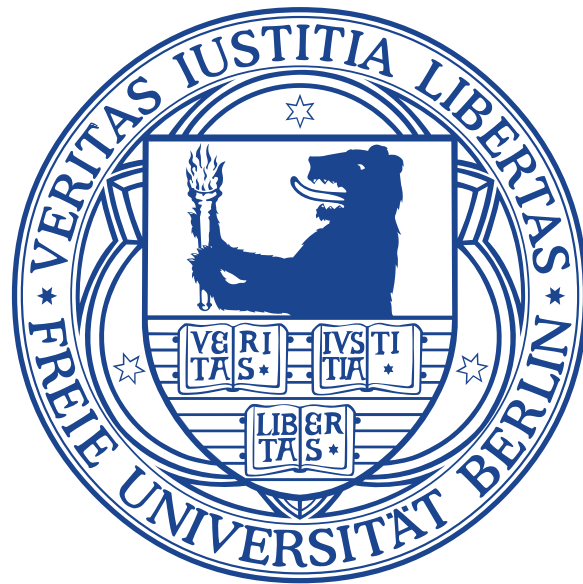


# Low-energy excitations in strongly coupled superconductor-magnet hybrids



## Dissertation

zur Erlangung des Grades eines Doktors  
der Naturwissenschaften (Dr. rer. nat.)

am Fachbereich Physik  
der Freien Universität Berlin

vorgelegt von

Thomas Kiendl

Berlin, 2018

**Erstgutachter:** Prof. Dr. Piet W. Brouwer  
**Zweitgutachter:** Prof. Felix von Oppen, PhD

**Tag der Disputation:** 08. Oktober 2018

## **Selbstständigkeitserklärung**

Hiermit versichere ich, dass ich in meiner Dissertation alle Hilfsmittel und Hilfen angegeben habe, und auf dieser Grundlage die Arbeit selbstständig verfasst habe. Diese Arbeit habe ich nicht schon einmal in einem früheren Promotionsverfahren eingereicht.

Berlin, 04. September 2018



# Kurzfassung

Theoretischer Fortschritt in den letzten zwei Jahrzehnten hat zu einem stark verbessertem Verständnis von Magnet-Supraleiter Hybridstrukturen geführt und hat vielversprechende Anwendungen von diesen Strukturen aufgezeigt. Dazu gehören unter anderem die Speicherung von Quanteninformation oder die Realisierung von Quantenschaltkreisen. Viele Experimente versuchen diese Vorhersagen umzusetzen. Ein Beispiel sind magnetisierte Drähte gekoppelt an einen  $s$ -Wellen Supraleiter, welche einen topologischen Supraleiter realisieren sollen. Signaturen dieser Phase wurden gemessen, allerdings sind diese nicht eindeutig und oft nur in engen Parameterbereichen zugänglich. Naiv erwartet man eine Stabilisierung dieser Phase für eine starke Kopplung zwischen den Materialien. Allerdings kann eine starke Kopplung zu einer nichttrivialen Vermischung von supraleitenden und magnetischen Effekten führen, und ein verbessertes Verständnis der Systeme wird benötigt.

Eine Konsequenz von topologischer Supraleitung in eindimensionalen Systemen sind Majoranazustände lokalisiert an den Systemenden. Experimente können deren Lokalisierungslänge mittels Rastertunnelspektroskopie oder über die systemlängenabhängige Hybridisierung von Majoranazuständen an gegenüberliegenden Enden auswerten. Einige dieser Experimente haben eine überraschend kleine Lokalisierungslänge gemessen, in einigen Fällen von atomarer Größenordnung. Diese kleine Lokalisierungslänge ist heute als Resultat der starken Kopplung zwischen den Materialien und dem Überlapp der Majoranamoden in den Supraleiter verstanden. In dieser Arbeit erweitern wir dieses Verständnis mittels einer semiklassischen Streumethodik, welche unter anderem neue Einsichten in den Ursprung der Renormierungseffekte in solchen Systemen ermöglicht.

Fortschritte in experimentellen Techniken erlauben das Wachstum epitaktischer Supraleiter auf Halbleiterdrähten und haben zur Erstellung von Hybridstrukturen mit Schnittstellen hoher Qualität geführt. Allerdings ist die Dicke dieser epitaktischen Supraleiter oft nur ein Bruchteil der Kohärenzlänge im Supraleiter. Es stellt sich daher die Frage, ob diese endliche Ausdehnung nachteilige Effekte auf die starke Kopplung zum Supraleiter hat, und ob diese Effekte umgekehrt werden können, insbesondere in ungeordneten Systemen. Diese Arbeit behandelt diese Fragen mittels analytischer und numerischer Streumethoden.

Eine magnetische Störstelle gekoppelt an einen Supraleiter kann gebundene Yu-Shiba-Rusinov (YSR) Zustände induzieren. Experimentelle Fortschritte erlauben eine detaillierte Abbildung dieser Zustände, so dass YSR Zustände heute in vielen Experimenten beobachtet werden. Eine potenzielle Anwendung ist es, diese Zustände als Bausteine für höherdimensionale Systeme zu verwenden. Beispielsweise um topologische Supraleiter in linearen Ketten zu realisieren. Für solche Anwendungen ist es relevant zu wissen, wie nichtmagnetische Unordnung YSR Zustände beeinflusst. In der vorliegenden Arbeit untersuchen wir diesen Zusammenhang mittels eines streutheoretischen Ansatzes, und zeigen dass die spektralen Eigenschaften von YSR Zuständen in zwei- und dreidimensionalen Systemen eine starke Robustheit gegen moderate Mengen von Unordnung haben.



# Abstract

Over the past two decades, theoretical advances have led to a better understanding of hybrid structures made of magnetic and superconducting materials, and have uncovered promising applications, such as the storage of quantum information and the use for quantum computation. Many experimental studies try to implement and verify these findings. One promising example is that of magnetized wires coupled to an  $s$ -wave superconductor, which is predicted to realize a topological superconductor. Although promising signatures of this phase have been observed, these signatures remain ambiguous and at times accessible only in a small parameter range. Naively, one expects the topological phase to become more stable in the limit of strong coupling between the materials. However, strong coupling can lead to a non-trivial interplay between superconducting and magnetic effects, and a better understanding of the systems at hand is required.

A consequence of topological superconductivity in one-dimensional systems is the appearance of Majorana bound states at the system boundaries. Experiments can access the localization length of these bound states through the use of scanning tunneling microscopy or via the hybridization of Majoranas at opposite ends as a function of wire length. Some of the experiments revealed a surprisingly small localization length, in several cases equalling atomic length scales. This small localization length is now understood to be a result of the strong coupling between the materials and the leakage of the Majorana modes into the superconductor. In this thesis, we extend this understanding by employing a semiclassical scattering approach that gives novel insights on the origin of renormalization effects in strongly-coupled superconductor-magnet hybrids.

Advances in fabrication techniques allow for epitaxial growth of superconducting materials, generating devices that have pristine interfaces between the magnetized normal conductor and the superconducting material. However, often the epitaxial superconductors have a small thickness of only a fraction of their coherence length. This raises the question, whether finite size-effects have detrimental effects on the strong coupling to the superconductor, and whether these effects can be reversed. This thesis tries to answer these questions by employing a combination of analytical and numerical scattering approaches, and by including the effects of disorder.

A magnetic impurity coupled to a superconductor can induce Yu-Shiba-Rusinov (YSR) states bound to the impurity. Advances in experimental techniques allow for detailed spatial and spectral imaging of these states, and many aspects of YSR states have been studied. A potential application of YSR states is to use them as building blocks for higher-dimensional systems, such as linear chains that may realize a topological superconductor. To this end, it is relevant to know how robust YSR states are to disorder. This motivates us to study the impact of non-magnetic disorder on YSR states, within a semiclassical scattering approach. We show that the spectral properties of YSR states have a strong robustness to moderate amounts of disorder in two- and three dimensional systems.



# Contents

<b>Kurzfassung</b>	<b>v</b>
<b>Abstract</b>	<b>vii</b>
<b>1. Introduction</b>	<b>1</b>
<b>2. Heterostructures of magnetic and superconducting materials</b>	<b>3</b>
2.1. Majorana quasiparticles . . . . .	3
2.1.1. Topological superconductivity . . . . .	4
2.1.2. Weakly-coupled magnet-superconductor hybrids . . . . .	6
2.1.3. Majorana bound states in experiments . . . . .	9
2.2. Yu-Shiba-Rusinov states . . . . .	11
2.2.1. Derivation for a simple model . . . . .	11
2.2.2. YSR states in experiments . . . . .	13
<b>3. Scattering theory</b>	<b>19</b>
3.1. Definition of the $S$ -matrix for linear geometries . . . . .	19
3.2. Application to the Kitaev chain . . . . .	21
3.3. Thin-slice concatenation method . . . . .	24
<b>4. Renormalization effects in spin-polarized metallic wires proximitized by a superconductor: A scattering approach</b>	<b>27</b>
4.1. Semiclassical interpretation of the renormalization . . . . .	28
4.2. Planar geometry . . . . .	29
4.2.1. Velocity renormalization . . . . .	31
4.2.2. Minigap and Majorana localization length . . . . .	35
4.3. Cylindrical geometry . . . . .	40
4.3.1. Cylindrical normal-normal metal interface . . . . .	41
4.3.2. Velocity renormalization . . . . .	44
4.3.3. Minigap and Majorana localization length . . . . .	46
4.4. Conclusions . . . . .	49
<b>5. Proximity induced gap in nanowires with a thin superconducting coating</b>	<b>53</b>
5.1. Induced gap from a semiclassical point of view . . . . .	54
5.2. Model . . . . .	56
5.3. Metal-metal junction . . . . .	57
5.4. Excitation gap in the absence of disorder . . . . .	59
5.5. Semiclassical approach to disordered systems . . . . .	61

5.6. Numerical scattering approach . . . . .	63
5.6.1. Implementation details . . . . .	63
5.6.2. Results on disordered systems . . . . .	64
5.6.3. Saturation of surface disorder scattering . . . . .	65
5.7. Conclusion . . . . .	67
<b>6. Effects of nonmagnetic disorder on the energy of Yu-Shiba-Rusinov states</b>	<b>71</b>
6.1. Model . . . . .	72
6.2. Perturbative approach . . . . .	72
6.3. Scattering approach . . . . .	75
6.3.1. Relation between YSR-state energy and scattering amplitudes . . . . .	75
6.3.2. Qualitative discussion . . . . .	77
6.3.3. Numerical calculation of the scattering matrix . . . . .	78
6.4. Relation to Ref. [Hui 15] . . . . .	84
6.5. Conclusion . . . . .	86
<b>7. Conclusion</b>	<b>89</b>
<b>A. Scattering matrix and born approximation</b>	<b>95</b>
<b>B. Details on the numerics of the thin superconductor setup</b>	<b>97</b>
<b>C. Transfer matrix for the YSR problem</b>	<b>101</b>
C.1. Circular slice . . . . .	101
C.2. Spherical slice . . . . .	102
<b>Bibliography</b>	<b>105</b>
<b>Acknowledgements</b>	<b>117</b>
<b>Curriculum Vitae</b>	<b>119</b>
<b>Publications</b>	<b>121</b>

# 1. Introduction

The interplay of magnetism and superconductivity has a long history. An early experiment in this field was performed in 1933, when Walther Meissner and Robert Ochsenfeld placed superconducting tin inside a magnetic field and found that below the critical temperature of tin, the magnetic field was completely expelled from the superconducting region [Meis 33], an effect now known as the Meissner effect. Only two years later, the London equations were proposed, which explain the expelled magnetic field on phenomenological grounds. But it took more than 20 years until Bardeen, Cooper, and Schrieffer proposed their BCS theory of superconductivity and explained the Meissner effect at a microscopic level. Since then, significant advances in both theoretical understanding and experimental techniques have led to a much improved understanding of the interplay of magnetism and superconductivity, although many challenges remain.

In this thesis, we investigate superconductor-magnet hybrids with a focus on strong coupling between the materials, subject to the following specifications. On the one side, we will restrict ourselves to the discussion of superconductors that are in the weak-coupling limit and assume a constant pairing potential inside the superconductor. This allows us to treat the systems of interest on a single-particle level. On the other side, magnetism can have many origins, and in our case we consider any material a magnet that has a significant Zeeman-like splitting term for its electrons in the conducting bands. This splitting may arise due to an internally generated magnetic field, as is present for example in transition metals and half metals, or due to an externally applied field that is sufficiently strong to induce a noticeable spin polarization. The use of such superconductor-magnet heterostructures is a powerful tool, as it allows one to generate effects that may not be present in a homogeneous material. Naively, the effects are expected to be most prominent when the coupling between the two material types becomes strongest.

The structure of this thesis is as follows. In chapter 2, we place this thesis into a broader context and introduce relevant concepts. This includes the theoretical discussion of Majorana quasiparticles and topological superconductivity, as well as a review of experimental progress to detect Majorana quasiparticles. Furthermore, we review the field of magnetic adatoms coupled to a superconductor. In particular, basic theoretical models and recent developments are discussed. In chapter 3, we introduce scattering theory on which much of our later calculations are based, apply it to wires with  $s$ - and  $p$ -wave pairing potentials, and review a concatenation scheme that allows us to calculate the  $S$ -matrix of a scattering region. The main part of the thesis consists of chapters 4 to 6. In chapter 4, we apply a semi-classical scattering approach to a spin-polarized normal metal strongly coupled to an  $s$ -wave superconductor. Due to the strong coupling, one expects renormalization effects reflecting that the wavefunctions living in the normal metal strongly extend into the superconductor. In chapter 5, we consider a related setup, where a normal metal is coupled to a superconductor with a finite thickness. We investigate the effects of the finite

thickness with a focus on the limit of strong coupling between the two materials. Chapter 6 considers the case of a single magnetic adatom in contact with a superconductor, which induces a bound state that lives deep inside the superconductor's gap for a sufficiently strong coupling to the adatom. We investigate the effects of nonmagnetic disorder inside the superconductor on this bound state. Finally, we conclude in Sec. 7.

## 2. Heterostructures of magnetic and superconducting materials

### 2.1. Majorana quasiparticles

During the past decade, much attention has been drawn to the field of topological superconductivity and the appearance of Majorana quasiparticles in condensed matter systems. The idea of Majorana particles dates back to 1937, when Ettore Majorana found that the Dirac equation, which describes elementary fermionic excitations, has a special type of solution that is invariant under charge conjugation. Hence, in contrast to electrons and positrons which are each other's antiparticles, these new types of particles are their own antiparticles [Majo 37]. Particles possessing this property are now referred to as Majorana particles [Elli 15]. Formally, Majorana particles are defined as operators  $\hat{\gamma}_i$ , that follow the relations

$$\hat{\gamma}_i = \hat{\gamma}_i^\dagger, \{\hat{\gamma}_i, \hat{\gamma}_j\} = 2\delta_{i,j}, \quad (2.1)$$

where the braces denote the anticommutator and  $\delta_{i,j}$  is the Kronecker delta.

In high energy physics, the search for elementary particles that are of Majorana type is an ongoing quest and among the known particles in the standard model, neutrinos are a prime candidate as they are charge neutral. However, so far no sufficient experimental evidence has been produced to verify this hypothesis [Elli 15].

On the other hand, a variety of strategies for realizing Majorana quasiparticles in condensed matter systems have been investigated so far [Elli 15]. While in this case, the basic components consist of fermions that are not of Majorana type, such as electrons, one can still define emergent quasiparticles that are their own antiparticles. For example, the excitations of superconductors are superpositions of electrons and holes. If both particle types are of the same spin species, superpositions exist that are of Majorana type. As we will see later, these emergent Majorana quasiparticles can appear over a wide parameter range in systems with certain symmetries.

A large number of theoretical proposals for systems hosting Majorana quasiparticles exist. In the early 2000s, Read and Green proposed that fractional quantum Hall states at filling factor  $\nu = 5/2$  [Read 00] can host Majorana quasiparticles, and elucidated the relation to the BCS theory of superconductivity. Furthermore, it was shown that braiding of these Majorana quasiparticles follows nonabelian statistics [Ivan 01]. As an important technological application, these nonabelian statistics allow one to perform basic quantum gate operations by braiding Majoranas, although additional gates are required to achieve universal quantum computation [Kita 03, Naya 08]. Another influential contribution to the field was made by Kitaev, who provided a minimal model of a one-dimensional p-wave superconductor that hosts Majorana quasiparticles at its end and is now known as the Kitaev chain [Kita 01]. The Kitaev chain is an instructive model to understand the

basic physics of Majorana quasiparticles in one-dimensional systems, and we will treat a continuum version in Section 3.2. Many more proposals followed including materials with intrinsic  $p + ip$  superconductivity [Berg 03, Mack 03], 3D topological insulator surfaces in proximity to an  $s$ -wave superconductor [Fu 08], superfluid  $^3\text{He-B}$  [Volo 03, Sila 10], 2d topological insulator edge states proximitized by alternating ferromagnetic and superconducting sections [Nils 08] and two dimensional semiconductor systems placed in between an  $s$ -wave superconductor and magnetic thin film [Sau 10].

A breakthrough came in 2010, when two groups proposed a setup based on semiconductor nanowires in proximity to a superconductor that was less challenging to implement experimentally [Lutc 10, Oreg 10]. This proposal led to an ongoing series of experiments that produced promising signatures of Majorana quasiparticles in condensed matter systems and which we will discuss in section 2.1.2. Before that, we introduce the mathematical framework of topology that hopefully gives the reader a better understanding of why and when to expect the appearance of Majorana quasiparticles.

### 2.1.1. Topological superconductivity

The proposals for realizing Majorana bound states can be viewed from another perspective, that of topology. The field of topology studies properties of objects that are invariant under certain continuous transformations, such as deformations. A common illustration is that of a doughnut which can be continuously transformed into a coffee cup, so that both are in the same topological class, that of objects with one hole. On the other hand, a doughnut cannot be continuously transformed into a pretzel, which has three holes. In analogy, topology can become relevant in quantum mechanical systems when families of systems can be separated into multiple topological classes that are robust to continuous deformations such as the addition of disorder.

A prominent example is the quantum Hall effect, in which two dimensional electron systems under strong magnetic fields show a conductance that is exactly quantized to multiples of  $e^2/h$  [Klit 80]. It was realized soon after its discovery that the exact quantization has a topological origin, and that the Hall conductivity is a Chern number [Thou 82, Kohm 85]. About two decades later, in 2005, the quantum spin Hall effect that occurs in systems with time reversal symmetry was shown to be classified by a  $\mathbb{Z}_2$  topological index [Kane 05]. Soon afterwards, three dimensional insulators that are invariant under time reversal symmetry were predicted to enter a topological phase leading to the formation of boundary modes, and the term topological insulator was introduced to describe these systems [Fu 07, Moor 07]. Considering only particle-hole symmetry, time reversal symmetry and their combination, it was found that for a fixed dimension and a noninteracting, gapped system ten different symmetry classes arise. Each class is associated with a topological index that is invariant under continuous transformations which keep the gap open and preserve the symmetries. Furthermore, by incrementing the dimension a periodic pattern arises which is summarized in the periodic table of topological insulators and superconductors [Kita 09, Ryu 10]

In the context of this thesis, we are interested in superconducting and magnetic materials, that is systems that possess particle-hole symmetry but break time reversal symmetry. In one dimension, this family of systems is in symmetry class D and has a  $\mathbb{Z}_2$  topological

invariant, splitting the materials into a trivial and a topological phase. Superconductors in the topological phase are referred to as topological superconductors [Sato 17].

As an example, consider the subset of spinless  $p$ -wave superconductors in one dimension. These can be described by the second-quantized Hamiltonian [Sato 17]

$$\hat{\mathcal{H}}_{p\text{-wave}} = \frac{1}{2} \sum_k \begin{pmatrix} \hat{c}_k^\dagger & \hat{c}_{-k} \end{pmatrix} H_{p\text{-wave}}(k) \begin{pmatrix} \hat{c}_k \\ \hat{c}_{-k}^\dagger \end{pmatrix}, \quad (2.2)$$

with the Hermitian Bogoliubov-de-Gennes (BdG) Hamiltonian

$$H_{p\text{-wave}}(k) = \xi_k \tau_z + \hbar k \Delta' \tau_y. \quad (2.3)$$

Here,  $\tau_\alpha$  with  $\alpha = 1, 2, 3$  are the Pauli matrices in particle-hole space,  $\hbar k$  is the quasimomentum,  $\xi_k$  is the dispersion in the absence of superconductivity, which we take symmetric in  $k$  for the sake of simplicity, and  $\hat{c}_k^\dagger$  and  $\hat{c}_k$  are fermionic creation and annihilation operators, respectively, that follow the usual anticommutation relations.

Equation (2.3) describes a spinless superconductor with  $p$ -wave pairing potential  $\hbar k \Delta'$ , where  $\Delta'$  is real and we consider finite  $\Delta'$  only.

The spectrum has the form

$$\varepsilon = \pm \sqrt{\xi_k^2 + (\hbar k \Delta')^2}. \quad (2.4)$$

Hence, the energy gap can only close at the  $\Gamma$ -point, that is at  $k = 0$ .

This allows us to define the topological invariant  $\nu \in \{0, 1\}$  by the relation [Sato 17]

$$(-1)^\nu = \text{sgn}(\xi_\Gamma), \quad (2.5)$$

where  $\text{sgn}$  denotes the signum function and  $\xi_\Gamma = \xi_{k=0}$ . Any Hamiltonian described by Eq. (2.3) that has a negative  $\xi_\Gamma$  ( $\nu = 1$ ) cannot be continuously transformed into a Hamiltonian with a positive  $\xi_\Gamma$  ( $\nu = 0$ ) while keeping the gap open. Hence, there exist two separate phases.

Topology does not define which of these phases is trivial. For realistic systems, the trivial phase is usually defined as the one which can be smoothly transformed to the atomic limit or vacuum. In the case of (2.3), this corresponds to a fully depleted normal state Hamiltonian with  $\xi_k \gg 0$  for all  $k$ . On the other hand in the topological phase, the Fermi surface encloses the  $\Gamma$ -point, and  $\nu = 1$ . Employing a similar argument, multichannel odd-parity superconductors can be shown to be in the topological phase when they enclose an odd number of time reversal invariant points [Sato 17].

To infer the existence of bound states, we can employ the powerful concept of bulk-boundary correspondence. If a system in a topological phase is spatially connected to a trivial one, for example by cutting the wire and connecting it to vacuum, the topological index has to change from trivial to topological at the boundary. This is only possible if the gap closes, and a gapless boundary modes has to appear. The concept of bulk-boundary correspondence can be applied to any symmetry class in the periodic table for topological insulators and superconductors [Ando 13]. For superconductors, particle-hole symmetry states that for every excitation  $\gamma_\varepsilon^\dagger$  at energy  $\varepsilon$ , there exists a particle-hole conjugated

excitation  $\gamma_{-\varepsilon}$ . Hence, for a single boundary state, this state has to be invariant under particle-hole conjugation and has to live at zero energy. Consequently it is of Majorana type [Pien 14a].

In this thesis, we are especially interested in the case when only particle-hole symmetry is present (referred to as class D). The Hamiltonian in Eq. (2.3) is invariant under particle-hole symmetry of the form

$$\tau_x H_{p\text{-wave}}^*(k) \tau_x = -H_{p\text{-wave}}(-k), \quad (2.6)$$

where the asterisk denotes complex conjugation. It also obeys a time-reversal symmetry

$$H_{p\text{-wave}}^*(k) = H_{p\text{-wave}}(-k), \quad (2.7)$$

and actually belongs to another symmetry class (referred to as BDI). However when generalizing the model to multi-channel wires, this time-reversal symmetry can be broken, for example by adding the term  $\hbar k_{\perp} \Delta' \tau_x$  to the Hamiltonian (2.3), where  $k_{\perp}$  is the momentum in the transverse direction. When the transverse direction is sufficiently narrow so that only a few channels are occupied, we can consider the system quasi-one dimensional [Pien 14a].

The emerging Majorana quasiparticles are robust because deformations of the Hamiltonian that preserve particle-hole symmetry and do not close the gap cannot change the topological invariant [Kita 09]. In realistic systems, a sizable gap in the bulk is needed to provide good topological protection. Furthermore, bulk-boundary correspondence requires the presence of a bulk, that is the system has to be large enough to provide a clear distinction between boundary and bulk. Finally, even if a large gap is present and the wire is long, the detection of the boundary modes can remain challenging because bulk-boundary correspondence does not prohibit additional surface states at or close to zero energy.

In conclusion, topology is a powerful tool to predict which symmetries a system has to possess in order to be in a topological phase. However, more detailed studies are required to understand for which parameter configurations a topological phase appears, how stable these are in the presence of perturbations such as disorder, and how the emergent boundary modes can be detected and possibly distinguished from nontopological boundary modes.

### 2.1.2. Weakly-coupled magnet-superconductor hybrids

In this section, we discuss a basic model that describes one-dimensional magnetic wires weakly coupled to an  $s$ -wave superconductor. In 2010, two groups proposed that these systems host Majorana bound states, and that they can be realized using semiconductor nanowires [Lutc 10, Oreg 10]. Since then, promising signatures of Majorana bound states have been observed in these systems, as we will see in Sec. 2.1.3.

The two proposals [Lutc 10, Oreg 10] consider a BdG-Hamiltonian of the type

$$\hat{H}_{\text{1d-wire}} = \left( \frac{\hat{p}^2}{2m} - \mu + B\sigma_z \right) \tau_z + \alpha_{\text{so}} \hat{p} \sigma_x + \Delta \sigma_y \tau_y \quad (2.8)$$

in one dimension, where  $\tau_{\alpha}$  and  $\sigma_{\alpha}$  are the Pauli matrices in particle-hole and spin-space, respectively, and  $\alpha = x, y, z$ . The BdG spinor reads  $(u_{\uparrow}, u_{\downarrow}, v_{\uparrow}, v_{\downarrow})^T$ , where  $u$  and  $v$  describe

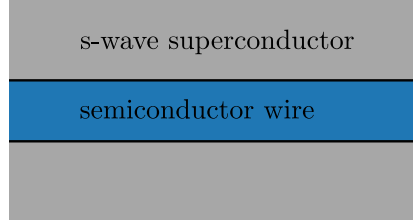
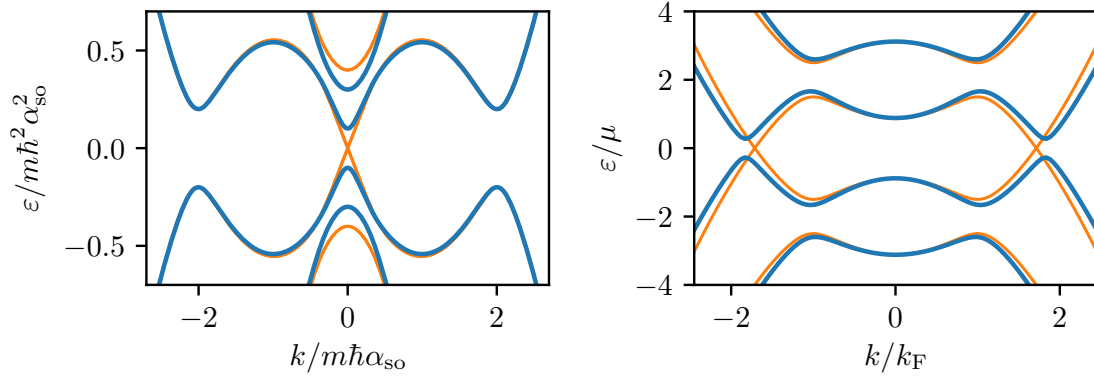


Figure 2.1.: Top view of a nanowire placed on top of a three dimensional superconductor.


 Figure 2.2.: Dispersion of a proximitized nanowire for strong spin-orbit coupling (left) and a large magnetic field (right). On the left, the lines show Eq. (2.9) for  $m\hbar^2\alpha_{\text{so}}^2/\Delta = 5$ ,  $B/\Delta = 0.5$  (blue) and  $B/\Delta = 1$  (orange), and  $\mu = 0$ . On the right, the lines show  $B/\mu = 2$ ,  $\Delta/\mu = 0.5$  and  $m\hbar^2\alpha_{\text{so}}^2/\mu = 0.25$  (blue) and  $\alpha_{\text{so}} = 0$  (orange).

particles and hole wavefunctions, respectively, and the arrows index the spin components. Equation (2.8) describes the electronic excitations of a nanowire with momentum  $\hat{p} = -i\hbar\partial_x$ , mass  $m$ , chemical potential  $\mu = \hbar^2k_F^2/2m$ , Fermi wavevector  $k_F$ , intrinsic spin-orbit coupling  $\alpha_{\text{so}}$  and Zeeman splitting  $2B$ .

The wire is assumed to be placed in proximity to an *s*-wave superconductor, as shown in Fig. 2.1. If the coupling to the superconductor is weak, the system is well described by Eq. (2.8) with constant pairing potential  $\Delta$  and the superconductor integrated out. In chapters 4 and 5 we will extend this model and consider several aspects that change in the case of strong coupling between wire and superconductor.

The Hamiltonian 2.8 has been solved in detail in Refs. [Lutc 10] and [Oreg 10]. Based on these two references, we now give a basic derivation of the results that are relevant for our later discussion.

The eigenenergies of Eq. (2.8) read

$$\varepsilon(k) = \pm \sqrt{B^2 + (\alpha_{\text{so}}\hbar k)^2 + \Delta^2 + \xi_k^2 \pm 2\sqrt{B^2\Delta^2 + (B\xi_k)^2 + (\hbar k\alpha_{\text{so}}\xi_k)^2}}, \quad (2.9)$$

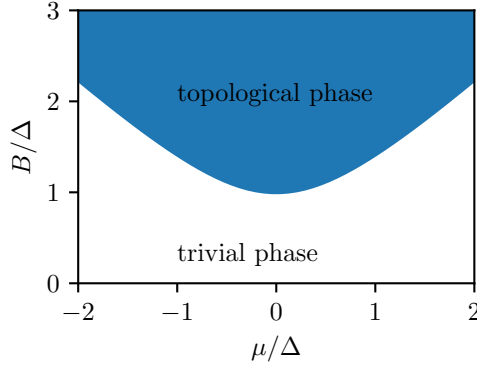


Figure 2.3.: Phase diagram for a nanowire weakly coupled to an  $s$ -wave superconductor.

for a wavenumber  $k$  and  $\xi_k = (\hbar k)^2/2m - \mu$ . Examples of the spectrum are shown in Figure 2.2. For the case of strong spin-orbit coupling (left plot, blue line), the dispersion corresponds to two horizontally shifted parabolas, mirrored at the  $\varepsilon = 0$  line, and split at their crossing points. For the case of a strong magnetic field (right plot, blue line), the dispersion corresponds to two vertically shifted parabolas, also mirrored at  $\varepsilon = 0$ , and split at their crossings.

In order to detect potential topological phases, we first calculate where the gap closes. After setting  $\varepsilon(k) = 0$  and applying some algebra, we obtain the condition

$$\xi_k^2 = B^2 + (\hbar k \alpha_{\text{so}})^2 - \Delta^2 - 2i\hbar k \alpha_{\text{so}} \Delta. \quad (2.10)$$

Up to the last term, all terms are real; the gap closes at  $k = 0$  only and one requires  $B^2 = \mu^2 + \Delta^2$ . (Here we assume that  $\alpha_{\text{so}}$  and  $\Delta$  are always finite). This defines the boundary between two phases, as shown in Fig. 2.3. The upper phase is disconnected from the vacuum ( $\mu \rightarrow -\infty$ ) and hence referred to as the topological phase.

For the case  $\mu = 0$  and large spin-orbit coupling, the closing of the gap is shown in Fig. 2.2 (left plot, orange lines). In this case, the low-energy physics is described by a massive, spinless Dirac equation [Pien 14a]. One can tune across the phase transition by tuning the magnetic field.

For a large magnetic field compared to the chemical potential and no spin-orbit coupling, the wire is spin polarized. Since the pairing potential pairs opposite spins, the dispersion becomes gapless, as can be seen from the right plot in Fig. 2.2 (orange lines). Turning on spin-orbit coupling slightly rotates the spins at opposite momenta in opposite directions and thus allows for pairing within the spin-polarized wire. Because this pairing is within the same spin-species, it is referred to as triplet pairing and is of  $p$ -wave type. Consequently, the low-energy physics becomes equivalent to that of the Hamiltonian (2.3).

Bulk-boundary correspondence ensures that when terminating the wire in the topological phase, Majorana bound states appear at the boundary at zero energy. In section 3.2, we give an explicit derivation of the boundary states in the limit of large  $B$ .

### 2.1.3. Majorana bound states in experiments

In this section, we discuss experimental progress towards observing Majorana quasiparticles in heterostructures consisted of superconducting materials and magnetic or strongly spin-orbit coupled normal metal wires. These experimental developments motivate the work presented in the later chapters of this thesis.

In order to confirm that bound states of Majorana type are indeed present in experiments one would ideally verify that they follow the exchange statistic of Majorana particles in Eq. (2.1). However, this is experimentally challenging and instead one relies on signatures that are available without braiding Majorana bound states. Two signatures that received much attention are zero-bias peaks in the conductance spectrum [Seng 01, Law 09, Akhm 11] and the  $4\pi$  Josephson effect [Kita 01, Fu 09]. In the following, we focus on the former.

Briefly after the first theoretical proposals on semiconductor nanowires [Lutc 10, Oreg 10], several groups reported experimental signatures of Majorana bound states [Mour 12, Will 12, Rokh 12, Deng 12, Das 12]. Several of these reports included the observation of zero-bias peaks in the conductance spectra. Ideally the zero energy conductance should be quantized to  $2\frac{e^2}{h}$ , however in many experiments the conductance peak has been far below the quantized value [Mour 12, Deng 12, Das 12, Chur 13, Albr 16, Deng 16, Gul 18].

On the one hand it was pointed out that these lower peaks can generically appear even if the system is in a topologically trivial phase, for example due to scattering from disorder in multichannel wires [Liu 12]. On the other hand, several effects have been proposed that could lead to a reduced peak height even if a Majorana bound state would be present. First, thermal broadening would naturally lead to a flattened peak, if temperature exceeds the zero-temperature width of the zero-bias peak [Pien 12, Lin 12] and early experiments indeed showed that the observed zero-bias peaks have a strong dependency on temperature [Mour 12]. Theoretical studies show that the intrinsic width of the zero-bias peak can be enhanced by increasing the tunnel coupling between lead and wire, as well as increasing the proximity induced gap [Pien 12]. Another effect that is believed to flatten the zero-bias peak is a series of dissipation effects, among which is the dissipation into other subgap states through interactions [Liu 17]. The appearance of such subgap states is often referred to as a soft gap, and experimental effort has been put into hardening the gap [Chan 15, Gul 17]. Possible explanations for the soft gap are Andreev bound states as well as a density of states induced by inhomogeneities at the semiconductor-superconductor interfaces [Take 13].

Majorana bound states have been predicted to exist in another type of system, chains of magnetic adatoms coupled to a superconductor. These systems do not require the application of an external magnetic field and make it easy to combine three relevant ingredients for topological superconductivity: An  $s$ -wave pairing potential, spin polarization intrinsic to the adatoms, and spin-orbit coupling that is intrinsic to the superconductor or is emulated by a helical magnetic ordering of the impurity chain [Nadj 13, Pien 14b]. After the first theoretical proposals of these systems, experiments used scanning tunneling microscopy (STM) tips to probe the local density of states for Fe chains deposited on Pb, revealing zero-energy peaks localized at the ends of the chain in accordance with the predicted Majorana bound states [Nadj 14, Ruby 15a, Feld 17, Kim 18]. Further studies

claimed that the bound states also appear in atomic force microscopy [Pawl 16] and that the zero-bias peaks carry a spin polarization [Feld 17].

An initially surprising characteristic of the observed bound states was their very small localization length of the order of a few adatom sites. Naively, one might expect that given a velocity  $v$  inside the effective one-dimensional system, created by the adatom chain, and an induced gap  $\Delta_{\text{ind}} \leq \Delta$ , where  $\Delta$  is the gap in the host superconductor, the Majorana wave is exponentially localized at a scale of at least  $\hbar v/\Delta$ , the coherence length inside the superconductor. However, this length scale is typically much larger than the distance between the adatom sites. This discrepancy was first resolved by a theoretical study [Peng 15], showing that Majorana bound states are strongly localized at the end of adatom chains due to the wavefunction hybridization with the superconductor.

As noted earlier, it is desirable to have a large induced gap when realizing systems hosting Majorana bound states. Apart from the choice of the superconducting material, a strong coupling between the superconductor and the normal region is beneficial. In chapter 4 we discuss such a system and consider renormalization effects caused by the high transparency.

For the experiments involving adatom chains, the strong coupling regime is believed to be naturally present as the coupling strength is fixed by atomic scales [Peng 15]. In the case of the semiconductor nanowires, one can think of strong coupling as resulting from an interface with a high transparency and a small gap so that modes decay slowly into the superconductor. In particular, a transparency of order unity can be achieved if the velocities of quasiparticles propagating on both sides are comparable, and the interface is homogeneous and involves no potential barrier. Hence, apart from a high interface quality, two materials with approximately matching Fermi velocities should be chosen. One such combination that is used in experiments is that of Al as a superconductor and the semiconductor InSb [Gul 17, Gul 18]. InSb has an effective mass  $m_{\text{InSb}} = 0.014m_e$  where  $m_e$  is the mass of the electron [Vurg 11]. A quick parameter estimate shows that these materials are in the regime of approximately matching Fermi velocities: The Fermi velocity of most metals, including Al, is of order  $10^6$  m/s [Ashc 76]. Assuming a quadratic dispersion for InSb,  $\varepsilon = \mathbf{p}^2/2m_{\text{InSb}}$  with momentum  $\mathbf{p}$ , a Fermi velocity matching the one in Al can be achieved by applying a gate voltage such that the Fermi level inside InSb lies at  $\sim 50$  meV relative to the band bottom. Such a value seems feasible, as it is small compared to the band gap in InSb  $\sim 235$  meV [Vurg 11] and a Fermi level sufficiently high to reach a finite conductance has been achieved in experiments, see for example [Wepe 13]. Another popular choice of semiconductor material is InAs, which has properties similar to InSb [Krog 15, Deng 16, Kjae 17].

Advances in experimental growth techniques allow for the fabrication of high-quality samples and improved control. In particular, it has become possible to create semiconductor nanowires surrounded by a superconducting shell using epitaxial growth, and the resulting samples exhibit fewer inhomogeneities inside the nanowire as well as at the superconductor nanowire interface [Krog 15, Chan 15, Deng 16, Albr 16, Zhan 18]. Furthermore, the in-gap conductance at zero magnetic field is orders of magnitude smaller than the out of gap conductance, hinting at hard gaps without any sub-gap states [Chan 15].

However, there have been some concerns on whether finite-size effects could be detrimental to the induced energy gap and the extent of the topological phase in parameter

space [Reeg 17]. In particular, the widths of the superconducting Al shells used are below 50 nm, a size which is much smaller than the superconducting coherence length that is of order  $\mu\text{m}$  in Al. In chapter 5, we consider this setting and show that disorder, either in the bulk or at the surface of the superconductor, is a relevant ingredient that diminishes the detrimental finite-size effects.

Very recent experiments on semiconductor nanowires with superconducting shells show conductance peak heights of  $2e^2/h$ , robust to changes in gate voltages and magnetic field [Nich 17, Zhan 18]. This provides further evidence that the produced samples may host Majorana bound states.

## 2.2. Yu-Shiba-Rusinov states

Chapter 6 investigates a system consisting of a single magnetic impurity placed on top of or inside a superconductor. These systems have drawn much attention over the past decades, starting with theoretical investigations by Yu, Shiba, and Rusinov (YSR) [Yu 65, Rusi 68, Shib 68] in the late 1960s, about a decade after the development of the BCS theory of superconductivity [Bard 57]. YSR found that the presence of a single magnetic impurity in contact with a superconductor induces states that lie within the gap of the superconductor and that are spatially bound to the impurity. Nowadays, these states are referred to as YSR- or Shiba states and are of great interest for fundamental research. Furthermore, chains of magnetic adatoms may realize a topological superconductor as discussed in Sec. 2.1.3.

### 2.2.1. Derivation for a simple model

In this section, we give a brief derivation of the YSR energies that is strongly related to Shiba's original derivation [Shib 68] and follows the lines of Ref. [Pien 13]. Rusinov gave an alternate derivation in terms of scattering phase shifts [Rusi 68], which we will discuss in chapter 6. Those readers already familiar with Shiba's derivation may directly jump to Eq. (2.18).

An impurity embedded in the bulk of a three dimensional superconductor can be modeled by the BdG Hamiltonian

$$\hat{H}_{\text{YSR}} = \xi_{\mathbf{k}}\tau_z + \Delta\tau_x + J\mathbf{S}\boldsymbol{\sigma}\delta_{\lambda}(\mathbf{r}), \quad (2.11)$$

with the BdG spinor  $(u_{\uparrow}, u_{\downarrow}, v_{\downarrow}, -v_{\uparrow})$ , made up of electron ( $u$ ) and hole ( $v$ ) wavefunctions with  $\uparrow$  and  $\downarrow$  indexing the electron spin, and  $\tau_j$  are the Pauli matrices in particle-hole space with  $j = x, y, z$ . The first two terms describe a superconductor with a dispersion  $\xi_{\mathbf{k}} = \hbar^2(\mathbf{k}^2 - k_{\text{F}}^2)/2m$ , mass  $m$ , wavenumber  $k_{\text{F}}$  at the Fermi level, and uniform  $s$ -wave pairing potential  $\Delta$ . The last term describes the exchange coupling  $J > 0$  between the electronic states of the superconductor and a classical impurity with spin  $\mathbf{S}$ . The electronic spin is described by the vector of Pauli matrices  $\boldsymbol{\sigma} = (\sigma_x, \sigma_y, \sigma_z)^T$ . The spatial extent of the exchange coupling is described by a short-range function  $\delta_{\lambda}(\mathbf{r})$  with unit integral and range  $\lambda \lesssim 1/k_{\text{F}}$ .

We now solve the eigenvalue problem

$$\hat{H}_{\text{YSR}}\psi(\mathbf{r}) = \varepsilon\psi(\mathbf{r}) \quad (2.12)$$

for energies  $|\varepsilon| < \Delta$ . We choose the  $z$ -axis to be parallel to  $\mathbf{S}$ , such that the Hamiltonian (2.11) becomes block diagonal and restrict ourselves to the block  $\psi(\mathbf{r}) = (u_\uparrow, 0, v_\downarrow, 0)^T$ . After rearranging the terms involved in Eq. (2.12) we obtain

$$(\varepsilon - \xi_{\mathbf{k}}\tau_z - \Delta\tau_x)\psi(\mathbf{r}) = \sigma JS\delta_\lambda(\mathbf{r})\psi(\mathbf{r}), \quad (2.13)$$

where  $\sigma = +1$ . The solutions of the block  $(0, u_\downarrow, 0, -v_\uparrow)$  follow from particle-hole-symmetry  $i\tau_y\mathcal{K}\hat{H}_{\text{YSR}}(i\tau_y\mathcal{K})^\dagger = -\hat{H}_{\text{YSR}}$ , which keeps Eq. (2.13) invariant up to the change  $\sigma \rightarrow -1$ . In the following, we consider the block with  $\sigma = 1$ .

We map the problem to  $\mathbf{k}$ -space via the Fourier transform

$$\psi(\mathbf{r}) = \int \frac{d\mathbf{k}}{(2\pi)^3} e^{i\mathbf{k}\mathbf{r}} \psi_{\mathbf{k}}, \quad (2.14)$$

which transforms Eq. (2.13) to

$$\psi_{\mathbf{k}} = \frac{JS}{\varepsilon - \xi_{\mathbf{k}}\tau_z - \Delta\tau_x} \int d\mathbf{r} e^{-i\mathbf{k}\mathbf{r}} \delta_\lambda(\mathbf{r})\psi(\mathbf{r}). \quad (2.15)$$

By integrating both sides of Eq. (2.15) with  $\int d\mathbf{k}/(2\pi)^3$ , we obtain

$$\psi(\mathbf{r}) = \int \frac{d\mathbf{k}}{(2\pi)^3} \frac{JS e^{i\mathbf{k}\mathbf{r}}}{\varepsilon - \xi_{\mathbf{k}}\tau_z - \Delta\tau_x} \psi(\mathbf{0}). \quad (2.16)$$

Here, we assume that  $\psi(\mathbf{r})$  is approximately constant for  $|\mathbf{r}| \lesssim \lambda$ , we approximate the last integral in Eq. (2.15) by  $\psi(\mathbf{0})$ , and take the  $\mathbf{k}$ -space integral to have a high-energy cutoff  $k_c \sim 1/\lambda$ . For a more formal introduction of a cutoff we refer to Ref. [Pien 13].

The  $\mathbf{k}$ -space integral in Eq. (2.16) for  $\mathbf{r} = 0$  can be solved by applying the replacement  $\int d\mathbf{k}/(2\pi)^3 \rightarrow \nu_0 \int d\xi_{\mathbf{k}}$  and linearising  $\xi_{\mathbf{k}}$ , where we define the density of states per energy, spin and volume  $\nu_0 = mk_F/2\pi^2\hbar^2$ . By performing contour integration, the  $\xi_{\mathbf{k}}$ -integration is solved by evaluation at the poles. In principle, one has to add the Cauchy principal value, however as we will show in chapter 6, the Cauchy principal value leads to a renormalization of  $J$  and does not qualitatively alter our results. Due to this and for the sake of simplicity, in the following, we neglect the Cauchy principal value. At the origin, Equation (2.16) then evaluates to [Pien 13]

$$\psi(\mathbf{0}) = -\pi\nu_0 JS \frac{\varepsilon + \Delta\tau_x}{\sqrt{\Delta^2 - \varepsilon^2}} \psi(\mathbf{0}), \quad (2.17)$$

which has the subgap solutions

$$\varepsilon_{\text{YSR}} = -\Delta \frac{1 - \alpha^2}{1 + \alpha^2}, \quad (2.18)$$

where  $\alpha = \pi\nu_0 JS$ .

As expected, in the absence of the impurity no subgap states are present. Upon increasing  $J$ , a state detaches from  $\varepsilon = -\Delta$  and enters the gap. This type of state is referred to as a YSR or Shiba state. At a critical  $J_c = 1/\pi\nu_0 S$  the state crosses zero energy and beyond  $J_c$  asymptotically reaches  $\varepsilon = \Delta$ .

The sign of the energy (2.18) has important consequences in terms of the many-body ground state, as was discussed by Sakurai [Saku 70]. Recall that a state with negative energy corresponds to a state that is occupied in the ground state, and that in the derivation of the YSR state, we restricted ourselves to the subspace of  $u_\uparrow$  and  $v_\downarrow$ . For  $0 < J < J_c$ , we have  $\varepsilon_{\text{YSR}} < 0$ , the YSR state is occupied. This can be interpreted as a ground state in which the magnetic impurity binds a spin-up electron and a spin-down hole. The total electronic spin is  $S_{\text{elec}} = 0$ , as the ground state is connected to the case of no impurity ( $J = 0$ ) where it is formed by spin-singlet Cooper pairs. In contrast, for  $J_c < J$ , the YSR energy becomes positive and the ground state changes to one where a spin-up electron and spin-down hole are unoccupied. Consequently, the total spin changes to  $S_{\text{elec}} = -1$  and the magnetic impurity binds a localized state constituted of a spin-down electron and a spin-up hole.

We now turn to the YSR wavefunction. At  $\mathbf{r} = 0$ , we have  $\psi(\mathbf{0}) \sim (1, -1)^T$ . At distances  $|\mathbf{r}| \gg \lambda$ , the integral (2.16) yields [Pien 13]

$$\psi(\mathbf{r}) \sim \frac{e^{-r/\xi_\varepsilon}}{k_{\text{F}}r} \begin{pmatrix} \sin(k_{\text{F}}r - \tan^{-1}\alpha) \\ -\sin(k_{\text{F}}r + \tan^{-1}\alpha) \end{pmatrix}, \quad (2.19)$$

where  $\xi_\varepsilon = \hbar^2 k_{\text{F}} / \sqrt{\Delta^2 - \varepsilon^2}$ . The YSR wavefunction is localized near the magnetic impurity, with a power-law decay at short distances from the impurity and an exponential decay beyond  $\xi_\varepsilon$ . Another important feature is the asymmetry of the particle- and hole components of wavefunction due to the phase shift  $\tan^{-1}\alpha$ . As we will see in chapter 6, this phase shift corresponds to the scattering phase that a normal-state electron picks up when it scatters from the magnetic impurity.

In this section, we discussed a simple model of a magnetic adatom embedded in a superconductor. Following YSR's initial proposal, many aspects of YSR states have been theoretically considered in more complex models. Examples include the local variation of the pairing potential in the vicinity of the magnetic impurity [Rusi 69, Morr 06, Meng 15], the interplay of a small number of magnetic impurities [Morr 06, Yao 14, Meng 15, Hoff 15], the relation to the Kondo effect [Zitk 11], and the realization of a topological superconductor in YSR-chains [Nadj 13, Pien 13].

In Chapter 6, we investigate another aspect of YSR states, the impact of weak non-magnetic disorder on their spectral properties. The impact of non-magnetic disorder on time-reversal symmetric superconductors has been studied by Anderson [Ande 59]. He showed that the critical temperature and the spectral gap of an  $s$ -wave superconductor is robust to weak disorder, even if the mean free path becomes small compared to the coherence length in the superconductor. However, in the presence of a magnetic impurity time-reversal symmetry is broken. Still, as we will see in chapter 6, an argument similar to Anderson's can be applied to attribute YSR states a strong robustness against weak disorder.

### 2.2.2. YSR states in experiments

In the early years after YSR's prediction, experimental progress was hindered by the lack of techniques to control and measure the local properties near the adatom site. In 1997, Eigler et al. employed a new set of techniques to study YSR states, such as the preparation of

clean superconductor surfaces and the deposition of adatoms at low temperatures [Yazd 97, Hein 18]. Furthermore, scanning tunneling microscopy became available, which uses a tip to scan across the surface and to probe the local density of states on an atomic scale, with energy resolution below the gap of the superconductor [Binn 83, Yazd 97]. The resulting conductance spectrum is shown in Fig. 2.4, at a temperature of about a quarter the size of the superconducting gap. Although subgap peaks in the conductance difference spectrum (right plots) are visible at the sites of magnetic adatoms, the peaks are washed out and do not show delta-like peaks that one would expect at very small temperatures.

More recent experiments on YSR states use lower temperatures and superconducting tips to improve the energy resolution [Ji 08, Ji 10, Fran 11, Mena 15, Ruby 15b, Hatt 15, Ruby 16, Choi 17, Kezi 18, Hein 18]. While lower temperatures trivially reduces the thermal broadening, the use of superconducting tips is more involved and is studied in detail in Ref. [Ruby 15b]. In the following, we give a brief summary of Ref. [Ruby 15b], which hopefully allows the reader to better understand the resulting scanning tunneling images using superconducting tips.

Consider the quasiparticle spectrum shown in Fig. 2.5 with a YSR state at a finite energy, and for temperatures small compared to the gap. The spectral distance between the Fermi levels (dashed lines) and the band gap edges is of magnitude  $\Delta$  in both materials. Reminiscent of the tunneling between normal state metals, at a sample bias  $eV > 2\Delta$  electrons from the occupied quasiparticle continuum in the tip (left for each plot) can directly tunnel into the unoccupied continuum of the substrate (right), and similarly a current flows for  $eV < -2\Delta$ .

For  $-2\Delta < eV < 2\Delta$ , we first consider processes that do not involve YSR states. On the one hand, thermally excited electrons and holes can tunnel directly between substrate and tip continua. These processes are suppressed for small temperatures compared to the gap. On the other hand for  $0 < eV < 2\Delta$ , electrons in the occupied continuum of the tip can be multiply Andreev reflected, with a voltage threshold that depends on the number of reflections. Andreev reflection processes correspond to processes where an electron from the tip tunnels into the substrate, forms a Cooper pair and a counter propagating hole tunnels back into the tip. These processes require the tunneling of two quasiparticles and are only relevant at strong tunneling. The same arguments apply for Andreev reflection of tip-holes into tip-electrons at negative sample bias.

The presence of a YSR state (solid line) enables the resonant tunneling processes shown in Fig. 2.5: At a bias  $eV = \pm(\Delta + \epsilon_{\text{YSR}})$ , quasiparticles from the tip can (a) hop into the YSR state and subsequently relax into the substrate continuum, (b) quasiparticles can be Andreev reflected via a YSR state, and (c) at a bias  $eV = \pm(\Delta - \epsilon_{\text{YSR}})$ , thermally excited quasiparticles in the substrate can relax into the Shiba state and then tunnel into the tip. The processes (a)-(c) are strongest when the YSR states are resonant with the high spectral density at the band edge of the tip. This is expected to lead to pronounced peaks in the conductance spectrum.

The tunneling processes (a) and (c) involve tunneling of a single electron between tip and substrate, and their relative strength at positive and negative bias reflects the ratio of electron and hole components of the YSR state. Because process (b) involves tunneling of an electron and a hole, the processes (a) and (c) are dominant at a weak normal-state conductance. For larger normal-state conductances, a crossover to a regime dominated by

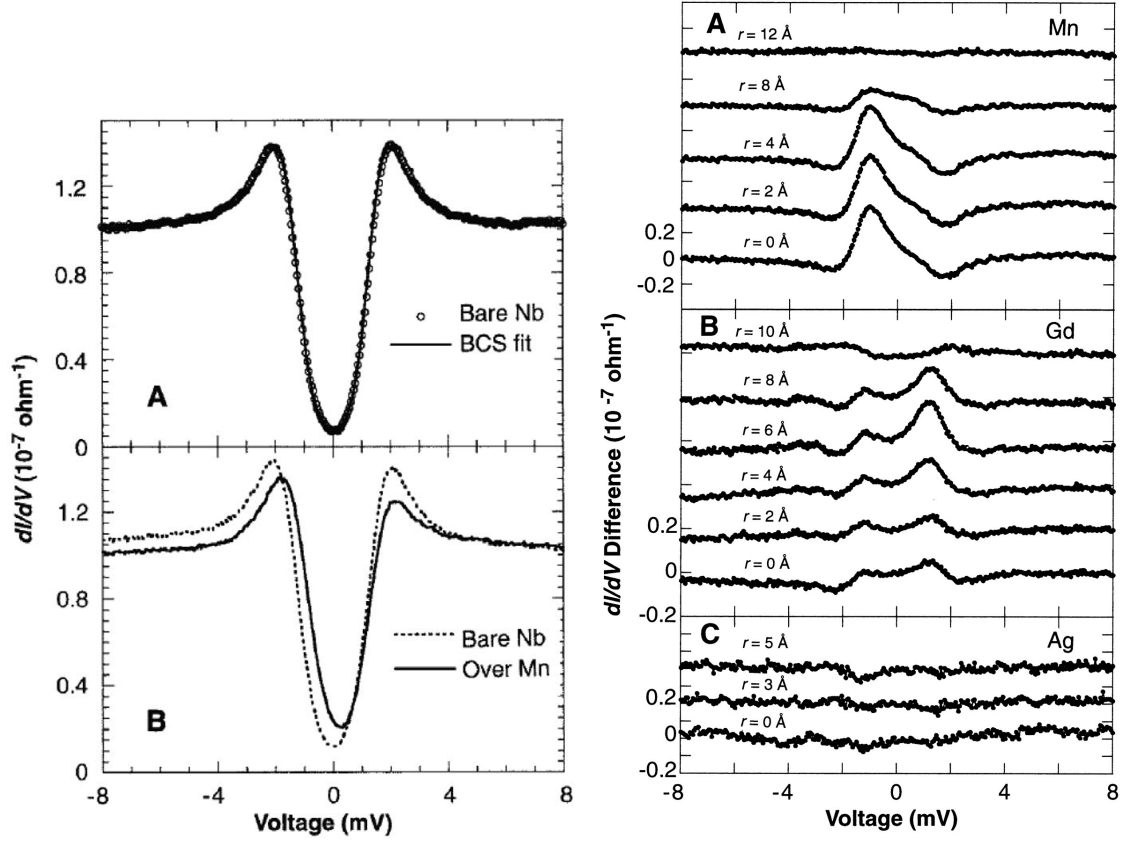


Figure 2.4.: STM conductance spectra of superconducting Nb. From [Yazd 97]. Reprinted with permission from AAAS. On the left, the conductance spectrum over bare Nb and on top of a Mn impurity is shown. A change in the conductance is visible. On the right, the difference of the conductance over an adatom to that over bare Nb is shown. For each plot, the different lines show different distances from the adatom, and each line has a constant offset. The adatoms are Mn, Gd and Ag, the former two are magnetic and show sub-gap peaks, while Ag is nonmagnetic and no significant change in the conductance spectrum is visible.

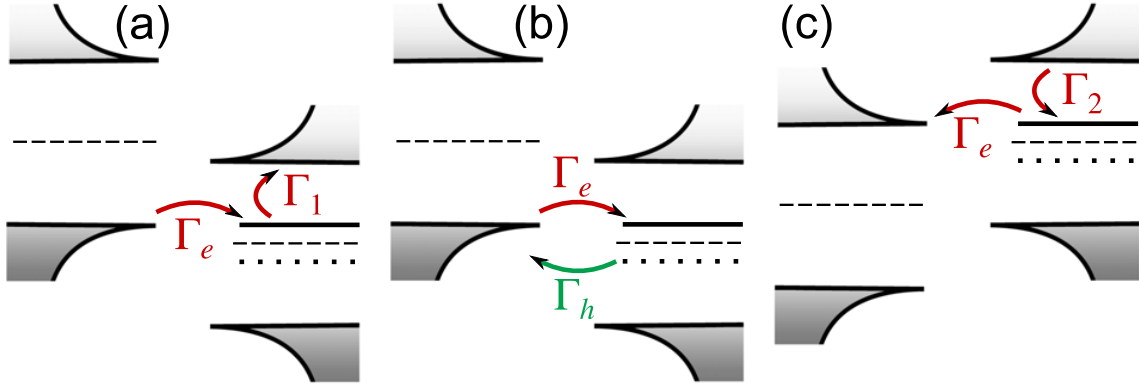


Figure 2.5.: Principal tunneling processes involved in probing a YSR state (solid line, enclosed by BCS quasiparticle peaks) with the quasiparticle peaks of a superconducting tip (left in (a), (b) and (c)). The dashed lines indicate the chemical potential in the tip and the substrate. Reprinted figure with permission from [Ruby 15b] at doi. Copyright 2015 by the American Physical Society. Single particle-tunneling from tip to substrate is shown in (a): An electron from the substrate continuum tunnels into the YSR state at a rate  $\Gamma_e$  and subsequently relaxes into the substrate continuum at a rate  $\Gamma_1$ . In (b), resonant Andreev reflection is shown, which transfers a cooper pair from the tip to the substrate. This involves tunneling of an electron at a rate  $\Gamma_e$  and a hole  $\Gamma_h$ . In (c), a thermally-excited substrate-electron relaxes into the YSR state at a rate  $\Gamma_2$  and subsequently tunnels into the tip at a rate  $\Gamma_e$ .

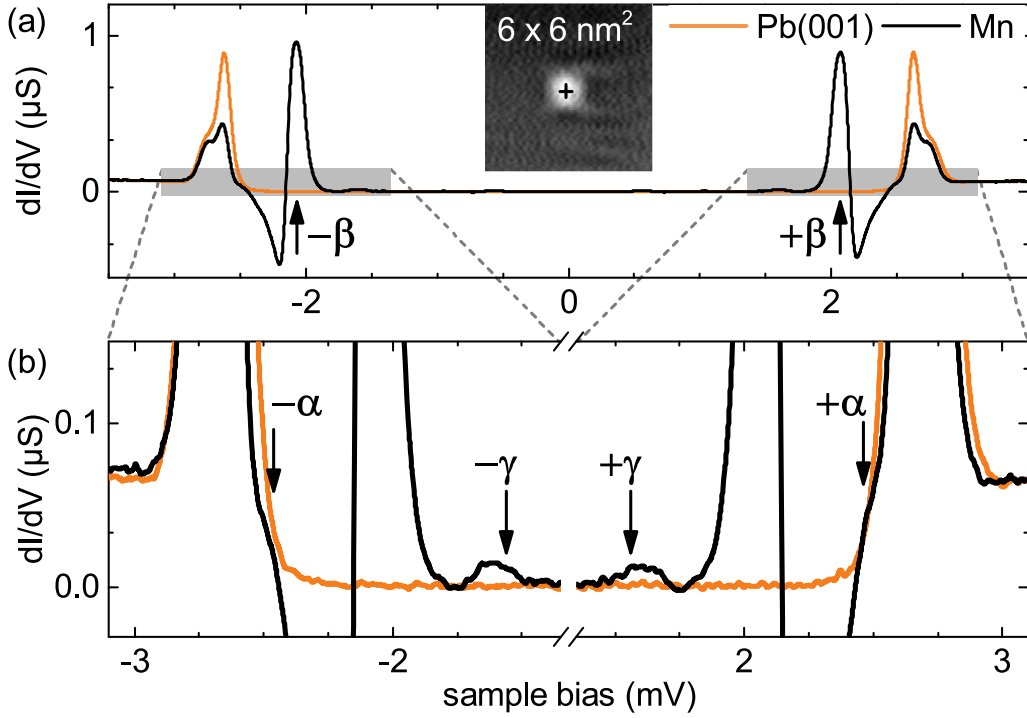


Figure 2.6.: STM conductance spectra of clean Pb (orange) and on top of a Mn adatom (black) using a superconducting tip. Reprinted figure with permission from [Ruby 16] (<https://doi.org/10.1103/PhysRevLett.117.186801>). Copyright 2016 by American Physical Society. Two strong subgap resonances are visible in (a) denoted by  $\pm\beta$ , the zoom in (b) reveals additional peaks  $\pm\gamma$  and shoulders  $\pm\alpha$ . The inset in (a) shows the topography in the vicinity of the Mn adatom.

process (b) is found, with a sublinear or even decreasing dependence on the conductance, and an inverted dependence on the electron and hole components [Ruby 15b].

An example of STM spectroscopy images using superconducting tips is shown in Fig. 2.6. The scan over clean Pb (orange line) shows a suppressed conductance for  $|eV| \lesssim 2.6$  mV, indicating a gap  $\Delta \sim 1.3$  mV. The subgap resolution is improved compared to the early experimental data shown in Fig. 2.4. For the new data, clear resonances are visible when the STM tip scans above Mn adatoms (black line).

The scan in Fig. 2.6 shows data at a sample bias  $|eV| \gtrsim \Delta$  and naively one might expect a pair of peaks at  $eV = \pm(\Delta + \varepsilon_{\text{YSR}})$  due to a single YSR state. However, in the experimental data, multiple peaks are visible. These peaks have been the focus of several studies and are attributed to different magnetic-adatom orbitals that couple to the superconducting substrate, each of which can induce a YSR state [Moca 08, Hatt 15, Ruby 16, Choi 17].

In the case of Fig. 2.6, a Mn impurity is used, and due to its  $S$ -state nature only the  $l = 2$  conduction electrons scatter from the impurity, which leaves five different orbitals [Schr 67, Ruby 16]. The resulting conductance spectrum has been explained in Ref.

[Ruby 16] as follows. The degeneracy of the five  $l = 2$  orbitals can be lifted by the crystal fields at the absorption site, which makes the exchange interaction and the local potential shift orbital dependent, and shifts the energy of the resulting YSR states. Due to the high symmetry of the absorption site scanned in Fig. 2.6, the degeneracy is predicted to be only partially lifted by the crystal field, leaving three degenerate and two non-degenerate orbitals. The partially lifted degeneracy explains the presence of the three shoulders and peaks in Fig. 2.6, and the difference of their peak heights can be explained by the different tunnel coupling strengths for different orbitals, which is dependent on the extension of the orbitals perpendicular to the substrate surface.

Besides the material combination shown in Fig. 2.6, many other combinations have been investigated. A popular choice of superconducting substrate is Pb [Ji 08, Ji 10, Fran 11, Ruby 15b, Hatt 15, Ruby 16, Choi 17, Hatt 17, Ruby 18, Fari 18], but other choices have been explored as well [Yazd 97, Mena 15, Choi 17, Kezi 18]. Notably, for the case of two-dimensional superconducting substrates, an increased range of the YSR wavefunction has been found in agreement with the theoretically predicted change of the power-law decay [Mena 15]. Materials for the magnetic impurities include single atoms such as the transition metals Co, Cr, Fe, and Mn, and the lanthanide Gd [Yazd 97, Ji 08, Ji 10, Mena 15, Ruby 15b, Ruby 16, Choi 17, Choi 18, Ruby 18], as well as magnetic molecules [Fran 11, Hatt 15, Hatt 17, Fari 18].

The excellent control over the magnetic impurities has been demonstrated in a recent experiment. Farinacci et al. used the interplay between the STM tip and a magnetic molecule deposited on the surface of a superconductor to control the vertical position of the molecule above the substrate [Fari 18]. This allows for a continuous control of the exchange coupling strength  $J$  and the spectral position of the YSR state [see Eq. (2.18)]. As we discussed in Sec. 2.2.1, when the YSR state crosses zero energy, the electronic ground-state switches from one with total spin zero to one with total spin one. This quantum phase transition can be probed by measuring the asymmetry between the particle and hole components of the wavefunction, that is inherent to the YSR state. Because the quasiparticle associated with the YSR state switches from occupied to unoccupied at the transition, the asymmetry between electron and hole components is predicted to be discontinuous, and this discontinuity has been reported in the experiment [Fari 18].

In conclusion, magnetic adatoms can be used to induce YSR states in the spectral gap of a superconductor. We have explored several theoretical properties of YSR states that have been discussed since YSR's original papers about half a century ago, and we have reviewed the tremendous experimental progress that has been made over the past two decades.

### 3. Scattering theory

In this chapter, we introduce relevant concepts of scattering theory, employ some of these concepts to analyze toy models of superconducting wires, and review a concatenation method that is used in later chapters.

Scattering theory can be applied in many contexts. In this thesis, we are interested in geometries similar to the one shown in Fig. 3.1, where two leads are attached to a scattering region. We assume that the leads are noninteracting and coherent. Furthermore, up to chapter 6, we assume that the leads are translationally invariant along  $x$ , in which case the solutions are plane waves. In section 6, we generalize this picture to two (three) dimensional leads with a circular (spherical) interface between the scattering region and the leads.

Scattering theory has been discussed extensively in the literature, including the derivations and results presented in this chapter, see for example [Datt 97, Saku 94, Thom 15]. Here, our goal is provide an introduction that covers the aspects that are relevant for the later chapters.

#### 3.1. Definition of the $S$ -matrix for linear geometries

In order to define the scattering matrix of the scattering region shown in Fig. 3.1, we define the Hamiltonian

$$\hat{H}_{\text{linear}} = \hat{H}_{\text{lead}} + \hat{V}(\mathbf{r}), \quad (3.1)$$

where  $\hat{H}_{\text{lead}}$  describes the leads and  $\hat{V}$  is a scattering potential that has support in the scattering region only, that is for  $0 < x < L$ . We assume that  $\hat{H}_{\text{lead}}$  has the left- and right-propagating solutions  $\phi_{-, \alpha}(\mathbf{r}, \varepsilon)$  and  $\phi_{+, \alpha}(\mathbf{r}, \varepsilon)$ , respectively, and the index  $\alpha$  runs over the available propagating modes. Furthermore, we choose  $\phi_{\pm, \alpha}$  to be normalized to unit probability current in the longitudinal direction. The system described by Eq. (3.1) covers the models used in chapters 4 and 5.

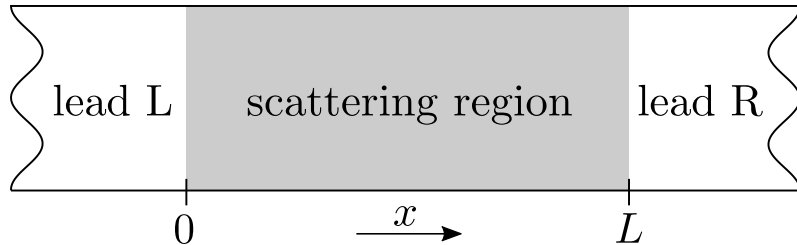


Figure 3.1.: Sketch of a scattering region of length  $L$  contacted by two leads, one to the left (L) and one to the right (R).

### 3. Scattering theory

---

We expand the wavefunction of the system at energy  $\varepsilon$  as

$$\psi(\mathbf{r}, \varepsilon) = \sum_{\alpha, s=\pm} c_{s,\alpha}^{(L)} \phi_{s,\alpha}(\mathbf{r}, \varepsilon) \quad (3.2)$$

for  $x < 0$ ,

$$\psi(\mathbf{r}, \varepsilon) = \psi_{\text{scatt}}(\mathbf{r}, \varepsilon) \quad (3.3)$$

for  $0 < x < L$  and

$$\psi(\mathbf{r}, \varepsilon) = \sum_{\alpha, s=\pm} c_{s,\alpha}^{(R)} \phi_{s,\alpha}(\mathbf{r}, \varepsilon) \quad (3.4)$$

for  $x > L$ . The coefficients  $c_{s,\alpha}^{(L)}$  and  $c_{s,\alpha}^{(R)}$  are restricted by the wavefunction matching conditions at the interfaces at  $x = 0$  and  $x = L$ .

The matching conditions relate the modes exiting into the leads to the ones incoming from the leads. This allows us to define the scattering matrix  $S$  as

$$\begin{pmatrix} \mathbf{c}_+^{(R)} \\ \mathbf{c}_-^{(L)} \end{pmatrix} = S \begin{pmatrix} \mathbf{c}_+^{(L)} \\ \mathbf{c}_-^{(R)} \end{pmatrix} \quad (3.5)$$

where  $\mathbf{c}_\pm^{(L/R)}$  are vectors over the index  $\alpha$ . In the above representation, the scattering matrix takes the form

$$S = \begin{pmatrix} t & r' \\ r & t' \end{pmatrix}. \quad (3.6)$$

Here  $t$  and  $t'$  can be interpreted as the transmission matrices, and  $r$  and  $r'$  as the reflection matrices for solutions incoming from the left and right, respectively. Because the wavefunctions are normalized to unit probability current, the scattering matrix has to be unitary, that is

$$S^\dagger S = \mathbb{1}, \quad (3.7)$$

where  $\mathbb{1}$  is the identity matrix.

A variety of methods exists to calculate scattering matrices, and in the following we will detail some of them. A common approach is to divide the scattering region of interest into subregions, calculate the scattering matrices of the subregions and then combine the solution into the scattering matrix of the full scattering region. To perform such a divide-and-conquer approach, it is useful to know how to concatenate the scattering matrices of two subsequent regions. Let us define two scattering regions  $A$  and  $B$  located at  $0 < x < L_A$  and  $L_B < x < L$ , respectively, with  $L_A < L_B$ , and assume that we know the scattering matrices  $S_A$  and  $S_B$  of the two regions. The coefficients  $c_{\pm,\alpha}^{(R)}$  from  $A$  can be identified with the coefficients  $c_{\pm,\alpha}^{(L)}$  from  $B$ , and by using relation (3.5) the scattering matrix for the combined region reads

$$S_{AB} = S_A \otimes S_B = \begin{pmatrix} t_B R t_A & r'_B + t_B R r'_A t'_B \\ r_A + t'_A r_B R t_A & t'_A (1 + r_B R r'_A) t'_B \end{pmatrix}, \quad (3.8)$$

with  $R = 1/(1 - r'_A r_B)$ . Here, we neglect evanescent modes in between the leads and adopt the notation from Ref. [Sbie 16].

The factor  $R$  can be interpreted as the geometric series of multiple reflections between  $A$  and  $B$ . Furthermore, if  $r'_A r_B$  has an eigenvalue 1, an incoming state will be mapped back to itself after reflecting from  $A$  and  $B$  and consequently a bound state appears. More formally the condition for a bound state to appear reads

$$\det(r'_A r_B - 1) = 0, \quad (3.9)$$

where  $\det$  denotes the determinant.

## 3.2. Application to the Kitaev chain

In this section, we apply the previously outlined scattering approach to the continuum version of the Kitaev chain, as well as a one dimensional  $s$ -wave superconductor. The Kitaev chain is a simple model introduced by Kitaev in 2001, which hosts Majorana bound states at its ends [Kita 01]. In contrast, an  $s$ -wave superconductor is expected to be trivial and generically no zero-energy modes are expected to appear.

The models and results discussed in this section have been extensively analyzed in the literature, see for example [Andr 64, Kita 01, Duck 11, Brou 11a, Alic 12]. Our goal is to apply the scattering approach to a simple known model and illustrate central concepts that we use in the analysis of the low-energy excitations in chapters 4, 5 and 6.

We define the models by the BdG Hamiltonian

$$\hat{H}_{1d} = \begin{pmatrix} \xi_{\hat{k}} & \Delta^*(-\hat{k}) \\ \Delta(\hat{k}) & -\xi_{\hat{k}} \end{pmatrix} \quad (3.10)$$

where  $\hbar\hat{k} = -i\hbar\partial_x$  is the quasi-momentum operator along  $x$ ,  $\xi_k = (\hbar k)^2/2m - \mu$  is the normal metal dispersion with chemical potential  $\mu = k_F^2/2m$  and mass  $m$ , and  $\Delta(k)$  is the pairing potential. The BdG spinor takes the form  $(u(x), v(x))^T$ , consisting of electron and hole components.

We consider two cases of the pairing potential. For case (i), an  $s$ -wave superconductor, we set  $\Delta(\hat{k}) = i\Delta$ , which for later convenience makes the gauge choice of a purely complex pairing potential, and the electron and hole components are from the spin-up and spin-down bands, respectively. For a physical system a second copy of (3.10) has to be taken in order to account for spin-down electrons and spin-up holes. For case (ii), a  $p$ -wave superconductor, we set  $\Delta(\hat{k}) = i\Delta'\hbar\hat{k}$  and assume a spin-polarized material with spin-triplet pairing, in which case we only require a single copy of  $\hat{H}_{1d}$ . In the following analysis we set  $\hbar = 1$  and consider the case of a superconductor in the weak-coupling limit,  $|\Delta(k_F)| \ll \mu$ . Without loss of generality we choose the gauges  $\Delta > 0$  and  $\Delta' > 0$ .

Case (ii) is a special case of Eq. (2.3). Consequently, for  $\mu > 0$ , the  $\Gamma$ -point lies below the Fermi level and the system enters a phase of topological superconductivity.

In order to confirm the presence of a Majorana bound state, we require a solution that is invariant under particle-hole symmetry  $\hat{C}\hat{H}_{1d}\hat{C}^\dagger = -\hat{H}_{1d}$ , with the particle-hole conjugation operator  $\hat{C}$  [Kita 09]. For our choice of gauge,  $\hat{C}$  takes the shape

$$\hat{C} = \tau_x \mathcal{K}. \quad (3.11)$$

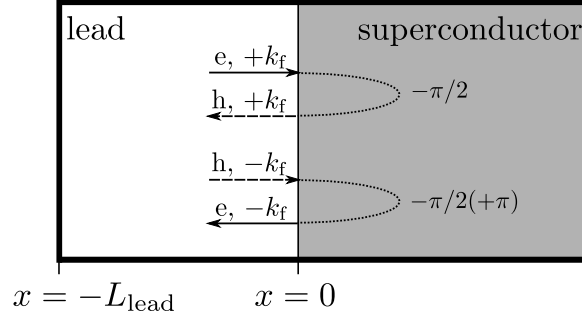


Figure 3.2.: Sketch of a semi-infinite one-dimensional superconductor connected to a lead of length  $L_{\text{Lead}}$ . Andreev reflection processes are shown for an incoming electron (top) and an incoming hole (bottom). On the right, the phases picked up for incoming quasiparticles at  $\varepsilon = 0$  are shown. In the case of a  $p$ -wave superconductor a phase shift  $\pi$  has to be added for the bottom process.

Next, we find the eigenstates of Equation (3.10) by using a plane wave ansatz  $e^{ikx}$ . This yields the eigenenergies

$$\varepsilon = \pm \sqrt{\xi_k^2 + |\Delta(k)|^2}, \quad (3.12)$$

and upon linearising  $\xi_k$  around the Fermi level the (unnormalized) eigenstates

$$\psi_{\pm,s}(x) = \begin{pmatrix} 1 \\ \frac{\Delta(\pm k_F)}{|\Delta(k_F)|} e^{-is\eta(\varepsilon)} \end{pmatrix} e^{\pm[ik_F x - sx/\xi(\varepsilon)]}, \quad (3.13)$$

where  $s = \pm 1$ ,  $k_F = \sqrt{2m\mu}$  is the wave number at the Fermi level in the normal state and

$$\eta(\varepsilon) = \arccos \frac{\varepsilon}{|\Delta(k_F)|}, \quad (3.14)$$

$$\xi(\varepsilon) = \frac{k_F/m}{\sqrt{1 - |\varepsilon/\Delta(k_F)|^2}}. \quad (3.15)$$

Because  $\xi_k^2$  is large unless  $k \sim k_F$ , the dispersion of the bulk has a gap  $|\Delta(k_F)|$  for both  $s$ -wave and  $p$ -wave superconductors, and the in-gap wavefunctions decay exponentially at a length scale  $\xi(\varepsilon)$ .

In order to discuss the boundary modes, we terminate the 1d-system as illustrated in Fig. 3.2. We restrict the superconducting region to  $x > 0$  and connect a lead at  $x = 0$  with a normal state Hamiltonian  $H_{\text{lead}} = \xi_k \tau_z$  that is terminated at  $x = -L_{\text{lead}}$  by the boundary condition of a vanishing wavefunction for  $x < -L_{\text{lead}}$ .

Inside the lead, we define the solutions propagating in  $\pm x$ -direction by

$$\phi_{\pm,e}(x, \varepsilon) = \frac{e^{\pm ik_F x}}{\sqrt{k_F/m}} \begin{pmatrix} 1 \\ 0 \end{pmatrix}, \quad (3.16)$$

$$\phi_{\pm,h}(x, \varepsilon) = \frac{e^{\mp ik_F x}}{\sqrt{k_F/m}} \begin{pmatrix} 0 \\ 1 \end{pmatrix}. \quad (3.17)$$

Here we assume that  $|\varepsilon| \lesssim \Delta(k_F)$  and short leads with  $\Delta mL/k_F \ll 1$  such that we can approximate the wavenumbers by  $k_F$ . The wavefunctions (3.16) and (3.17) are normalized to unit probability current  $j_P[\psi](x) = [\psi^*(x)\partial_x\psi(x) - \psi(x)\partial_x\psi^*(x)]/2mi$ . The overall wavefunction inside the lead takes the shape

$$\psi(\mathbf{r}, \varepsilon) = \sum_{\substack{s=\pm \\ \tau=e,h}} c_{s,\tau} \phi_{s,\tau}(x, \varepsilon). \quad (3.18)$$

Next, we define the scattering matrix at the left and right side of the lead for in-gap energies. Because no transmission is possible at both sides, for subgap energies, it is sufficient to only consider the reflection matrices. At  $x = -L_{\text{lead}}$ , we have

$$\begin{pmatrix} c_{+,e} \\ c_{+,h} \end{pmatrix} = r'_N \begin{pmatrix} c_{-,e} \\ c_{-,h} \end{pmatrix}, \quad (3.19)$$

$$r'_N = \begin{pmatrix} e^{2ik_F L_{\text{lead}}} & 0 \\ 0 & e^{-2ik_F L_{\text{lead}}} \end{pmatrix}. \quad (3.20)$$

At the lead-superconductor interface, we take the Andreev approximation,  $|\Delta(k_F)| \ll \mu$ . In this case the wavenumber has to be approximately conserved and one can read off the reflection amplitudes from (3.13). For subgap energies, we get

$$\begin{pmatrix} c_{-,e} \\ c_{-,h} \end{pmatrix} = r_S \begin{pmatrix} c_{+,e} \\ c_{+,h} \end{pmatrix}, \quad (3.21)$$

$$r_S = \begin{pmatrix} 0 & \frac{\Delta^*(-k_F)}{|\Delta(k_F)|} e^{-i\eta(\varepsilon)} \\ \frac{\Delta(k_F)}{|\Delta(k_F)|} e^{-i\eta(\varepsilon)} & 0 \end{pmatrix}. \quad (3.22)$$

Thus at the interface, electrons are reflected as holes, while no normal reflection into electrons is present, and vice versa holes are reflected into electrons only. The reflection of electrons into holes and vice versa is known as Andreev reflection. For the case of an  $s$ -wave superconductor it can be interpreted as a spin-up electron entering the superconductor and forming a cooper pair with another spin-down electron. This process leaves a spin-down hole that travels back into the normal metal lead [Andr 64].

Possible bound states are obtained by the bound state condition (3.9) upon identifying  $r'_A$  and  $r_B$  with  $r'_N$  and  $r_S$ , respectively. Evaluating the determinant leads to

$$1 = \frac{\Delta(k_F)\Delta^*(-k_F)}{|\Delta(k_F)|^2} e^{-2i\eta(\varepsilon)}. \quad (3.23)$$

Intuitively, Eq. (3.23) can be understood as the requirement that a phase that is a multiple of  $2\pi$  has to be picked up during the closed cycle where an electron is Andreev reflected at the interface as an hole, makes a round trip in the lead, is Andreev reflected back into an electron and makes a final round trip as an electron to the initial state. The phases  $\pm(2k_F L + \pi)$  picked up by the electron and hole during the round-trip in the lead cancel each other.

Next, we solve Eq. (3.23) for the two types pairing potentials. In case of an  $s$ -wave pairing potential we have  $\Delta(k) = \Delta$  and obtain  $\varepsilon = \pm\Delta$ , hence no in-gap states are

present. However, for a  $p$ -wave superconductor the fraction in Eq. (3.23) yields a minus sign and a single solution emerges at  $\varepsilon = 0$ . In the limit  $L_{\text{lead}} \rightarrow 0$ , the bound state wavefunction reads

$$|\psi_0(x)\rangle = \begin{pmatrix} 1 \\ 1 \end{pmatrix} \sin(k_F x) e^{-x/\xi(0)}, \quad (3.24)$$

for  $x > 0$  and zero elsewhere.

The wave function (3.24) has the special property of being invariant under particle-hole conjugation (3.11) and hence is a Majorana quasiparticle. Its amplitude rapidly oscillates at the Fermi-wave number and decays exponentially at a scale of the coherence length  $\xi(0)$ .

In conclusion, while we found a zero-energy Majorana bound state for the  $p$ -wave pairing case, no in-gap states are present in the  $s$ -wave case. The appearance of the Majorana bound state can be traced back to a closed cycle of two normal reflections and two Andreev reflections. While the quasiparticles pick up cancelling phases during normal reflections, the phases picked up in the Andreev process do not cancel. In the  $s$ -wave case this leads to no in-gap states, while in the  $p$ -wave case an additional  $\pi$ -phase is picked up because the pairing potential is odd in momentum, and a zero-energy state becomes possible.

### 3.3. Thin-slice concatenation method

In section 3.2 we obtained the scattering matrix by calculating the eigenstates in the scattering region and matching these eigenstates with the modes in the leads. Often the eigenstates of a scattering region are not easily accessible, for example in the presence of disorder, and other approaches are required. In this section, we review an approach that perturbatively calculates the scattering matrix of thin slices of the scattering region, and then concatenates these slices to obtain the total scattering matrix. This type of integration scheme has been previously used to tackle a variety of problems, such as the study of disordered wires with unconventional superconductivity [Brou 03], the conductivity scaling in graphene [Bard 07] and Weyl semimetals [Sbie 14], and the phase diagram of the Hamiltonian (2.8) in the presence of disorder [Brou 11b].

Consider a system described by the Hamiltonian (3.1), with a geometry as shown in Fig. 3.1. We cut the scattering region  $0 < x < L$  into  $N$  slices according to Fig. 3.3, and in between the gray slices the scattering potential  $\hat{V}(\mathbf{r})$  is absent. This system is described by the Hamiltonian

$$\hat{H}_{\text{slice}} = \hat{H}_{\text{lead}} + \frac{1}{2} \sum_{j=0}^{N-1} \left\{ \delta_{\text{slice},j}(x), \hat{V}(\mathbf{r}) \right\}, \quad (3.25)$$

where the braces denote the anticommutator and  $\delta_{\text{slice},j}(x) = 1$  for  $x_j < x < x_j + \delta L - \delta x$ , with  $x_j = j\delta L$ , and  $\delta L = L/N$ ; and  $\delta_{\text{slice},j}(x) = 0$  elsewhere. The anticommutator is required because  $\hat{V}(\mathbf{r})$  may include derivatives due to effects such as spin-orbit coupling. The thickness of the white slices is  $\delta x$ . Inside these slices, the left- and right-propagating modes are  $\phi_{\pm,\alpha}(\mathbf{r}, \varepsilon)$ , as introduced below Eq. (3.1), and we neglect evanescent modes within a semiclassical approximation, assuming that these decay sufficiently fast on the relevant scattering length scales such as the coherence length in Sec. 3.2. The white slices

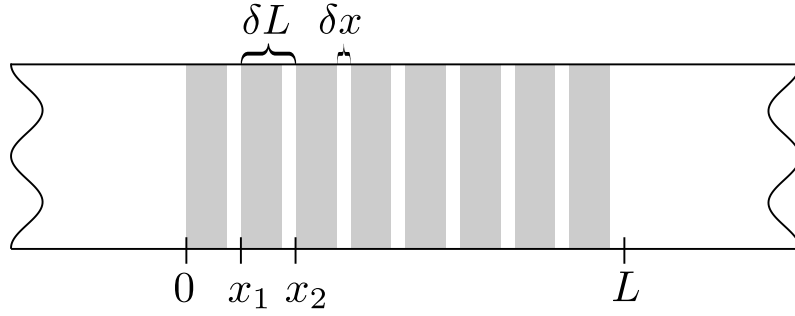


Figure 3.3.: Slicing of the scattering region. The scattering potential  $\hat{V}(\mathbf{r})$  is present in the grey areas only. The gray slices have a thickness  $\delta L - \delta x$ , and the white region in between a thickness  $\delta x$ . Taking the limit  $\delta x \rightarrow 0$  recovers the geometry of Fig. 3.1.

are present in order to define the propagating modes, and we take the limit  $\delta x/\delta L \rightarrow 0$  later.

Denote the scattering matrix of the  $j$ th gray slice by  $S_j$ . If  $\delta L$  is sufficiently small,  $S_j$  can be calculated perturbatively in lowest-order Born approximation. We give a derivation of this approximation in Appendix A, which yields

$$S_j = \mathbf{1} - i\mathcal{T}^{(j)}, \quad (3.26)$$

where

$$\mathcal{T}_{\nu,\mu}^{(j)} = \frac{1}{2} \int d\mathbf{r} \phi_{\nu}^{\dagger}(\mathbf{r}, \varepsilon) \left\{ \delta_{\text{slice},j}(x), \hat{V}(\mathbf{r}) \right\} \phi_{\mu}(\mathbf{r}, \varepsilon), \quad (3.27)$$

and  $\mu, \nu$  are multi indices over  $(\pm, \alpha)$ . Because the scattering matrices have to be unitary, Eq. (3.26) can be recast into the unitarized Born approximation

$$S_j = \frac{\mathbf{1} - \mathcal{T}^{(j)}/2}{\mathbf{1} + i\mathcal{T}^{(j)}/2}. \quad (3.28)$$

The scattering matrix  $S(L, \varepsilon)$  across the full scattering region  $0 < x < L$  is obtained by

$$S(L, \varepsilon) = \lim_{N \rightarrow \infty} S_0 \otimes S_1 \otimes \cdots \otimes S_{N-1}, \quad (3.29)$$

in the limit  $\delta L \rightarrow 0$  and for  $\delta x = 0$ .

In order to guarantee numerical convergence of the limit in Eq. (3.29), we choose  $\delta L$  small compared to the involved longitudinal scattering length-scales.

In chapters 4 and 5, we will make use of the thin-slice concatenation method described here.



## 4. Renormalization effects in spin-polarized metallic wires proximitized by a superconductor: A scattering approach

This chapter has been published as Ref. [Kien 18].

As we discussed in Sec. 2.1.3, experimental realizations of systems that host Majorana bound states make use of the proximity effect by coupling a superconductor to an effectively spin-polarized normal wire, such as a semiconducting wire in a large magnetic field [Mour 12, Das 12, Chur 13, Deng 16, Albr 16, Chen 17, Zhan 18] or a ferromagnetic wire formed by a linear chain of magnetic adatoms placed on a superconducting substrate [Nadj 14, Ruby 15a, Pawl 16, Feld 17]. In both cases, a crucial ingredient is spin-orbit coupling, because it allows spin-singlet  $s$ -wave Cooper pairs in the superconducting substrate to be converted into spin-polarized  $p$ -wave pairs in the proximitized wire.

Besides the zero-energy peaks that we discussed in Sec. 2.1.3, experiments can also access the localization length of the Majorana bound states. In case of the adatoms chains, scanning tunneling microscopy is used to detect the zero-bias peaks at the chain ends, and the localization length can be inferred from the spatially resolved conductance maps [Nadj 14, Ruby 15a, Pawl 16, Feld 17]. For the case of semiconductor-based experiments, the hybridization of Majorana bound states at the opposite ends can be used to infer the localization length [Albr 16]. In Sec. 3.2 we saw that for an energy gap of size  $\varepsilon_{\text{gap}}$  and a Fermi velocity  $v$ , a naive expectation for the localization length is that the product  $\varepsilon_{\text{gap}}l_{\text{maj}} \sim \hbar v$ . Surprisingly, in the experiments based on adatom chains and some of the semiconductor-based experiments [Das 12], the observed value of this product was significantly below this value [Dumi 15].

The anomalously small value of  $\varepsilon_{\text{gap}}l_{\text{maj}}$  could be explained by strong coupling between the wire and the superconductor, which leads to a renormalization of the properties of the Majorana bound states in adatom-chain-based setups [Peng 15, Das 15] as well as semiconductor-based setups [Stic 17, Stan 17]. In both cases, the qualitative picture for this renormalization is that a significant part of the spectral weight of the Majorana is shifted into the superconductor and as a result the velocity along the wire is renormalized towards small values.

In this chapter, we investigate the renormalization effects for a superconductor strongly coupled to a spin-polarized wire — where the spin polarization can be a consequence of the use of half-metallic materials [Groo 83, Schw 86, Park 98, Son 06], the use of chains of magnetic adatoms [Nadj 14, Ruby 15a, Pawl 16, Feld 17], or of the application of a magnetic field. We show that the renormalization of the velocity exists independently of the existence of a proximity-induced minigap  $\varepsilon_{\text{gap}}$  in the wire and the Majorana bound states. Renormalization effects are present even if  $\varepsilon_{\text{gap}}$  is much smaller than the bulk

superconducting gap  $\Delta$ . Such a situation drastically differs from a conventional normal-metal–superconductor junction in the absence of a magnetic field, where a large spectral weight inside the superconductor coincides with the short-junction limit for which  $\varepsilon_{\text{gap}}$  and  $\Delta$  are of comparable magnitude.

Our theoretical approach complements that of Refs. [Peng 15, Das 15], which uses a large tunnel matrix element to model the strong-coupling limit of a normal-metal–superconductor hybrid. Instead, we employ a semiclassical wavefunction approach, and characterize the normal-metal–superconductor interface in terms of its transparency, in which case the strongest coupling naturally appears for an ideal interface with unit transparency. For such an ideal interface, the coupling of normal metal and superconductor is strongest when  $\Delta \ll \hbar v/D_N$ , where  $v$  is the Fermi velocity in the absence of coupling to the superconductor and  $D_N$  the transverse dimension of the normal metal. Our method is similar to the one used in the analysis of a semiconductor-wire model in Ref. [Stic 17], and extends previous work on the weak-coupling limit [Duck 11].

### 4.1. Semiclassical interpretation of the renormalization

The wavefunction approach allows for an instructive semiclassical picture of the renormalization effects. In this picture, a delayed specular reflection of electrons in the normal metal at the superconductor interface lowers the longitudinal velocity, as shown in Fig. 4.1. At an ideal normal-metal superconductor interface, this reflection process consists of three phases: (1) An electron incident from the normal metal at angle  $\theta$  is transmitted into the superconductor. (2) The transmitted electron is Andreev reflected as a hole. In contrast to the electron, this hole cannot re-enter the spin-polarized normal metal because it has the wrong spin. Instead, it is specularly reflected at the normal-metal–superconductor interface. (3) Finally, the reflected hole is Andreev reflected into an electron with the right spin, which is subsequently transmitted into the normal metal. Because the penetration depth into the superconductor is finite, the electron accumulates a delay  $\sim 2\hbar/\Delta$  during the three phases of this reflection process. For a normal metal wire of thickness  $D_N$  the electron travels a distance  $2D_N \tan \theta$  in the longitudinal direction between subsequent reflection events within a time  $2D_N/v \cos \theta$ . Hence we obtain the renormalized velocity

$$v_x \approx \frac{\Delta}{\hbar} D_N \tan \theta \quad (4.1)$$

in the limit of strong coupling  $\Delta \ll \hbar v/D_N$ .

For a non-ideal normal-metal–superconductor interface a second reflection channel, direct specular reflection without a delay, is added in parallel to this delayed reflection process. We emphasize that the velocity renormalization is caused by the delay for the *normal* reflection; processes that lead to Andreev reflection of majority electrons into majority holes or vice versa are not involved in this renormalization.

Spin-orbit coupling in the normal metal and/or the superconductor enables Andreev reflection of majority electrons into majority holes. As a result a small minigap  $\varepsilon_{\text{gap}}$  opens up in the spectrum of the normal metal and Majorana bound states appear at the wire ends. The localization length of the Majorana bound state  $l_{\text{maj}} \sim \hbar v_x/\varepsilon_{\text{gap}}$ , with  $v_x$  the renormalized normal-state velocity. In the strong coupling limit, the renormalization of

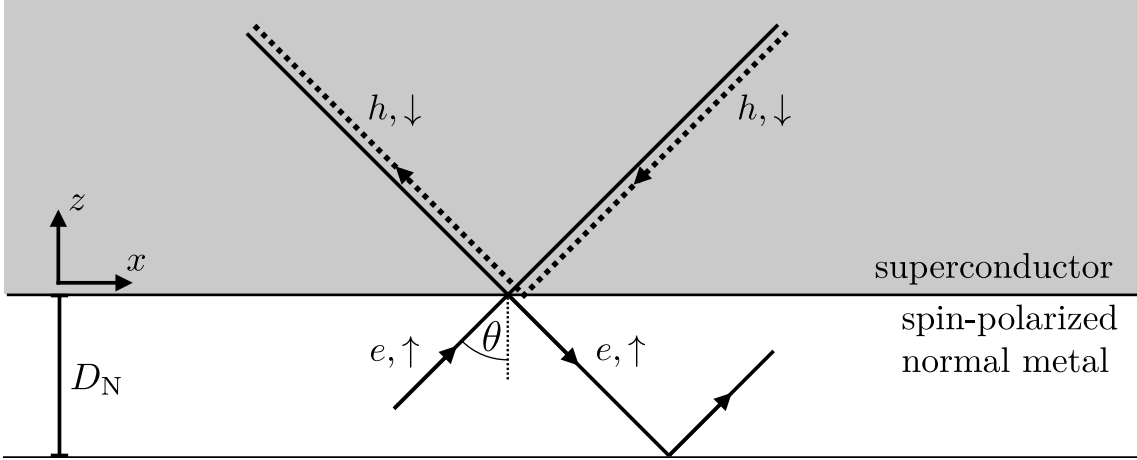


Figure 4.1.: Spin-polarized normal-metal wire of thickness  $D_N$  (white) with one superconducting (grey, top) boundary and one insulating boundary (bottom). In the absence of spin-orbit coupling specular (normal) reflection at the normal-metal–superconductor interface involves a double Andreev reflection process in which an Andreev reflected minority hole is specularly back-reflected into the superconductor. The time delay incurred in this process slows down electrons propagating in the normal metal.

the velocity  $v_x$  leads to a strong renormalization of the product  $\varepsilon_{\text{gap}}l_{\text{maj}}$ . Upon comparing expressions for the weak and strong-coupling limits, we find that  $\varepsilon_{\text{gap}}$  is renormalized but not the localization length, in accordance with the analysis of Refs. [Peng 15, Das 15].

The outline of the remainder of this chapter is as follows: In Sec. 4.2 we introduce a model of a spin-polarized normal metal proximity coupled to a superconductor in a planar geometry. In Sec. 4.2.1, we derive the propagating low-energy modes and the dispersion  $\varepsilon(k_x)$  in the absence of spin-orbit coupling. The renormalized velocity  $v_x$  is obtained via the relation  $v_x = \hbar^{-1}|d\varepsilon/dk_x|$  and compared to a classical prediction. We include spin-orbit coupling in Sec. 4.2.2 and study the Majorana localization length and minigap in the limits of an ideal and non-ideal interface. Results for a spin-polarized normal metal with a cylindrical cross-section are presented in Sec. 4.3.2.

## 4.2. Planar geometry

We consider a normal-metal (N) strip coupled to a superconductor (S). Coordinate axes are chosen such that the NS interface coincides with the  $x$  axis, see Fig. 4.1, the superconductor occupies the half space  $z > 0$ , and the normal metal is in the region  $-D_N < z < 0$ . The  $4 \times 4$  BdG Hamiltonian reads

$$\hat{\mathcal{H}} = \begin{pmatrix} H_0 & i\sigma_2\Delta e^{i\phi\theta(z)} \\ -i\sigma_2\Delta e^{-i\phi\theta(z)} & -H_0^* \end{pmatrix}, \quad (4.2)$$

#### 4. Renormalization effects in spin-polarized metallic wires proximitized by a superconductor: A scattering approach

---

for a BdG spinor  $(u_\uparrow, u_\downarrow, v_\uparrow, v_\downarrow)^T$  consisting of particle and hole wavefunctions. Here,  $\sigma_i$  with  $i = 1, 2, 3$  are the Pauli matrices in spin subspace,  $\Delta e^{i\phi}$  is the superconducting order parameter, and  $\theta(z)$  the Heaviside step function. The  $2 \times 2$  normal-state Hamiltonian  $H_0$  is

$$H_0 = \frac{\mathbf{p}^2}{2m} + V(z) + \frac{\hbar^2 w}{m} \delta(z) + H_{\text{so}}, \quad (4.3)$$

where  $\mathbf{p}$  is the momentum operator,  $m$  is the electron mass, which we take to be the same in the N and S parts of the system,  $V(z)$  is a spin-dependent potential,  $(\hbar^2 w/m)\delta(z)$  a potential barrier at the NS interface, and  $H_{\text{so}}$  the spin-orbit interaction. For the spin-dependent potential  $V(z)$ , we take different expressions in the normal and superconducting parts of the system,

$$V(z) = -\frac{\hbar^2 k_S^2}{2m} \quad (4.4)$$

when  $z > 0$  and

$$V(z) = -\frac{\hbar^2}{2m} \begin{pmatrix} k_\uparrow^2 & 0 \\ 0 & -\kappa_\downarrow^2 \end{pmatrix} + V_{\text{conf}}(z) \quad (4.5)$$

when  $z < 0$ . Here,  $k_S$  and  $k_\uparrow$  are the Fermi wavenumbers of the superconductor and the majority spin band,  $-\kappa_\downarrow^2/2m$  is the Fermi level of the depleted minority band, measured from the band bottom in the absence of spin-orbit coupling, and  $V_{\text{conf}}(z)$  is a confining potential modeling the sample boundary at  $z = -D_N$ ,  $V_{\text{conf}}(z) = 0$  for  $z > -D_N$  and  $V_{\text{conf}}(z) = \infty$  for  $z < -D_N$ . Finally, the spin-orbit coupling is taken to be linear in momentum,

$$H_{\text{so}} = \frac{\hbar}{2} \sum_j [\mathbf{p} \boldsymbol{\Omega}_j(z) \sigma_j + \sigma_j \boldsymbol{\Omega}_j(z) \mathbf{p}], \quad (4.6)$$

where the spin-orbit coupling strength

$$\boldsymbol{\Omega}_j(z) = \boldsymbol{\Omega}_{Sj} \theta(z) + \boldsymbol{\Omega}_{Nj} \theta(-z) \quad (4.7)$$

is piecewise constant in the N and S regions. Spin-orbit coupling is assumed to be weak, so that it can be treated in first-order perturbation theory.

The normal-state majority-carrier transparency of the interface depends on the Fermi velocities  $v_\uparrow = v = \hbar k_\uparrow/m$  and  $v_S = \hbar k_S/m$ , the strength  $w$  of the surface  $\delta$ -function potential, and the momentum component  $\hbar k_x$  parallel to the interface. In the absence of spin-orbit coupling, the corresponding reflection and transmission amplitudes at the Fermi energy  $\varepsilon = 0$  are [Kupf 11]

$$t_\uparrow(k_x) = \frac{2\sqrt{k_\uparrow z k_{Sz}}}{2iw + k_\uparrow z + k_{Sz}}, \quad (4.8)$$

$$r_\uparrow(k_x) = -1 + t_\uparrow(k_x) \sqrt{k_\uparrow z / k_{Sz}}, \quad (4.9)$$

$$r'_\uparrow(k_x) = -1 + t_\uparrow(k_x) \sqrt{k_{Sz} / k_\uparrow z}, \quad (4.10)$$

where

$$k_\uparrow z = \sqrt{k_\uparrow^2 - k_x^2}, \quad k_{Sz} = \sqrt{k_S^2 - k_x^2}. \quad (4.11)$$

(The amplitudes  $r_\uparrow$  and  $r'_\uparrow$  describe reflection for majority electrons coming from the N and S parts of the system, respectively.) Minority spins coming from  $z > 0$  are reflected with reflection amplitude

$$\begin{aligned} r'_\downarrow(k_x) &= e^{i\varphi_\downarrow(k_x)} \\ &= \frac{k_{S_z} - i\kappa_{\downarrow z} - 2iw}{k_{S_z} + i\kappa_{\downarrow z} + 2iw}, \end{aligned} \quad (4.12)$$

where  $\kappa_{\downarrow z} = \sqrt{\kappa_\downarrow^2 + k_x^2}$  and we neglect terms exponentially suppressed in  $\kappa_{\downarrow z} D_N$ .

This model describes semiconductor wires in a large Zeeman field as well as half-metallic (ferromagnetic) wires, both coupled to a superconductor. In the former case spin-orbit coupling is typically assumed to exist inside the semiconductor, but not in the superconductor [Lutc 10, Oreg 10]; in the latter case, spin-orbit coupling is usually taken to be in the superconductor, but not in the half-metallic wire [Duck 11, Chun 11].

### 4.2.1. Velocity renormalization

We first consider the system under consideration in the presence of superconductivity, but without spin-orbit coupling. The superconducting gap confines carriers with excitation energy  $|\varepsilon| < \Delta$  to the normal region, so that the N region effectively becomes a conducting wire of thickness  $D_N$ .

Without spin-orbit coupling, reflections at the NS interface are purely normal; Andreev reflections are ruled out because they would require a spin flip process. Nevertheless, the presence of the superconductor can lead to a strong renormalization of the carrier velocity. To see this explicitly, we construct the wavefunction of a majority electron at excitation energy  $\varepsilon$  and momentum  $\hbar k_x$  parallel to the interface,

$$u_\uparrow(x, z) \propto e^{ik_x x} \left[ e^{ik_z(k_x, \varepsilon)z} + r_{ee}(k_x, \varepsilon) e^{-ik_z(k_x, \varepsilon)z} \right]. \quad (4.13)$$

Here

$$k_z(k_x, \varepsilon) = \sqrt{k_\uparrow^2 - k_x^2 + 2m\varepsilon/\hbar^2} \quad (4.14)$$

and  $r_{ee}(k_x, \varepsilon)$  is the reflection amplitude in the presence of the superconductor. In terms of the normal-state reflection and transmission amplitudes of the NS interface the reflection amplitude  $r_{ee}(k_x, \varepsilon)$  reads (in the Andreev approximation  $\hbar^2 k_z^2/2m \gg \Delta$ )

$$\begin{aligned} r_{ee}(k_x, \varepsilon) &= r_\uparrow(k_x) + \frac{t_\uparrow(k_x)^2 e^{-2i\eta(\varepsilon) - i\varphi_\downarrow(k_x)}}{1 - r'_\uparrow(k_x) e^{-2i\eta(\varepsilon) - i\varphi_\downarrow(k_x)}} \\ &= \frac{k_{\uparrow z} - 2iw - ik_{S_z} \tan(\eta + \varphi_\downarrow/2)}{k_{\uparrow z} + 2iw + ik_{S_z} \tan(\eta + \varphi_\downarrow/2)}, \end{aligned} \quad (4.15)$$

where

$$\eta(\varepsilon) = \arccos(\varepsilon/\Delta). \quad (4.16)$$

This result can be easily understood by considering the different paths a majority electron incident on the NS interface from  $z < 0$  can take: Direct normal reflection with amplitude

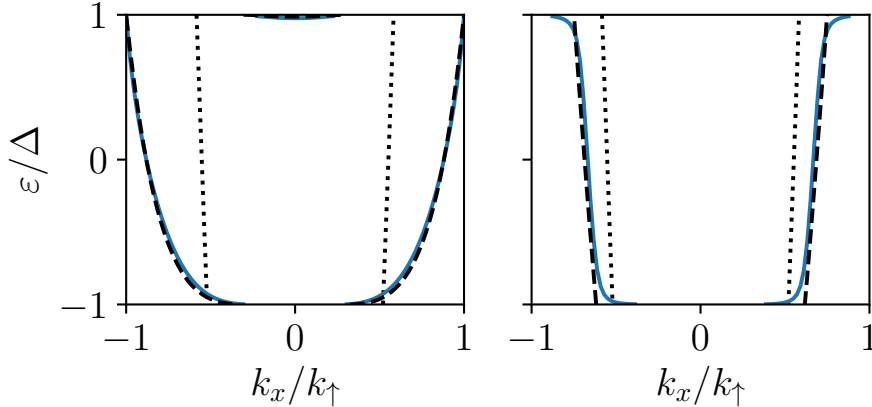


Figure 4.2.: Subgap dispersion relation  $\varepsilon(k_x)$  for a spin-polarized normal wire attached to a superconductor. Only electron-like solutions are shown, hole-like ones are obtained by mirroring the spectrum vertically such that  $\varepsilon \rightarrow -\varepsilon$ . The wire thickness satisfies  $k_\uparrow D_N/\pi = 1.2$ , corresponding to one propagating mode at the Fermi level  $\varepsilon = 0$  in an isolated wire. The solid lines are obtained by numerically solving Eq. (4.17). The left panel shows the dispersion relation for  $k_\uparrow = k_S$ ,  $w = 0$ , corresponding to a fully transparent NS interface; the right panel has  $wm/\hbar k_\uparrow = 1$ , corresponding to an interface with transmission probability  $|t_\uparrow|^2 = 1/2$  for perpendicular incidence. The dashed lines show Eqs. (4.20) (left panel) and (4.25) (right panel), while the dotted lines show the dispersion for a vanishing interface transparency. The magnitude of the superconducting gap is given by  $(\hbar\pi/D_N)^2/2m\Delta = 10$ , well within the validity range of the Andreev approximation. We further set  $\kappa_{F\downarrow}/k_\uparrow = 2$ .

$r_\uparrow$  or entering the superconductor with transmission amplitude  $t_\uparrow$ , Andreev reflection into a minority hole, normal backreflection of the hole into S with amplitude  $r_\downarrow^*$ , finally followed by a second Andreev reflection into a majority electron and transmission into the normal metal. The denominator in Eq. (4.15) describes higher-order processes involving multiple double Andreev reflections. We have assumed  $\kappa_\downarrow D_N \gg 1$ , so that the minority wavefunction component  $u_\downarrow$  decays sufficiently fast away from the NS interface and it is sufficient to restrict ourselves to the majority wavefunction component  $u_\uparrow$ .

The dispersion relation  $\varepsilon(k_x)$  follows by imposing that  $u_\uparrow(x, -D_N) = 0$ , which leads to

$$1 = -e^{2ik_z D_N} r_{ee}(k_z, \varepsilon). \quad (4.17)$$

For a weakly coupled superconductor one has  $r_\uparrow = r_\uparrow' \approx -1$  and  $|t_\uparrow| \ll 1$ , and Eq. (4.17) reproduces the standard quantization rule  $k_z = n\pi/D_N$ ,  $n = 1, 2, \dots$ , and a quadratic dispersion

$$\varepsilon = \frac{\hbar^2}{2m} \left( k_x^2 + \frac{n^2 \pi^2}{D_N^2} - k_\uparrow^2 \right). \quad (4.18)$$

In the opposite limit of an ideal interface with  $t_\uparrow = 1$  and  $r_\uparrow = r'_\uparrow = 0$ , one finds

$$2k_z(\varepsilon)D_N = 2\eta(\varepsilon) + \varphi_\downarrow(k_x) + (2n + 1)\pi. \quad (4.19)$$

If we restrict ourselves to the single-mode regime  $1 \lesssim k_\uparrow D_N/\pi \lesssim 2$ , the Andreev approximation implies that  $(\hbar\pi/D_N)^2/2m \gg \Delta$ , which allows us to neglect the energy dependence on the l.h.s. of Eq. (4.19) and to obtain the dispersion

$$\varepsilon = \pm\Delta \sin \left[ \frac{\varphi_\downarrow(k_x)}{2} - D_N \sqrt{k_\uparrow^2 - k_x^2} \right]. \quad (4.20)$$

The left panel of Fig. 4.2 shows the dispersion for  $k_\uparrow D_N/\pi = 1.2$  for an ideal interface, together with the approximate result (4.20) and the dispersion (4.18) of the isolated wire.

Figure 4.2 clearly shows that the coupling to the superconductor leads to significantly flatter  $\varepsilon$  vs.  $k_x$  curves near  $\varepsilon = 0$ , indicating a strongly renormalized Fermi velocity  $v_x = \hbar^{-1}|d\varepsilon/dk_x|$ . The strong renormalization of the velocity also follows from the approximate dispersion (4.20) for an ideal interface,

$$v_x = \frac{1}{\hbar} \sqrt{\Delta^2 - \varepsilon^2} \frac{k_x D_N}{k_{\uparrow z}} \left( 1 - \frac{1}{\kappa_{\downarrow z} D_N} \right). \quad (4.21)$$

Although we dropped terms exponentially suppressed in  $\kappa_{\downarrow z} D_N$  in Eq. 4.12, we keep the term including  $\kappa_{\downarrow z} D_N$  as it is suppressed by a power law only. Equation (4.21) gives an effective velocity  $v_x$  that is suppressed by a factor  $\Delta/\varepsilon_{\text{kin}}$  compared to the velocity  $\hbar k_x/m$  of an isolated normal wire. Here,  $\varepsilon_{\text{kin}} = \hbar^2 k_\uparrow^2/2m$  is the normal-state kinetic energy. This suppression is consistent with the semiclassical estimate (4.1).

The renormalized velocity is shown in Fig. 4.3 as a function of interface transparency for the same parameter choice as in Fig. 4.2. Starting from the value  $v_x = \hbar k_x/m$  of an isolated wire, the velocity decreases monotonically as a function of interface transparency  $|t_\uparrow|$ , reaching the much smaller value given by Eq. (4.21) at  $|t_\uparrow|^2 = 1$ .

Although the velocity renormalization is strongest for a fully transparent interface, we emphasize that the renormalization exists for arbitrary transparency of the interface, provided  $\Delta$  is small enough, so that a double Andreev reflection from the superconductor takes a sufficiently long time. In fact, the limit of a weakly transparent interface allows for an explicit solution for  $v_x$ , as we now show. The limit of a small junction transparency is realized if  $k_{S_z} \gg k_z$  or  $|w| \gg k_z$ . In this limit one finds

$$r_{\text{ee}} = -\frac{4w^2 + k_{S_z}^2 + ik_z(2w + \varepsilon k_{S_z}/\Delta)}{4w^2 + k_{S_z}^2 - ik_z(2w + \varepsilon k_{S_z}/\Delta)}, \quad (4.22)$$

up to corrections that are small in  $|\varepsilon|/\Delta$ , in  $k_z/|w|$ , or in  $k_z/k_{S_z}$ . For  $|\varepsilon| \ll \Delta$ , the solution of Eq. (4.17) is

$$k_z = \frac{\pi}{D_N} - \frac{\pi(2w + \varepsilon k_{S_z}/\Delta)}{D_N^2(4w^2 + k_{S_z}^2)}, \quad (4.23)$$

which gives the equation

$$\varepsilon = \frac{\hbar^2}{2m} \left( k_x^2 + \frac{\pi^2}{D_N^2} - \frac{2\pi^2(2w + \varepsilon k_{S_z}/\Delta)}{D_N^3(4w^2 + k_{S_z}^2)} - k_\uparrow^2 \right), \quad (4.24)$$

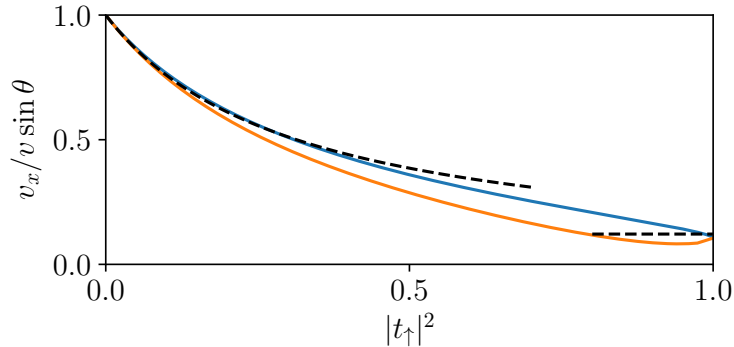


Figure 4.3.: Renormalized velocity as a function of interface transparency  $|t_\uparrow|^2$ . The velocity is normalized to  $v_x^0 = \hbar k_x/m = v \sin \theta$ . The interface barrier is introduced by increasing  $w$  while matching  $k_\uparrow = k_S$  (bright, orange line) and by increasing  $k_S$  at fixed  $w = 0$  (dark, blue line). The solid lines are obtained by numerically solving Eq. (4.17). All other parameters are the same as in Fig. 4.2. The dashed lines show the  $|t_\uparrow|^2 = 1$  approximation of Eq. (4.21) and the small-transparency approximation of Eq. (4.25).

from which the dispersion relation can be obtained. (The  $\varepsilon$ -dependence of  $k_{Sz}$  can be neglected in the limit of small interface transparency because either  $k_S \gg k_\uparrow$ , in which case  $k_{Sz} = k_S$  up to small corrections, or  $|w| \gg k_{Sz}$ , in which case  $k_{Sz}$  drops out of the equation.) Differentiating with respect to  $k_x$  gives the velocity

$$v_x = \frac{v \sin \theta}{1 + |t_\uparrow|^2 \xi_N / 4D_N}, \quad (4.25)$$

at  $\varepsilon = 0$ , where  $\sin \theta = k_x/k_\uparrow$  and  $\xi_N = \hbar^2 k_z / m \Delta = \hbar^2 \pi / m D_N \Delta$  is the transverse coherence length in the normal metal. The strong velocity renormalization sets in when  $\xi_N |t_\uparrow|^2 \gg D_N$ . The small-transparency approximation for the dispersion  $\varepsilon(k_x)$  and the velocity  $v_x$  is illustrated in the right panel of Fig. 4.2 and in Fig. 4.3, respectively, showing that the small-transparency approximation remains useful for interface transparencies  $|t_\uparrow|^2 \lesssim 0.5$ .

From a purely classical point of view, the denominator in Eq. (4.25) is surprising. To understand this, consider the process shown in Fig. 4.1 for a low transparency  $|t_\uparrow|^2$ . From a classical point of view, the electron will spend a time  $T_N \sim D_N/v_\uparrow |t_\uparrow|^2$  in the normal metal before being transmitted through the interface and a time  $T_S \sim \xi/v_S |t_\uparrow|^2$  in the superconducting region. Here, we define the velocities  $v_\uparrow = k_\uparrow/m$  and  $v_S = k_S/m$  and neglect the angle  $\theta$ . In the superconducting region, the distance traveled along  $x$  is zero due to the zero-net displacement processes shown in Fig. 4.1, and thus the velocity is expected to be

$$v_x^{(\text{cl})} \sim \frac{v_\uparrow T_\uparrow}{T_\uparrow + cT_S} \sim \frac{v_\uparrow}{1 + c\xi_N/D_N}, \quad (4.26)$$

with some constant numerical factor  $c$ , and the ratio  $v_\uparrow/v_S$  has been absorbed into  $\xi_N$ .

Eq. (4.26) is clearly inconsistent with Eq. (4.25). The missing factor  $|t_\uparrow|^2$  can be traced back to the coherent scattering in the superconductor: During a single cycle of the double Andreev reflection shown in Fig. 4.6, a phase factor  $e^{i\alpha} = e^{-2i\eta(\varepsilon)} r'_\uparrow (r'_\downarrow)^*$  is picked up. For  $|\varepsilon| \ll \Delta$  and a low transparency, this phase factor becomes  $e^{i\alpha} = -1 + O(|t|^2)$ . Hence multiple double Andreev reflections interfere destructively up to corrections of  $O(|t_\uparrow|^2)$  and the time  $T_S$  is effectively lowered by a factor  $|t_\uparrow|^2$ , which explains the discrepancy between the classical and semiclassical expressions in (4.25) and (4.26).

In Sec. 4.3.2, we show that qualitatively the same results are obtained for a spin-polarized normal metal wire with a cylindrical cross section.

### 4.2.2. Minigap and Majorana localization length

Spin-orbit coupling in the superconductor allows for spin flips and thereby enables Andreev reflections of majority spin electrons into majority spin holes and vice versa. This induces a  $p$ -wave minigap  $\varepsilon_{\text{gap}}$  in the excitation spectrum of the normal wire and zero-energy Majorana bound states form at its ends. This section considers both of these effects and relates the localization length  $l_{\text{maj}}$  of the Majorana bound states and the minigap  $\varepsilon_{\text{gap}}$  to the velocity renormalization calculated in the previous section. The calculation extends that of Ref. [Duck 11], which considered the same problem in the limit of an opaque NS interface, for which there is no velocity renormalization.

We assume that spin-orbit coupling is sufficiently weak so that it can be treated in first-order perturbation theory. Correspondingly, the probability for Andreev reflection off the normal-metal–superconductor interface is small and the induced minigap  $\varepsilon_{\text{gap}}$  in the spectrum of the normal wire much smaller than the bulk superconducting gap  $\Delta$ . For that reason, we neglect corrections to the scattering amplitudes of order  $\varepsilon/\Delta$  in the calculations below.

The starting point of the calculation is an expression for the propagating states in the normal wire in the absence of spin-orbit coupling, normalized to unit flux in the  $x$  direction. To keep the notation simple, we restrict attention to the regime in which there is one propagating mode in the normal-metal wire in the absence of spin-orbit induced Andreev reflection. This mode has transverse wavevector  $k_z$ , which is determined by the quantization condition (4.17). The electron-like scattering states  $|\psi_{e,\pm}\rangle$  propagating in the positive (+) or negative (−)  $x$  direction have the wavefunction components [Kupf 11]

$$u_{\uparrow,\pm}(\mathbf{r}) = e^{\pm ik_x(\varepsilon)x} \frac{e^{ik_z z} + r_{ee} e^{-ik_z z}}{\sqrt{\mathcal{N}} v_x} \quad (4.27)$$

$$v_{\downarrow,\pm}(\mathbf{r}) = -e^{\pm ik_x(\varepsilon)x} \frac{it_\uparrow \tau_\downarrow e^{\kappa_{\downarrow z} z} e^{-i\phi}}{(r'_{\downarrow} + r'_{\uparrow}) \sqrt{\mathcal{N}} v_x}, \quad (4.28)$$

in the normal region  $-D_N < z < 0$ , where

$$k_x(\varepsilon) = \sqrt{k_\uparrow^2 - k_{\uparrow z}^2} + \frac{\varepsilon}{\hbar v_x}, \quad (4.29)$$

with the velocity  $v_x$  taken from the calculation of the dispersion in Sec. 4.2.1, and

$$\tau_\downarrow = \frac{2\sqrt{k_{S_z} k_{\uparrow z}}}{k_{S_z} + ik_{\downarrow z} + 2iw}. \quad (4.30)$$

#### 4. Renormalization effects in spin-polarized metallic wires proximitized by a superconductor: A scattering approach

---

Since we are interested in energies  $|\varepsilon| \ll \Delta$ , we only need to retain the energy dependence in the exponential factors, see the discussion in the previous paragraph. As before, we assume that  $\kappa_{\downarrow z} D_N \gg 1$  so that no hard-wall boundary condition needs to be applied at  $z = -D_N$  for the minority component  $v_{\downarrow, \pm}(\mathbf{r})$ . In the superconducting region, the nonzero wavefunction components are [Kupf 11]

$$\begin{aligned} u_{\uparrow, \pm}(\mathbf{r}) &= \frac{t_{\uparrow} e^{\pm i k_x(\varepsilon)x - z/\xi} (e^{i k_{S_z} z} - e^{-i k_{S_z} z - i\varphi_{\downarrow}})}{(1 + r'_{\uparrow} e^{-i\varphi_{\downarrow}}) \sqrt{\mathcal{N} k_{S_z} v_x / k_{\uparrow z}}}, \\ v_{\downarrow, \pm}(\mathbf{r}) &= - \frac{i t_{\uparrow} e^{\pm i k_x(\varepsilon)x - z/\xi - i\phi} (e^{i k_{S_z} z} + e^{-i k_{S_z} z - i\varphi_{\downarrow}})}{(1 + r'_{\uparrow} e^{-i\varphi_{\downarrow}}) \sqrt{\mathcal{N} k_{S_z} v_x / k_{\uparrow z}}}. \end{aligned} \quad (4.31)$$

Here

$$k_{S_z} = \sqrt{k_S^2 - k_{\uparrow}^2 + k_z^2}, \quad (4.32)$$

$$\xi = \frac{\hbar^2 k_{S_z}}{m\Delta}, \quad (4.33)$$

$$\mathcal{N} = 2D_N + \frac{\text{Im } r_{\text{ee}}}{k_z} + \frac{2\xi_N |t_{\uparrow}|^2}{|r'_{\downarrow} + r'_{\uparrow}|^2}, \quad (4.34)$$

where the transverse coherence length in the normal metal  $\xi_N$  was defined below Eq. (4.25). The factors  $\sqrt{k_{S_z}/k_{\uparrow z}}$  in the denominators of Eq. (4.31) are a consequence of current conservation at the normal-metal–superconductor interface. Similarly, the nonzero wavefunction components of the hole-like scattering states  $|\psi_{h, \pm}\rangle$  are

$$\begin{aligned} v_{\uparrow, \pm}(\mathbf{r}) &= \frac{e^{\mp i k_x(-\varepsilon)x} (e^{-i k_z z} + r_{\text{ee}}^* e^{i k_z z})}{\sqrt{\mathcal{N} v_x}}, \\ u_{\downarrow, \pm}(\mathbf{r}) &= \frac{i t_{\uparrow}^* r_{\downarrow}^* e^{\mp i k_x(-\varepsilon)x} e^{\kappa_{\downarrow z} z} e^{i\phi}}{(r'_{\downarrow} + r'_{\uparrow}) \sqrt{\mathcal{N} v_x}} \end{aligned} \quad (4.35)$$

in the normal region  $-D_N < z < 0$ . Likewise, the corresponding wavefunction components in the superconducting region follow from Eqs. (4.31) upon exchanging electron and hole components, complex conjugating, and sending  $\varepsilon \rightarrow -\varepsilon$ .

To calculate how spin-orbit coupling modifies these scattering states, we now consider a system for which spin-orbit coupling is non-zero in a segment  $0 < x < \delta L$  only. For small enough  $\delta L$ , spin-orbit coupling induces a backscattering amplitude in the scattering state which is linear in  $\delta L$  for small enough  $\delta L$ . Calculating the linear-in- $\delta L$  scattering amplitudes in perturbation theory in  $H_{\text{so}}$  as in Ref. [Duck 11], we find for the electron-to-hole amplitude for electrons incident from the left (*i.e.*, initially moving in the positive  $x$  direction)

$$\rho_{\text{he}} \delta L = -\frac{i}{\hbar} \langle \psi_{h,-} | \delta \hat{\mathcal{H}}_{\text{so}} | \psi_{e,+} \rangle, \quad (4.36)$$

where

$$\delta \hat{\mathcal{H}}_{\text{so}} = \frac{1}{2} \left\{ \begin{pmatrix} H_{\text{so}} & 0 \\ 0 & -H_{\text{so}}^* \end{pmatrix}, \Theta_{\delta L}(x) \right\}, \quad (4.37)$$

with  $\{\cdot, \cdot\}$  the anticommutator and  $\Theta_{\delta L}(x) = 1$  for  $0 < x < \delta L$  and  $\Theta_{\delta L}(x) = 0$  otherwise. This gives

$$\begin{aligned} \rho_{\text{he}} = & - \frac{it_{\uparrow}^2 \hbar k_x k_{\uparrow z} (\Omega_{\text{Sxx}} + i\Omega_{\text{Syy}}) e^{-i\phi} (1 + r_{\downarrow}'^2)}{\mathcal{N} v_x k_{\text{Sz}}^2 (r_{\downarrow}' + r_{\uparrow}')^2} \\ & - \frac{2\hbar k_x (\Omega_{\text{Nxx}} + i\Omega_{\text{Nyy}}) t_{\uparrow} \tau_{\downarrow} e^{-i\phi}}{\mathcal{N} v_x (r_{\uparrow}' + r_{\downarrow}') (\kappa_{\downarrow z}^2 + k_{\uparrow z}^2)} [\kappa_{\downarrow z} (1 + r_{\text{ee}}) - ik_{\uparrow z} (1 - r_{\text{ee}})]. \end{aligned} \quad (4.38)$$

The remaining amplitudes are readily obtained by symmetry arguments. The Andreev reflection amplitude  $\rho_{\text{he}}'$  for incoming electron moving in the negative  $x$  direction is obtained from Eq. (4.38) by sending  $k_x \rightarrow -k_x$ ; The amplitudes for incoming holes are obtained by complex conjugation,  $\rho_{\text{eh}} = \rho_{\text{he}}^*$  and  $\rho_{\text{eh}}' = \rho_{\text{he}}'^*$ . Although the wavefunction penetrates a distance  $\sim \xi$  into the superconductor, the spatial integrals contributing to the matrix element (4.36) have support only within a few wavelengths of the interface [Duck 11]. This is the reason why the first term in Eq. (4.38) does not involve a factor  $\xi$  in the numerator.

The Andreev reflection amplitude  $r_{\text{he}}(L)$  for a segment of length  $L$  can be obtained by solving

$$\frac{dr_{\text{he}}}{dL} = \frac{2i\varepsilon}{\hbar v_x} + \rho_{\text{he}} + \rho_{\text{he}}'^* r_{\text{he}}^2, \quad (4.39)$$

which is obtained by concatenating the scattering matrix of an infinitesimal slice  $0 < x < \delta L$  and a subsequent segment  $\delta L < x < L$  according to Eq. (3.8), and solutions to the differential equation are known [Duck 11]. Integrating Eq. (4.39) gives the non-perturbative amplitudes

$$r_{\text{he}}(L) = \frac{\rho_{\text{he}} \sinh qL}{q \cosh qL - i(\varepsilon/\hbar v_x) \sinh qL} \quad (4.40)$$

and

$$r_{\text{eh}}(L) = \frac{\rho_{\text{eh}}^{\text{eff}} \sinh qL}{\cosh qL - i(\varepsilon/\hbar v_x) \sinh qL}, \quad (4.41)$$

where

$$q = \sqrt{|\rho_{\text{he}}|^2 - (\varepsilon/\hbar v_x)^2}. \quad (4.42)$$

For energies  $|\varepsilon| < \varepsilon_{\text{gap}}$ , with

$$\varepsilon_{\text{gap}} = \hbar v_x |\rho_{\text{he}}| \quad (4.43)$$

one has  $|r_{\text{he}}| \rightarrow 1$  in the limit  $L \rightarrow \infty$ . This is the hallmark of a Majorana bound state [Law 09, Flen 10], with  $\varepsilon_{\text{gap}}$  being the proximity-induced minigap [Duck 11].

With the help of Eq. (4.42) one readily identifies  $l_{\text{maj}} = |\rho_{\text{he}}|^{-1}$  as the localization length of the zero-energy Majorana bound state. The strong renormalization of the velocity  $v_x$  for a transparent interface enters the denominator of Eq. (4.38). However, the fact that in the strong coupling limit  $\Delta \ll \hbar v/D_{\text{N}}$  most of the spectral weight is concentrated in the superconductor also enters into the expression for  $\rho_{\text{he}}$ , through the normalization factor  $\mathcal{N}$ . Interestingly, the superconducting gap  $\Delta$  drops out from the product  $\mathcal{N} v_x$ , causing no additional smallness of the localization length. Nevertheless, the velocity renormalization does affect the product of the minigap and the localization length, in agreement with the analysis of Ref. [Peng 15, Das 15].

#### 4. Renormalization effects in spin-polarized metallic wires proximitized by a superconductor: A scattering approach

---

To assess the dependence on interface transparency, it is instructive to evaluate the expressions for the induced gap and the localization length of the Majorana state for a weakly transmitting barrier. Taking the imaginary part of  $r_{ee}$  from Eq. (4.22), one concludes that the second term in Eq. (4.34) does not contribute to the normalization factor in that limit. Since  $|r'_\downarrow + r'_\uparrow| \simeq 2$  for a weakly transmitting barrier, one finds

$$\mathcal{N} = 2D_N + \frac{|t_\uparrow|^2 \xi_N}{2}. \quad (4.44)$$

To further simplify the expressions for  $\rho_{he}$ , we consider two special cases: (i) Equal Fermi velocities in the normal metal and the superconductor  $k_S = k_\uparrow$ , and  $|w| \gg k_\uparrow$  to ensure a non-transparent interface. (ii)  $k_S \gg k_\uparrow$  with a barrier-free interface  $w = 0$ . Here, the small transparency is the result of a large Fermi velocity mismatch between the superconductor and the normal metal.

In both limits one has  $1 + r_\downarrow^2 = 2$ , although this equality does not hold generally for non-transparent interfaces. Finally, for the factor  $1 + r_{ee}$  we find

$$1 + r_{ee} = t_\uparrow \quad (4.45)$$

in the former limit, and

$$1 + r_{ee} = -\frac{it_\uparrow^2 \kappa_z}{2k_{Sz}} \quad (4.46)$$

in the latter limit (where we assumed that  $\kappa_\downarrow \ll k_S$ ). For the amplitude whose magnitude is equal to the inverse Majorana localization length, we then find

$$\begin{aligned} \rho_{he} &= ie^{-i\phi} m |t_\uparrow|^2 \\ &\times \left( \frac{\pi(\Omega_{Nxx} + i\Omega_{Nyx})}{\pi^2 + \kappa_{\downarrow z}^2 D_N^2} - \frac{\Omega_{Sxx} + i\Omega_{Syx}}{4\pi} \right) \end{aligned} \quad (4.47)$$

for a weakly transmitting interface with  $k_S = k_\uparrow$  and  $|w| \gg k_\uparrow$ , and

$$\begin{aligned} \rho_{he} &= ie^{-i\phi} m |t_\uparrow|^2 \\ &\times \left( \frac{\pi(\Omega_{Nxx} + i\Omega_{Nyx})}{\pi^2 + \kappa_{\downarrow z}^2 D_N^2} - \frac{|t_\uparrow|^4 (\Omega_{Sxx} + i\Omega_{Syx})}{64\pi} \right) \end{aligned} \quad (4.48)$$

in limit of a weakly transmitting interface with  $w = 0$  and  $k_S \gg k_\uparrow$ . Expressions for the induced minigap  $\varepsilon_{\text{gap}} = \hbar v_x |\rho_{he}|$  follow immediately upon multiplication with the renormalized velocity  $v_x$  in Eq. (4.25), restricted to the small-transparency limit.

Figure 4.4 shows the inverse localization length  $|\rho_{he}|$  as a function of barrier transparency for the two limits considered above, as well as the full expression (4.38) (solid line). For the latter, the velocity and the wave numbers are obtained by numerically solving Eq. (4.17). The figures confirm that the low-transparency expressions in Eqs. (4.47) and (4.48) are excellent quantitative approximations for transparencies  $|t_\uparrow|^2 \lesssim 0.5$ . However, for transparencies close to unity, spin-orbit coupling in the superconductor, and  $w = 0$ , we observe a sharp closing of the minigap. This is an interference effect which

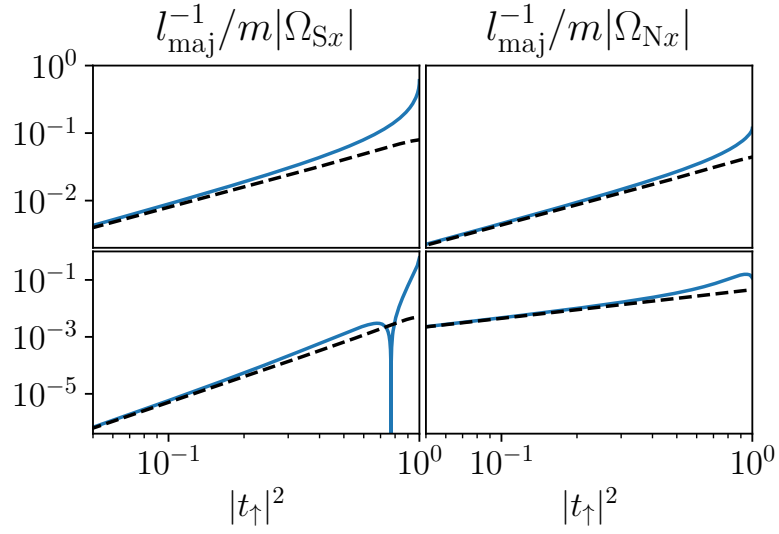


Figure 4.4.: Log-log plot of the inverse localization length  $|\rho_{\text{he}}| = 1/l_{\text{maj}}$  vs. interface transparency  $|t_{\uparrow}|^2$  for an interface with matched Fermi velocities  $k_{\text{S}} = k_{\uparrow}$  (top row) and with zero potential barrier  $w = 0$  (bottom row), with spin-orbit coupling in the superconductor (left column) and in the normal metal (right column). The dashed curves show the weak-transparency results (4.47) and (4.48). The remaining parameters are  $k_{\uparrow}D_{\text{N}} = 1.2\pi$ ,  $(\hbar\pi/D_{\text{N}})^2/2m\Delta = 20$  and  $\kappa_{\downarrow} = 2k_{\uparrow}$ . We defined  $\Omega_{\text{S}x}^2 \equiv \Omega_{\text{S}xx}^2 + \Omega_{\text{S}yx}^2$  and  $\Omega_{\text{N}x}^2 \equiv \Omega_{\text{N}xx}^2 + \Omega_{\text{N}yx}^2$ .

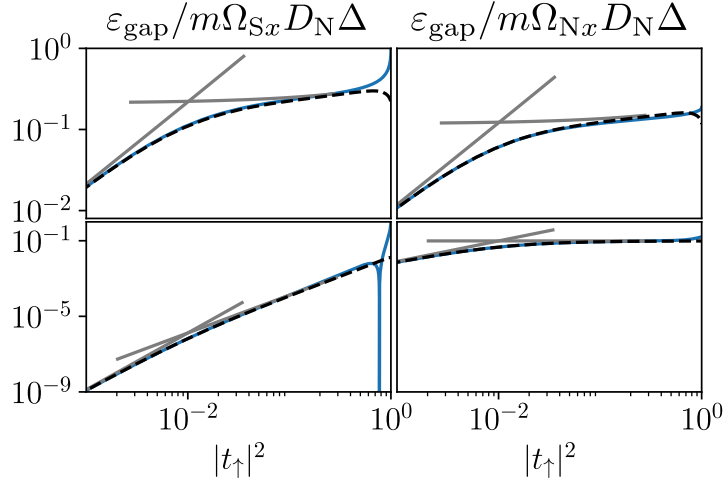


Figure 4.5.: Log-log plot of the minigap versus transparency for the same conditions as in Fig. 4.4. The grey curves show the power laws corresponding to the weak-coupling limit  $|t_{\uparrow}|^2 \ll D_N/\xi_N$  and the strong-coupling limit (at weak transparency)  $D_N/\xi_N \ll |t_{\uparrow}|^2 \ll 1$ . The dashed curve is obtained using the weak-transparency results (4.47) and (4.48) for the inverse localization length  $\rho_{\text{he}}$ . The parameter values are  $k_{\uparrow}D_N = 1.2\pi$ ,  $(\hbar\pi/D_N)^2/2m\Delta = 200\pi$  and  $\kappa_{\downarrow} = 2k_{\uparrow}$ .

can be traced back to the factor  $1 + r_{\downarrow}^2 = 2e^{i\varphi_{\downarrow}} \cos \varphi_{\downarrow}$  in Eq. (4.38). For  $w = 0$  and with  $\kappa_{\downarrow} > k_{\uparrow}$  the minority reflection phase  $\varphi_{\downarrow}$  passes through  $\pi/2$  close to unit transparency, see Eq. (4.12). A similar effect appears upon approaching perfect transparency by varying  $w$  at  $k_{\uparrow} = k_S$  for negative  $w$  (data not shown).

Figure 4.5 shows the induced minigap  $\epsilon_{\text{gap}}$  as a function of barrier transparency. Here the transition between the strong-coupling and weak-coupling limits at  $|t_{\uparrow}|^2 \sim D_N/\xi_N$  can be clearly seen. The weak-coupling limit agrees with the theory of Ref. [Duck 11]; the velocity renormalization appears in the strong-coupling limit  $|t_{\uparrow}|^2 \gtrsim D_N/\xi_N$ .

### 4.3. Cylindrical geometry

The planar model discussed in Sec. 4.2 accounts only for a small subset of realizable materials. This motivates us to investigate a three dimensional analogue thereof. We consider a spin-polarized normal metal wire with a cylindrical cross-section surrounded by an  $s$ -wave superconductor with spin-orbit coupling in either of the two materials. The cross section is shown in Fig. 4.6. The wire has a radius  $R$ , which replaces the thickness  $D_N$  used in Sec. 4.2. The main differences to the planar model are a change in the basis of the transverse components, from plane waves to Bessel functions, and the addition of an angular momentum quantum number. We neglect the orbital contribution of the magnetic field and take only the Zeeman field into account.

We consider the parameter regime of sufficiently narrow wires such that a single trans-

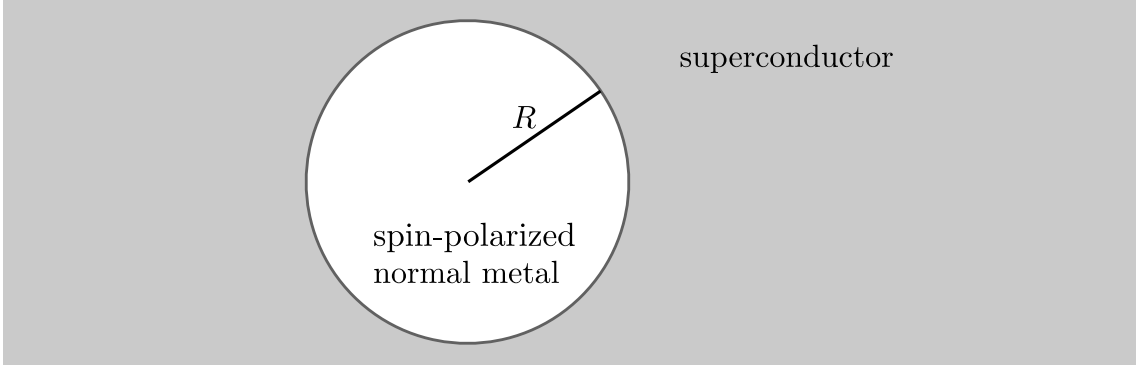


Figure 4.6.: Cross section of the cylindrical-wire model. A spin-polarized normal metal wire of radius  $R$  is embedded in an  $s$ -wave superconductor.

verse mode, the one with zero angular-momentum, is present inside the wire. We are able to show that the renormalization of the velocity and minigap are qualitatively the same as in the planar geometry, and consequently the Majorana localization length is not renormalized.

The outline of our approach is similar to the planar setup. After defining the cylindrical model, we first define the transmission and reflection amplitudes at a normal-metal–normal-metal interface. Next, we turn on superconductivity and follow the lines of Sec. 4.2.1 in order to obtain the renormalized velocity. Building on these results, we then derive the Majorana decay length and the minigap in the presence of the spin-orbit coupling.

The cylindrical-wire model is described by the same Hamiltonian as in Eq. (4.2), with three changes. First, we generalize to cylindrical coordinates  $(r, \varphi, x)$ , with  $x$  parallel to the wire. The explicit dependence on  $z$  is changed by replacing  $z \rightarrow r - R$ . Second, we set  $V_{\text{conf}}(r) = 0$  for all  $r$ , as the cylindrical normal wire has a boundary with the superconductor only, while for the planar setup a termination at  $z = -D_N$  was necessary. Third, we take into account the cylindrical geometry in the spin-orbit coupling tensor, such that the components along the unit vectors  $\hat{\mathbf{e}}_r$ ,  $\hat{\mathbf{e}}_\varphi$  and  $\hat{\mathbf{e}}_x$  are constant. To this end, we redefine

$$\Omega_{Xj} = \Omega_{Xjr}\hat{\mathbf{e}}_r + \Omega_{Xj\varphi}\hat{\mathbf{e}}_\varphi + \Omega_{Xjx}\hat{\mathbf{e}}_x \quad (4.49)$$

where  $X = S, N$ .

### 4.3.1. Cylindrical normal-normal metal interface

We now derive the scattering amplitudes at the interface for  $\Delta = 0$  and in the absence of spin-orbit coupling. We define the propagating modes

$$\Psi_{k_x, m}(\mathbf{r}, \varepsilon) = e^{im\varphi + ik_x x} \psi_{k_x, m}(r, \varepsilon) \quad (4.50)$$

Here, we introduced the integer angular momentum quantum number  $m$  and the longitudinal momentum  $k_x$ . In order to distinguish the quantum number  $m$  from the mass of

4. Renormalization effects in spin-polarized metallic wires proximitized by a superconductor: A scattering approach

---

the electrons, we rename the latter to  $m_e$  for the remainder of this section. The radial component, normalized to unit flux, reads

$$\begin{aligned} \psi_{k_x, m}(r, \varepsilon) = & \sqrt{\frac{\pi m_e}{2\hbar}} \times \begin{pmatrix} c_{e, m, \uparrow} H_m^{(1)}(k_{\uparrow r}(\varepsilon)r) + c'_{e, m, \uparrow} H_m^{(2)}(k_{\uparrow r}(\varepsilon)r) \\ 0 \\ c_{h, m, \uparrow} H_m^{(2)}(k_{\uparrow r}(-\varepsilon)r) + c'_{h, m, \uparrow} H_m^{(1)}(k_{\uparrow r}(-\varepsilon)r) \\ 0 \end{pmatrix} \\ & + \sqrt{\frac{2\pi m_e}{\hbar}} \begin{pmatrix} 0 \\ c_{e, m, \downarrow} I_m(\kappa_{\downarrow r}(\varepsilon)r) \\ 0 \\ c_{h, m, \downarrow} I_m(\kappa_{\downarrow r}(-\varepsilon)r) \end{pmatrix} \end{aligned} \quad (4.51)$$

for  $r < R$  and

$$\psi_{k_x, m}(r) = \sqrt{\frac{\pi m_e}{2\hbar}} \begin{pmatrix} d_{e, m, \uparrow} H_m^{(2)}(k_{S_r} r) + d'_{e, m, \uparrow} H_m^{(1)}(k_{S_r} r) \\ d_{e, m, \downarrow} H_m^{(2)}(k_{S_r} r) + d'_{e, m, \downarrow} H_m^{(1)}(k_{S_r} r) \\ d_{h, m, \uparrow} H_m^{(1)}(k_{S_r} r) + d'_{h, m, \uparrow} H_m^{(2)}(k_{S_r} r) \\ d_{h, m, \downarrow} H_m^{(1)}(k_{S_r} r) + d'_{h, m, \downarrow} H_m^{(2)}(k_{S_r} r) \end{pmatrix} \quad (4.52)$$

for  $r > R$ . Here,  $H_m^{(1,2)}$  are the Hankel functions of first and second kind and  $I_m$  is the modified Bessel function of the first kind. The wave and decay numbers are

$$k_{\uparrow r}(\varepsilon) = \sqrt{k_{\uparrow}^2 - k_x^2 + 2m_e\varepsilon/\hbar^2}, \quad (4.53)$$

$$\kappa_{\downarrow r}(\varepsilon) = \sqrt{\kappa_{\downarrow}^2 + k_x^2 - 2m_e\varepsilon/\hbar^2}, \quad (4.54)$$

$$k_{S_r} = \sqrt{k_S^2 - k_x^2}. \quad (4.55)$$

We neglected the  $\varepsilon$ -dependence in  $k_{S_r}$ , which assumes  $\hbar^2 k_{S_r}^2/m_e \ll |\varepsilon|$ . As we are interested in the sub-gap spectrum, this corresponds to Andreev approximation  $\hbar^2 k_{S_r}^2/m_e \ll \Delta$ .

The  $c$ -coefficients are constrained by the requirement that the wavefunction has to be well behaved at the origin. This constraint is satisfied for  $c'_{e, m, \uparrow} = c_{e, m, \uparrow}$  and  $c'_{h, m, \uparrow} = c_{h, m, \uparrow}$ , as the Hankel-functions add up to the Bessel functions of the first kind  $J_m(z) = [H_m^{(1)}(z) + H_m^{(2)}(z)]/2$ , which is well behaved at the origin. For the minority modes,  $I_m$  is trivially well behaved at the origin.

The requirement of a continuous wavefunction across the interface and the relation

$$\psi'_{k_x, m}(R + \delta, \varepsilon) = \psi'_{k_x, m}(R - \delta, \varepsilon) + 2\omega\psi_{k_x, m}(R, \varepsilon), \quad (4.56)$$

with  $\delta \rightarrow 0$ , further constrain the  $c$ -coefficients. Solving the matching conditions relates

the in- and out-going modes by

$$\begin{pmatrix} d'_{e,m,\uparrow} \\ c'_{e,m,\uparrow} \\ d'_{h,m,\uparrow} \\ c'_{h,m,\uparrow} \end{pmatrix} = \begin{pmatrix} t_{\uparrow m}(\varepsilon) & r'_{\uparrow m}(\varepsilon) & 0 & 0 \\ r_{\uparrow m}(\varepsilon) & t_{\uparrow m}(\varepsilon) & 0 & 0 \\ 0 & 0 & t_{\uparrow m}^*(-\varepsilon) & r'_{\uparrow m}{}^*(-\varepsilon) \\ 0 & 0 & r_{\uparrow m}^*(-\varepsilon) & t_{\uparrow m}^*(-\varepsilon) \end{pmatrix} \begin{pmatrix} c_{e,m,\uparrow} \\ d_{e,m,\uparrow} \\ c_{h,m,\uparrow} \\ d_{h,m,\uparrow} \end{pmatrix}, \quad (4.57)$$

$$\begin{pmatrix} d'_{e,m,\downarrow} \\ c_{e,m,\downarrow} \\ d'_{h,m,\downarrow} \\ c_{h,m,\downarrow} \end{pmatrix} = \begin{pmatrix} r'_{\downarrow m}(\varepsilon) & 0 \\ t_{\downarrow m}(\varepsilon) & 0 \\ 0 & r'_{\downarrow m}{}^*(-\varepsilon) \\ 0 & t_{\downarrow m}^*(-\varepsilon) \end{pmatrix} \begin{pmatrix} d_{e,m,\downarrow} \\ d_{h,m,\downarrow} \end{pmatrix}. \quad (4.58)$$

Here, we dropped the dependence on  $k_x$  for the sake of compactness. For each  $m$ , Eqs. (4.57) and (4.58) are identical to the ones for a planar setup [Kupf 11], while the parametrization of the amplitudes differs,

$$t_{\uparrow m}(k_x, \varepsilon) = \frac{4i/\pi R}{k_{Sr} H_{m-1}^{(1)}(k_{Sr} R) H_m^{(2)}(k_{\uparrow r} R) - H_m^{(1)}(k_{Sr} R) [k_{\uparrow r} H_{m-1}^{(2)}(k_{\uparrow r} R) + 2\omega H_m^{(2)}(k_{\uparrow r} R)]}, \quad (4.59)$$

$$r_{\uparrow m}(k_x, \varepsilon) = \frac{-H_m^{(1)}(k_{\uparrow r} R) + t_{\uparrow m} H_m^{(1)}(k_{Sr} R)}{H_m^{(2)}(k_{\uparrow r} R)}, \quad (4.60)$$

$$r'_{\uparrow m}(k_x, \varepsilon) = \frac{-H_m^{(2)}(k_{Sr} R) + t_{\uparrow m} H_m^{(2)}(k_{\uparrow r} R)}{H_m^{(1)}(k_{Sr} R)}, \quad (4.61)$$

$$t_{\downarrow m}(k_x, \varepsilon) = \frac{2i/\pi R}{k_{Sr} H_{m-1}^{(1)}(k_{Sr} R) I_m(\kappa_{\downarrow r} R) - H_m^{(1)}(k_{Sr} R) [\kappa_{\downarrow r} I_{m-1}(\kappa_{\downarrow r} R) + 2\omega I_m(\kappa_{\downarrow r} R)]}, \quad (4.62)$$

$$r'_{\downarrow m}(k_x, \varepsilon) = e^{i\varphi_{\downarrow m}(k_x, \varepsilon)} = \frac{-H_m^{(2)}(k_{Sr} R) + 2t_{\downarrow m} I_m(\kappa_{\downarrow r} R)}{H_m^{(1)}(k_{Sr} R)}. \quad (4.63)$$

Here we dropped the dependencies on  $(k_x, +\varepsilon)$  on the right-hand side.

Next, we consider the limiting cases of the Bessel functions for large and small arguments. These are useful for the subsequent discussion. First, in the limit where  $m$  is small compared to the arguments of the Bessel functions, the amplitudes are related to the ones in the planar model in Eqs. (4.8) to (4.10), (4.12) and (4.30) by

$$t_{\uparrow m}(k_x, 0) = e^{i(k_{\uparrow r} - k_{Sr})R} t_{\uparrow}(k_x)|_{z \rightarrow r}, \quad (4.64)$$

$$r_{\uparrow m}(k_x, 0) = -i(-1)^m e^{2ik_{\uparrow r}R} r_{\uparrow}(k_x)|_{z \rightarrow r}, \quad (4.65)$$

$$r'_{\uparrow m}(k_x, 0) = i(-1)^m e^{-2ik_{Sr}R} r'_{\uparrow}(k_x)|_{z \rightarrow r}, \quad (4.66)$$

$$r'_{\downarrow m}(k_x, 0) = i(-1)^m e^{-2ik_{Sr}R} r'_{\downarrow}(k_x)|_{z \rightarrow r}, \quad (4.67)$$

$$t_{\downarrow m}(k_x, \varepsilon) = e^{(2m+1)\pi/4 - \kappa_{\downarrow r}R - ik_{Sr}R} \sqrt{\frac{\kappa_{\downarrow r}}{k_{\uparrow r}}} \tau_{\downarrow}(k_x) \Big|_{z \rightarrow r}. \quad (4.68)$$

#### 4. Renormalization effects in spin-polarized metallic wires proximitized by a superconductor: A scattering approach

---

Next, we consider the cases of large and intermediate  $|m|$ , for the relevant regime  $k_{\uparrow r} \sim \kappa_{\downarrow r} \lesssim k_{Sr}$ . In the large  $|m|$  limit,  $k_{Sr}R \ll |m|$ ,  $k_{\uparrow r}R \ll |m|$ , the radial modes have a vanishing overlap with the wire and  $r'_{\uparrow m} = r'_{\downarrow m} = r_{\uparrow m} = 1$ ,  $t_{\uparrow m} = 0$ . Hence, these modes have a vanishing overlap with the wire. For intermediate angular momentum numbers,  $k_{\uparrow r}R \ll m \ll k_{Sr}R$ , we get  $r_{\uparrow m} = 1$  and  $t_{\uparrow m} = 0$ . Consequently the amplitude inside the wire vanishes. The remaining reflection amplitudes  $r'_{\uparrow m}$  and  $r'_{\downarrow m}$  are of magnitude one.

In the limit of an ideal interface,  $w = 0$  and  $k_{\uparrow} = k_S$  the amplitudes for the majority carriers reduce to  $t_{\uparrow m} = 1$  and  $r_{\uparrow m} = r'_{\uparrow m} = 0$ , which can be verified by using the Wronskian of the Hankel functions and the unitarity of the scattering matrix [Olve 10].

#### 4.3.2. Velocity renormalization

Next, we include a finite pairing potential  $\Delta > 0$ . As described in Sec. 4.2.1, this confines excitations with energies  $\varepsilon < \Delta$  to the normal region,  $r < R$ , with evanescent components in the superconducting region that decay at a length scale of order of the coherence length  $\xi_\varepsilon$ . The additional weight in the superconductor, as well as the change of the matching conditions at the boundary lead to renormalization of the wire dispersion.

We continue to derive the renormalization of the velocity along the lines of Sec. 4.2.1. The majority wavefunctions for  $r < R$  read

$$\psi_{k_x, m}(r, \varepsilon) = \begin{pmatrix} u_{\uparrow, k_x, m}(r, \varepsilon) \\ 0 \\ 0 \\ v_{\downarrow, k_x, m}(r, \varepsilon) \end{pmatrix}, \quad (4.69)$$

$$u_{\uparrow, k_x, m}(r, \varepsilon) = \sqrt{\frac{\pi m_e}{2\hbar}} \left[ H_m^{(1)}(k_{\uparrow r}(\varepsilon)r) + r_{ee, m}(k_x, \varepsilon) H_m^{(2)}(k_{\uparrow r}(\varepsilon)r) \right], \quad (4.70)$$

$$v_{\downarrow, k_x, m}(r, \varepsilon) = \sqrt{\frac{2\pi m_e}{\hbar}} c_{h, m, \downarrow} I_m(\kappa_{\downarrow r}(-\varepsilon)r). \quad (4.71)$$

The amplitude  $r_{ee, m}$  is derived by applying wavefunction matching at  $r = R$  and by requiring the modes to decay in the limit  $r \rightarrow \infty$ . The latter condition yields the wavefunction

$$\psi_{k_x, m}(r, \varepsilon) = \sqrt{\frac{\pi m_e}{2\hbar}} \left[ \frac{H_m^{(1)}\left(k_{Sr}r + i\frac{r}{\xi_\varepsilon}\right)}{A_m^{(1)}} \begin{pmatrix} d'_\uparrow \\ 0 \\ 0 \\ d'_\uparrow e^{-i\eta - i\phi} \end{pmatrix} + \frac{H_m^{(2)}\left(k_{Sr}r - i\frac{r}{\xi_\varepsilon}\right)}{A_m^{(2)}} \begin{pmatrix} d_\uparrow \\ 0 \\ 0 \\ d_\uparrow e^{i\eta - i\phi} \end{pmatrix} \right], \quad (4.72)$$

for  $r > R$ , where the factors

$$A_m^{(1/2)} = \frac{H_m^{(1/2)}\left(k_{Sr}R \pm i\frac{R}{\xi_\varepsilon}\right)}{H_m^{(1/2)}(k_{Sr}R)} \quad (4.73)$$

ensure continuity at  $r = R$ . We dropped the  $\varepsilon$  and  $k_x$  dependencies for the sake of compactness. Within Andreev approximation,  $\hbar^2 k_{\text{Sr}}^2 / 2m_e \ll \Delta$ , the interface can be treated as an interface between two normal metals. Thus, the  $c$  and  $d$  coefficients are related by Eqs. (4.57) and (4.58). We choose  $c_{e,m,\uparrow} = 1$ , and obtain

$$r_{ee,m}(k_x, \varepsilon) = r_{\uparrow m}(k_x, \varepsilon) + \frac{t_{\uparrow m}(k_x, \varepsilon)^2}{r'_{\downarrow m}(k_x, -\varepsilon)e^{2i\eta(\varepsilon)} - r'_{\uparrow m}(k_x, \varepsilon)}, \quad (4.74)$$

$$d_{\uparrow}(k_x, \varepsilon) = \frac{t_{\uparrow m}(k_x, \varepsilon)}{r'_{\downarrow m}(k_x, -\varepsilon)e^{2i\eta(\varepsilon)} - r'_{\uparrow m}(k_x, \varepsilon)}, \quad (4.75)$$

$$d'_{\uparrow}(k_x, \varepsilon) = r'_{\downarrow m}(k_x, -\varepsilon)e^{2i\eta(\varepsilon)}d_{\uparrow}(k_x, \varepsilon), \quad (4.76)$$

$$c_{h,m,\downarrow}(k_x, \varepsilon) = t_{\downarrow m}^*(k_x, -\varepsilon)e^{-i\eta(\varepsilon)-i\phi}d'_{\uparrow}(k_x, \varepsilon). \quad (4.77)$$

Equations (4.74) to (4.77) are identical to the ones in a planar setup at  $\varepsilon = 0$  [Kupf 11], while the parametrization of the amplitudes is different.

The requirement of a well-behaved wavefunction at the origin gives

$$1 = r_{ee,m}(k_x, \varepsilon_m). \quad (4.78)$$

Solving this equation yields the dispersion  $\varepsilon_m(k_x)$  and the renormalized velocity  $v_{x,m}(\varepsilon) = |d\varepsilon_m/dk_x|/\hbar$ . In the following, we provide solutions to Eq. (4.78) in the limiting cases of an ideal and a low transparency interface.

For an ideal interface,  $w = 0$  and  $k_{\text{S}} = k_{\uparrow}$ , Eq. (4.78) reduces to

$$2\eta(\varepsilon_m) + \varphi_{\downarrow m}(k_x, \varepsilon_m) = 2\pi n. \quad (4.79)$$

Within Andreev approximation for the normal region,  $\hbar^2 k_{\uparrow r}^2 / 2m_e \Delta \ll 1$  and  $\hbar^2 \kappa_{\downarrow r}^2 / 2m_e \Delta \ll 1$ , the energy dependence in  $\varphi_{\downarrow m}$  can be neglected, and we obtain

$$\varepsilon_m(k_x) = \pm \Delta \cos \varphi_{\downarrow m}(k_x). \quad (4.80)$$

For  $m \gg k_{\uparrow r} R$ , the phase  $\varphi_{\downarrow m}$  vanishes and  $\varepsilon_m = \pm \Delta$ . Hence, the large  $m$  modes are gapped out. For  $k_{\uparrow r} R \gtrsim m$ , we can use the approximation (4.67) to obtain

$$2k_{\uparrow r} R = 2\eta(\varepsilon_m) + \varphi_{\downarrow}(k_x) + (4n + 2m + 1)\pi/2, \quad (4.81)$$

where  $\varphi_{\downarrow}(k_x)$  is defined in Eq. (4.12). Solving for  $\varepsilon_m$ , we get

$$\varepsilon_m(k_x) = \pm \Delta \cos \left[ k_{\uparrow r} R - \frac{\varphi_{\downarrow}(k_x)}{2} - (2m + 1)\frac{\pi}{4} \right], \quad (4.82)$$

The velocity is obtained by taking the derivative,

$$v_{x,m}(k_x) = \sqrt{\Delta^2 - \varepsilon_m^2} \frac{k_x R}{\hbar k_{\uparrow r}} \left| 1 - \frac{1}{\kappa_{\downarrow r} R} \right|, \quad (4.83)$$

which is identical to the one for the planar model upon replacing  $r$  by  $z$  and  $R$  by  $D_{\text{N}}$ . The analytical predictions in Eqs. (4.82) and (4.83) are compared to a direct numerical solution of Eq. (4.78) in Figs. 4.7 and 4.8. Both limiting cases show good agreement.

#### 4. Renormalization effects in spin-polarized metallic wires proximitized by a superconductor: A scattering approach

---

Next, we consider the limit of an opaque interface,  $w, k_{Sr} \gg k_{\uparrow r}, \kappa_{\downarrow r}$ . For  $m \gg k_{Sr}R$  the overlap with the wire vanishes and all modes are gapped out,  $\varepsilon = \pm\Delta$ . For  $m \lesssim k_{Sr}R$ , we obtain

$$r_{ee,m}(k_x, \varepsilon) = -\frac{H_m^{(1)}(k_{\uparrow r}R) |H_m^{(1)}(k_{\uparrow r}R)|^2 \pi R \Delta (k_{Sr}^2 + 4w^2) + 2ik_{\uparrow r}(k_{Sr}\varepsilon/\Delta + 2w)}{H_m^{(2)}(k_{\uparrow r}R) |H_m^{(1)}(k_{\uparrow r}R)|^2 \pi R \Delta (k_{Sr}^2 + 4w^2) - 2ik_{\uparrow r}(k_{Sr}\varepsilon/\Delta + 2w)}. \quad (4.84)$$

Equation (4.78) enforces  $r_{ee,m} = 1$  and to zeroth order in  $k_{\uparrow r}/w$  and  $k_{\uparrow r}/k_{Sr}$  we get  $H_m^{(1)}(k_{\uparrow r}R) + H_m^{(2)}(k_{\uparrow r}R) = 0$ . The solutions of this equation correspond to the zeros of the  $m$ -th order Bessel function of the first kind. Since  $k_{\uparrow r} \leq k_{\uparrow}$  within our semiclassical approximation, no solutions are available for  $m \gg k_{\uparrow}R$ , hence we can employ the small  $m$  approximation. To leading order in  $k_{\uparrow r}/w$  and  $k_{\uparrow r}/k_{Sr}$ , Eq. (4.84) reduces to

$$r_{ee,m}(k_x, \varepsilon) \approx -e^{2ik_{\uparrow r}R - i(2m+1)\frac{\pi}{2}} \frac{k_{Sr}^2 + 4w^2 + ik_{\uparrow r}(k_{Sr}\varepsilon/\Delta + 2w)}{k_{Sr}^2 + 4w^2 - ik_{\uparrow r}(k_{Sr}\varepsilon/\Delta + 2w)}. \quad (4.85)$$

In the following, we will focus on the regime where  $k_{\uparrow r}R$  is of order one and sufficiently small such that only a single mode has significant overlap into the spin-polarized normal metal wire. This mode has  $m = 0$ , and Eq. (4.85) yields

$$k_{\uparrow r} = \frac{3\pi}{4R} \left[ 1 - \frac{k_{Sr}\varepsilon_0/\Delta + 2w}{R(k_{Sr}^2 + 4w^2)} \right], \quad (4.86)$$

and the dispersion

$$\varepsilon_0(k_x) = \frac{\hbar^2}{2m_e} \left[ k_x^2 - k_{\uparrow}^2 + \frac{9\pi^2}{16R^2} \left( 1 - 2\frac{k_{Sr}\varepsilon_0/\Delta + 2w}{R(k_{Sr}^2 + 4w^2)} \right) \right]. \quad (4.87)$$

The  $\varepsilon_0$ -dependence on the right hand side can be neglected. The longitudinal velocity is

$$v_{x,m} = \frac{v_r \sin \theta_r}{1 + \xi_{N0} |t_{\uparrow 0}|^2 / 4R}, \quad (4.88)$$

where  $v_r = \hbar k_{\uparrow} / m_e$ ,  $\sin \theta_r = k_x / k_{\uparrow}$  and  $\xi_{N0} = \hbar^2 k_{\uparrow r} / m_e \Delta$ .

The renormalization of the dispersion that is present in Eqs. (4.87) and (4.88) is the same as the one for the planar setup, see Eqs. (4.24) and (4.25), up to the change  $D_N \rightarrow R$ ,  $z \rightarrow r$  and the factor 9/16 in Eq. (4.87), which originates in the basis change from plane waves for two dimensions to Bessel functions in three dimensions. The approximations in Eqs. (4.87) and (4.88) are shown as the dashed line in Figs. 4.7 and 4.8. They show good agreement for small transparencies. The renormalized velocity (4.88) is essentially the same as for the planar geometry, see Eq. (4.25).

### 4.3.3. Minigap and Majorana localization length

Spin-orbit coupling is expected to have the same effects as in the planar-model, making Andreev reflection between majority spin electrons and majority spin holes possible, opening a minigap  $\varepsilon_{\text{gap}}$  and allowing Majorana bound states to form at the end of the cylindrical wire.

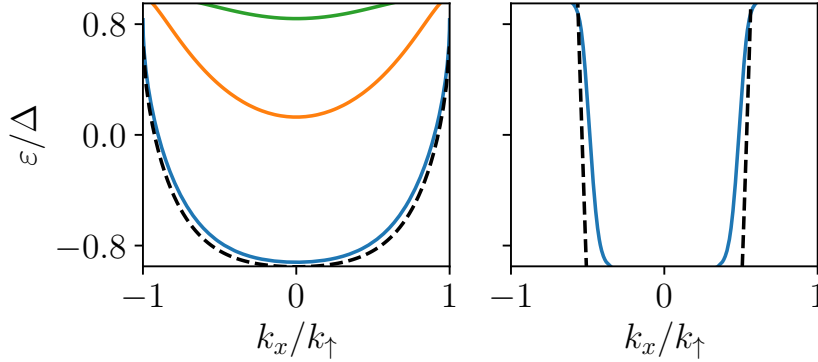


Figure 4.7.: Dispersion of the cylindrical setup at different interface transparencies. The figure shows only half of the BdG spectrum, the other half is obtained by taking  $\varepsilon \rightarrow -\varepsilon$ . We choose  $k_S = k_\uparrow$  and  $w = 0$  on the left, which yields  $t_{\uparrow m} = 1$ , and  $w/k_\uparrow = 2$  with  $k_S = k_\uparrow$  on the right, corresponding to  $|t_{\uparrow 0}|^2 = 0.2$  for perpendicular incidence. The solid lines show the numerical solution of Eq. (4.78), with angular momentum numbers  $m = 0$  (blue),  $m = \pm 1$  (orange) and  $m = \pm 2$  (green). In the right plot, we find in-gap solutions for  $m = 0$  only. The dashed lines shows the predictions from Eq. (4.82)(left) and (4.87)(right). The remaining parameters are  $k_\uparrow R = 0.8\pi$ ,  $\kappa_\downarrow/k_\uparrow = 2$  and  $(\hbar\pi/R)^2/2m_e\Delta = 50$ .

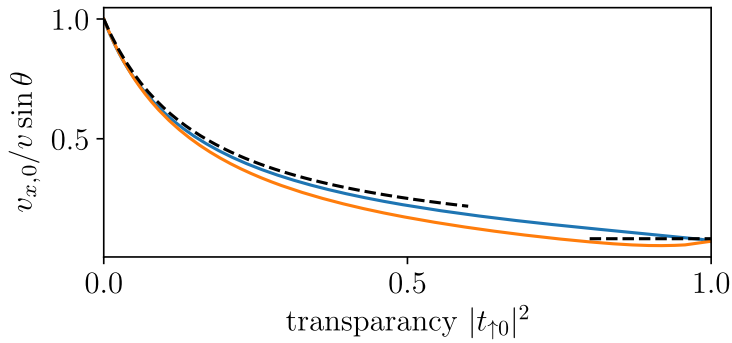


Figure 4.8.: Velocity renormalization as a function of transparency on a semi-logarithmic scale. For the blue (upper) line, we tune the transparency by varying  $w$  while keeping  $k_\uparrow = k_S$  fixed. For the orange (lower) line, we vary  $k_S/k_\uparrow \geq 1$  with  $w = 0$  fixed. The dashed lines show the predictions for  $|t_{\uparrow 0}|^2 \ll 1$  and for  $|t_{\uparrow 0}|^2 = 1$ . The remaining parameters are the same as in Fig. 4.7.

#### 4. Renormalization effects in spin-polarized metallic wires proximitized by a superconductor: A scattering approach

---

We assume spin-orbit coupling to be weak, such that we can treat its effects within first order perturbation theory and we neglect finite-energy corrections of order  $\varepsilon/\Delta$ . Furthermore, we restrict ourselves to the  $m = 0$  mode.

We define the electron like wave functions  $|\psi_{e\pm}\rangle$ , travelling into the positive (+) or negative (-)  $x$  direction, by

$$\psi_{e\pm}(\mathbf{r}, \varepsilon) = \frac{\sqrt{v_{\uparrow r}} e^{ik_x(\varepsilon)x}}{\sqrt{2\pi v_{x,m} \mathcal{N}_0}} \psi_{\pm k_x(0),0}(r, \varepsilon) \quad (4.89)$$

with  $\psi_{\pm k_x(\varepsilon),0}(r, \varepsilon)$  defined in Eqs. (4.69) and (4.72) and

$$k_x(\varepsilon) = \sqrt{k_{\uparrow}^2 - k_{\downarrow}^2 + \frac{\varepsilon}{\hbar v_{x,m}}}. \quad (4.90)$$

The normalization constant is obtained by normalizing  $\psi_{e\pm}$  to unit flux along the wire and one obtains

$$\mathcal{N}_0 = 2R + 2\xi_N \frac{|t_{\uparrow 0}|^2}{|r'_{\downarrow 0} + r'_{\uparrow 0}|^2}. \quad (4.91)$$

Here, we define  $\xi_N = \hbar^2 k_{\uparrow r} / m_e \Delta$ , neglect the minority spin contribution and expand the Bessel functions in terms of plane waves. The renormalization factor in Eq. (4.91) is similar to the one in the planar setup, see Eq. (4.44).

The hole-like wavefunctions  $\psi_{h\pm}$ , travelling into positive (+) or negative (-)  $x$ -direction, are obtained by applying particle-hole symmetry

$$\psi_{h\pm}(\mathbf{r}, \varepsilon) = \tau_x [\psi_{e\pm}(\mathbf{r}, -\varepsilon)]^*. \quad (4.92)$$

In order to study how spin-orbit coupling changes these states, we consider a segment  $0 < x < \delta L$ , in which spin-orbit coupling is turned on while it is zero elsewhere. For sufficiently small  $\delta L$ , the reflection amplitude becomes linear in  $\delta L$ . Along the lines of Sec. 4.2.2, we define

$$\rho_{\text{he,c}} \delta L = -\frac{i}{\hbar} \langle \psi_{h,-} | \delta \hat{\mathcal{H}}_{\text{so}} | \psi_{e,+} \rangle. \quad (4.93)$$

and for  $\kappa_{\downarrow r} R \gtrsim 1$ , we obtain

$$\begin{aligned} \rho_{\text{he,c}} = & \frac{-k_{\uparrow r} \hbar k_x (\Omega_{Sxx} + i\Omega_{Syy}) e^{-i\phi + 2ik_{\uparrow r} R} t_{\uparrow}^2 (1 + r_{\downarrow}'^2)}{v_{x,m} \mathcal{N}_0 k_{S_r}^2 (r_{\downarrow}' + r_{\uparrow}')^2} \\ & - \frac{2\hbar k_x (\Omega_{Nxx} + i\Omega_{Nyy}) e^{-i\phi} \tau_{\downarrow} t_{\uparrow}}{v_{x,m} \mathcal{N}_0 (k_{\uparrow r}^2 + \kappa_{\downarrow r}^2) (r_{\downarrow}' + r_{\uparrow}')^2} \left[ \kappa_{\downarrow r} \left( 1 - i e^{2ik_{\uparrow r} R} \right) + ik_{\uparrow r} \left( 1 + i e^{2ik_{\uparrow r} R} \right) \right], \end{aligned} \quad (4.94)$$

where  $t_{\uparrow}$ ,  $\tau_{\downarrow}$ ,  $r_{\uparrow}'$  and  $r_{\downarrow}'$  are the interface amplitudes defined in the planar setup.

The remaining amplitudes for reflection from the right, as well as the reflection amplitudes from majority holes into majority electrons are obtained by the same symmetry arguments as the ones discussed below Eq. (4.38). The reflection amplitudes for a segment of length  $L$  is the same as in Eq. (4.40) upon replacing  $\rho_{\text{he}}$  by  $\rho_{\text{he,c}}$  and  $v_x$  by  $v_{x,0}$ . This allows us to define the minigap

$$\varepsilon_{0,c} = \hbar v_{x,m} |\rho_{\text{he,c}}|, \quad (4.95)$$

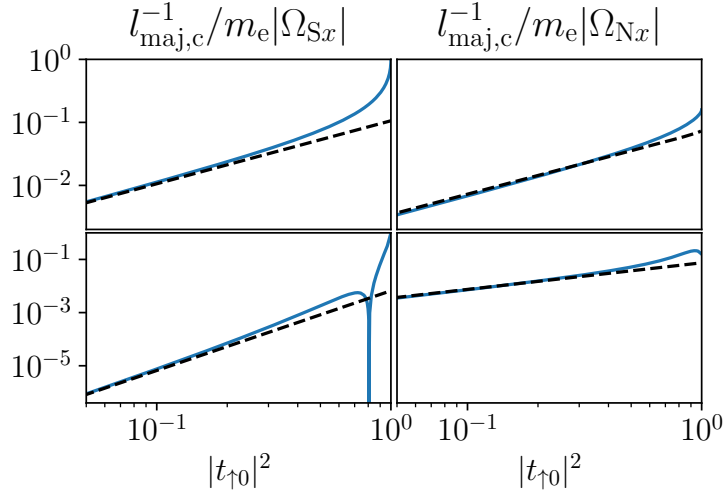


Figure 4.9.: Log-log plot of the Majorana decay strength as a function of transparency for the cylindrical setup. We choose matched Fermi velocities (top row) and zero potential barrier  $w = 0$  (bottom row), with spin-orbit coupling in the superconductor (left column) and in the normal metal (right column). The dashed curves show the weak transparency results, the solid lines are obtained by numerically solving Eq. (4.78) and using Eq. (4.94). The remaining parameters are  $k_{\uparrow r}R = 0.8\pi$ ,  $\kappa_{\downarrow}/k_{\uparrow} = 2$  and  $(\hbar\pi/R)^2/2m_e\Delta = 50$ .

and the localization length

$$l_{\text{maj,c}} = |\rho_{\text{he,c}}|^{-1}. \quad (4.96)$$

Equation (4.94) is almost identical to  $\rho_{\text{he}}$  in Eq. (4.38). Indeed, in the single mode limit and for  $k_{\uparrow r}R \gtrsim 1$  we have

$$1 = r_{\text{ee},0} = -ie^{2ik_{\uparrow r}R}r_{\text{ee}}, \quad (4.97)$$

with  $r_{\text{ee}}$  defined in Eq. (4.15), allowing us to identify  $\rho_{\text{he}} = \rho_{\text{he,c}}ie^{-2ik_{\uparrow r}R}$ , upon replacing the labels  $r$  by  $z$  and  $R$  by  $D_{\text{N}}$ . The asymptotic expansions for  $\rho_{\text{he}}$  in the limit  $|t_{\uparrow}|^2 \ll 1$  are then obtained by replacing the factors  $\pi$  in Eqs. (4.47) and (4.48) by factors of  $3\pi/4$ , which originates in the difference of Eqs. (4.23) and (4.86).

The low transparency approximation for the Majorana decay length is compared to the full expression in Fig. 4.9 and shows good agreement. The decay length, and hence also the induced minigap are qualitatively the same as the ones for the planar setup, in Sec. 4.2.2.

## 4.4. Conclusions

In this chapter, we employed a semiclassical scattering approach to study a spin-polarized normal-metal quantum wire which is strongly coupled to a spin-orbit-coupled superconductor. This model for a topological superconductor was originally introduced and studied in the limit of an opaque interface between wire and superconductor [Duck 11]. Here, we have shown that the properties of its topological phase are strongly renormalized for a

#### 4. Renormalization effects in spin-polarized metallic wires proximitized by a superconductor: A scattering approach

---

highly transparent interface and provide a semiclassical interpretation. Following previous work on related systems [Peng 15, Das 15, Stic 17, Stan 17], we trace the renormalization to the lowering of the Fermi velocity which we interpret in terms of scattering processes which yield zero net-displacement along the wire as well as a modified spin-flip scattering rate  $\rho_{\text{he}}$ . Specifically, a transparent interface greatly increases both the topological minigap and the localization length of the emerging Majorana bound states as compared to an opaque one. Additionally we find that, while the low transparency prediction for the localization length stays accurate even for transparencies  $\lesssim 0.5$ , the velocity as well as the minigap are strongly renormalized towards small values compared to the low-transparency prediction.

We now compare our semiclassical approach to the previously employed Green function approach of Ref. [Peng 15]. In this approach, the low-energy excitations are studied by accounting for the coupling to the superconductor through the self energy

$$\Sigma(\mathbf{k}, \omega) = -\Gamma \frac{\omega + \Delta \tau_x}{\sqrt{\Delta^2 - \omega^2}}. \quad (4.98)$$

Here,  $\Delta$  is the order parameter inside the superconductor,  $\Gamma$  relates to the coupling strength between wire and superconductor in the normal state, and  $\omega$  is the energy of the subgap excitations of the wire. The self energy is expressed in Nambu notation with the corresponding Pauli matrices denoted by  $\tau_j$  ( $j = x, y, z$ ) and does not yet account for spin-orbit coupling in the superconductor. Thus, the pairing terms  $\propto \tau_x$  describe conventional s-wave pairing and the induced  $p$ -wave pairing requires the addition of spin-orbit coupling.

An interesting feature of Eq. (4.98) is its independence of the wave vector  $\mathbf{k}$ . Consequently, the self energy is local in real space. Within the semiclassical picture of this chapter, this surprising locality can be naturally interpreted in terms of the locality of the scattering processes by the superconductor. Furthermore, the semiclassical approach requires a purely spectral description of the renormalizations. The expression in Eq. (4.98) implies that we can expect such a spectral interpretation in the limit in which  $\omega \ll \Delta$  and the induced gap is small compared to  $\Delta$ . For  $\omega \ll \Delta$ , both the induced pairing term and the quasiparticle weight become independent of  $\omega$ . Then, the subgap spectrum of the wire can be obtained from an effective Hamiltonian, provided that the induced gap is sufficiently small. In the context of the model studied in this chapter, this latter condition is guaranteed by the strong polarization of the wire.

In the Green's function approach of Ref. [Peng 15], the renormalizations of the Hamiltonian parameters are due to the quasiparticle weight. As the coupling between wire and superconductor increases, the quasiparticle weight of the wire Green function is progressively reduced. This renormalization is directly mirrored in factors involving  $4D_N + \xi_N |t_\uparrow|^2$  in the semiclassical approach of this chapter. Such factors are involved in the semiclassical expressions (4.25) and (4.43) for the Fermi velocity and the induced gap of the normal metal, respectively. Correspondingly, both quantities involve renormalizations by the quasiparticle weight in the Green function approach. At the same time, the quasiparticle weight drops out from the localization length of the Majorana bound state (or, equivalently, the coherence length of the induced superconductivity) since it is the ratio of Fermi velocity and induced gap. Again, this is consistent with our semiclassical approach

which also does not involve a factor  $4D_N + \xi_N |t_\uparrow|^2$  in Eqs. (4.47) and (4.48). Note that despite this absence of renormalization, the Majorana localization length depends on the bare system parameters in a highly unexpected way, as it is independent of the gap of the superconductor (see also [Stic 17]).

We finally note that our analysis excluded the presence of disorder which may or may not affect the properties of the topological phase. As discussed earlier [Kupf 11, Duck 11], for a mean free path  $\ell$  in the wire, much larger than the microscopic length scales, the single reflection amplitude  $\rho_{\text{he}} \delta L$  is not affected by weak disorder since it is obtained by matching the wavefunctions at the short scale of the half-metal - superconductor interface. In contrast, the derivation of the reflection amplitude  $r_{\text{he}}^{\text{eff}}$  includes multiple scattering processes at a length scale  $1/|\rho_{\text{he}}|$ . In the absence of disorder, these add coherently to  $r_{\text{he}}^{\text{eff}}$  because  $k_x$  is conserved. Including disorder with  $\ell \ll 1/|\rho_{\text{he}}|$  leads to contributions from different  $k_x$  for different scattering paths. Additionally, based on symmetry arguments it can be shown that  $r_{\text{he}}$  is anti-symmetric in  $k_x$  [Kupf 11]. Hence the sum over the different paths is incoherent and there is no guarantee that  $r_{\text{he}}^{\text{eff}}$  is unaffected by disorder. However, if  $\ell \gg 1/|\rho_{\text{he}}|$  the amplitudes still add coherently, and disorder is expected not to play a role [Kupf 11, Duck 11]. Since  $1/|\rho_{\text{he}}|$  is strongly decreased for a highly transparent interface, we conclude that high transparencies lead to a better protection from disorder for the Majorana bound states.



## 5. Proximity induced gap in nanowires with a thin superconducting coating

Recent experiments on semiconductor-superconductor hybrids in a magnetic field use very thin, epitaxially grown superconductors [Chan 15, Deng 16, Albr 16, Zhan 18]. Besides reducing the size of the experimental setup, these thin shells are advantageous as they reduce the magnetic flux through the superconductor for fields parallel to the wire and as they can be epitaxially grown on top of the nanowire, which allows for very clean interfaces between the two materials [Krog 15]. The latter is believed to be responsible for a hard proximity-induced gap which has been achieved in experiments [Chan 15].

Looking at the typical length scale of the system, these results are rather surprising, as the coherence length in Al is of the order of a  $\mu\text{m}$ , much larger than the thickness of the superconducting coat, and hence finite-size effects are expected to play a role. Similar to our analysis in chapter 4, early studies have focused on nanowire - superconductor heterostructures where the finite-size effects can be neglected [Sau 10, Duck 11, Zyuz 13, Peng 15, Heck 16]. More recent studies have considered the implications of a finite thickness of the superconductor. For a one-dimensional wire proximitized by two- or three dimensional thin superconducting coats, it has been suggested that finite-size effects can be detrimental for the induced gap [Reeg 17, Reeg 18a, Reeg 18b]. Other works have considered the effects of a spatially varying electrostatic potential. Under suitable conditions, this may allow for charge accumulation at the wire-superconductor interface and thus promote the proximity effect by pushing the wavefunction inside the nanowire closer to the interface [Anti 18, Mikk 18, Wood 18].

In the experiments, the interface between the epitaxially grown Al and the nanowire is expected to be clean [Krog 15], but the exposed surface of Al might introduce a sizable amount of disorder or surface roughness. So far, disorder has been studied for wide superconductors coupled to nanowires, with disorder present in the wire [Akhn 11, Brou 11a, Diez 12, Liu 12, Stan 12, Bagr 12, Stan 11, Rain 13], the wire surface, [Stan 11, Sau 12] at the end of the wire [Pien 12], and inside the superconductor [Stan 11, Cole 16]. A recent study investigated nanowires proximitized by a thin, disordered superconducting layer [Reeg 18a] and found that disorder can enhance the induced gap.

In this chapter, we will investigate both two and three dimensional thin superconducting coats (S) coupled to a single-mode nanowire (N), with a cross section as the one in shown in Fig. 5.1. We define thin superconductors as those where the thickness  $D_S$  is small compared to the coherence length in S. Our goal is to gain an understanding of what are the impacts of the finite superconductor thickness, dimensionality, and disorder on the induced gap in these systems. We consider disorder located in the bulk or at the surface of the superconductor.

This chapter is structured as follows. In Sec. 5.1, we use a semiclassical approach to

give an overview of the size of the induced gap in different regimes. We present our model of interest in Sec. 5.2 and derive the wavefunctions in the absence of disorder and superconductivity in Sec. 5.3. These form the basis of our analysis. In Sec. 5.4, we include superconductivity and derive the induced gap of the system explicitly up to a transcendental equation, which we solve numerically as well as analytically in certain limits. In Sec. 5.5 we include disorder in our discussion and derive analytical expression of  $\Delta_{\text{ind}}$  by using a semiclassical ansatz. Sec. 5.6 introduces a numerical scattering approach that allows us to calculate the density of states in the presence of disorder. We present the results in Sec. 5.6.2. Finally, we conclude in Sec. 5.7.

### 5.1. Induced gap from a semiclassical point of view

A semiclassical understanding of the magnitude of the induced gap  $\Delta_{\text{ind}}$  can be obtained as follows. For a sufficiently small pairing potential  $\Delta$ , the transverse modes of the N-S junction shown in Fig. 5.1 are well described by a metal-metal junction where  $\Delta$  is zero inside S. Within a semiclassical picture, the wavefunctions of such a metal-metal junction correspond to propagating electrons and holes, with quantized transverse momenta if no disorder is present. Superconductivity only plays a role at long length-scales of the order of the coherence length  $\xi = \hbar v_S / \Delta$ , where  $v_S$  is the Fermi velocity inside the superconductor. Electrons propagating in S are retroreflected into holes at this length scale, and this process takes a time  $\hbar / \Delta$ .

We identify the time  $\hbar / \Delta_{\text{ind}}$  with the maximum time scale an electron can propagate in the N-S junction, before it is retroreflected as a hole. In the simplest case of no N-region, this leads to a gap of magnitude  $\Delta$ . In the presence of N, electrons that can be transmitted into N are retroreflected into holes at a slower time scale, because the time spent in the normal region has to be added on top of  $\hbar / \Delta$ . Consequently, the induced gap reduces. By identifying the induced gap with the time of retroreflection, we assume that the quasiparticles propagate classically, which neglects interference effects.

To further discuss the magnitude of the induced gap, first let us consider the setup shown in Fig. 5.1 in the absence of disorder. Hopping between N and S modes has to preserve momentum in the  $x$ - and  $y$ - direction, and fixing these momenta leaves the momentum along  $z$ , which, for a weak coupling and a small interface transparency, is essentially quantized with a spacing of  $\pi / D_S$ . This translates to a large energy spacing for small  $D_S$  and generically a mode propagating in N will couple off-resonantly to S. Hence, these modes have little overlap into S, and the induced gap becomes small, which is in agreement with Ref. [Reeg 17].

Next, we consider an interface transparency close to unity, which requires approximately matching Fermi velocities in S and N. Not all quasiparticles that propagate in S can hop into N, because the Fermi wavenumber in semiconductors is typically much smaller than the Fermi wavenumber in superconductors. Hence for a quasiparticle in S to enter into N, it has to have a small momentum along  $k_x$  and thus has to propagate almost perpendicular to the interface, as shown in the middle of Fig. 5.1. Quasiparticles propagating under other angles will be totally reflected at the interface, as shown in the left part of Fig. 5.1, and will be gapped out with a gap of size  $\Delta$ , which leaves the modes that can penetrate into

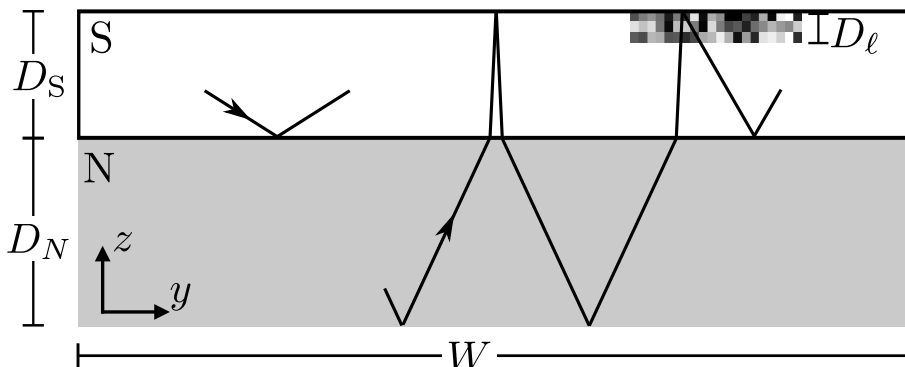


Figure 5.1.: Cross section of normal-metal wire (N) coated by a thin superconductor (S), and sketch of the relevant semiclassical scattering processes. For better visibility a rectangular cross-section is shown, although we typically choose N close to a square ( $D_N \approx W$ ). The left scattering process describes quasiparticles hitting the interface at a non-perpendicular angle. These are mostly totally reflected due to the large wavenumber in S compared to the one in N. Only for almost perpendicular incidence at the interface, quasiparticles can enter N (middle). Surface disorder, indicated in the top right, scatters modes that can enter N into modes that are totally reflected at the interface.

N to lower the gap. For a single mode in N with a velocity  $v_{Nz}$  in the  $z$  direction, the ratio of the times spent in N and S is  $D_N v_S / v_{Nz} D_S$ . The total time spent in S is  $\hbar / \Delta^{-1}$ , which leads to the induced gap

$$\Delta_{\text{ind}} = \frac{\Delta}{1 + D_N v_S / D_S v_{Nz}}. \quad (5.1)$$

Since the velocities are approximately matching and  $D_N / D_S$  is large in the experiments,  $\Delta_{\text{ind}}$  is still small, compared to the bulk gap  $\Delta$ .

The gap can be further enhanced by the inclusion of disorder in S. For unit transparency, after an electron propagating in N enters S, disorder can scatter it into all possible angles. If the disorder is strong enough, quasiparticles propagating in N will be scattered into an arbitrary angle after they enter the superconductor. Since only a few modes propagate perpendicular to the interface and thus can enter N, it is unlikely for the quasiparticle to return into the normal region through disorder scattering, as is indicated in the right part of Fig. 5.1. Instead, it will be retroreflected as hole after a time  $\hbar / \Delta$ . The total rate of scattering from an electron into a hole, and hence the induced gap, is

$$\Delta_{\text{ind}} = \frac{\Delta}{1 + 2D_N v_S / \xi v_{Nz}}, \quad (5.2)$$

where  $\xi = \hbar v_S / \Delta$  is the coherence length of S in the absence of N and the factor 2 is due to the normal region being traversed once as an electron and once as an hole. For current experiments that typically use aluminium as a superconductor [Krog 15, Chan 15,

Deng 16, Albr 16, Zhan 18],  $\xi$  is much larger than  $D_N$ . Thus the induced gap is expected to be of order  $\Delta$ , which is in agreement with experimental observations. We note that a similar reasoning has been used in Ref. [Reeg 18a] in order to argue that in the presence of disorder the induced gap is expected to increase and can reach a magnitude close to  $\Delta$ .

## 5.2. Model

In the remainder of this chapter, we consider a normal-metal (N) wire coupled to a thin superconducting layer (S). The cross section is shown in Fig. 5.1, with the  $x$  direction along the wire. Both materials have a width  $W$  in the  $y$  direction, the superconductor has a thickness  $D_S$ , and the semiconductor wire has a thickness  $D_N$  in the  $z$  direction. The interface between the two materials is located at  $z = 0$  and  $0 < y < W$ . The  $2 \times 2$  Bogoliubov-de Gennes Hamiltonian reads

$$\hat{\mathcal{H}} = \begin{pmatrix} \hat{H}_0 & \theta(z)\Delta \\ \theta(z)\Delta & -\hat{H}_0^* \end{pmatrix}, \quad (5.3)$$

for a spinor wavefunction  $\psi = (u, v)^T$  consisting of particle and hole wavefunctions of opposite spin, and we choose the gauge of a real pairing potential  $\Delta$ . The Heaviside step function  $\theta(z)$  restricts the gap to be finite in S only. The normal-state Hamiltonian  $\hat{H}_0$  is

$$\hat{H}_0 = \xi_{\mathbf{p}}(z) + V_{\text{conf}}(y, z) + U(\mathbf{r}). \quad (5.4)$$

We consider the parabolic dispersion

$$\xi_{\mathbf{p}}(z) = \mathbf{p}_{\perp} \frac{1}{2m(z)} \mathbf{p}_{\perp} + \frac{p_x^2}{2m_x(z)} - \mu(z), \quad (5.5)$$

where

$$\mu(z) = \frac{\hbar^2 k_S^2}{2m_S}, \quad (5.6)$$

$$m(z) = m_x(z) = m_S, \quad (5.7)$$

in the superconductor (i.e.  $z > 0$ ), and

$$\mu(z) = \frac{\hbar^2 k_N^2}{2m_N}, \quad (5.8)$$

$$m(z) = m_N, \quad (5.9)$$

$$m_x(z) = m_{N_x}. \quad (5.10)$$

in the wire ( $z < 0$ ). Here,  $p_x$ ,  $\mathbf{p}_{\perp} = (p_y, p_z)$  are the momenta along  $x$ ,  $y$  and  $z$ ,  $k_S$  and  $k_N$  are the Fermi wavenumbers, and  $m_S$  and  $m_N$  the masses in S and N. We leave the option to choose a different mass  $m_{N_x}$  along the  $x$  direction in N, which as we argue in section 5.6 does not qualitatively change the physics while it simplifies our numerics. The confining potential  $V_{\text{conf}}(y, z)$  models the sample boundary,  $V_{\text{conf}}(y, z) = 0$  for  $-D_N < z < D_S$  and  $0 < y < W$ , and  $V_{\text{conf}}(y, z) = \infty$  otherwise. We assume disorder to be

present at the exposed top boundary of the superconductor with an extension  $D_\ell$  into the superconductor. We model the corresponding potential  $V(\mathbf{r})$  as Gaussian white noise with zero mean and the correlation

$$\langle U(\mathbf{r})U(\mathbf{r}') \rangle = \frac{\hbar v_S}{2\pi\nu_0\ell} \delta_\lambda(\mathbf{r} - \mathbf{r}'), \quad (5.11)$$

with support for  $0 \leq D_S - D_\ell \leq z \leq D_S$  only. Here,  $v_S = \hbar k_S/m$  and the densities of states per spin direction in two and three dimensions read  $\nu_0 = k_S/2\pi\hbar v_S$  and  $\nu_0 = k_S^2/2\pi^2\hbar v_S$ , respectively. The parameter  $\ell$  corresponds to the mean free path in the disorder region if  $k_S\ell \gtrsim \pi$ . For surface disorder potential fluctuations are expected to be of the order of  $\hbar^2 k_S^2/2m_S$  and one expects diffusive boundary scattering. In this case,  $\ell$  no longer corresponds to the mean free path and scattering from the top boundary is expected to saturate with an effective mean free path of order  $D_S$ .

### 5.3. Metal-metal junction

In this section, we derive the wavefunctions for a metal-metal junction in the absence of disorder, described by Eqs. (5.3) to (5.10) with  $\Delta = 0$ . These will form the basis of our subsequent analysis.

We write the wavefunction, normalized to unit flux along the  $x$  direction, as

$$\psi_\nu(\mathbf{r}, \varepsilon) = \frac{e^{is\tau k_x(\tau\varepsilon)x} \sin \frac{\pi n_y}{W} y}{\sqrt{W\hbar v_x/2}} \psi_{\perp\tau, n_z}(z, \varepsilon), \quad (5.12)$$

with a multi-index  $\nu = (s, \tau, n_y, n_z)$ , direction of propagation  $s = \pm$ , longitudinal momentum  $k_x$ , velocity  $v_x = \hbar|d\varepsilon/dk_x|$ , and positive integer quantum numbers  $n_y$  and  $n_z$  describing the quantized momenta in the transverse directions. We use  $\tau = e(h)$  to index the electron-hole subspace if  $\tau$  appears as an index, and  $\tau = 1(-1)$  otherwise. The components along  $z$  read

$$\psi_{\perp e, n_z}(z, \varepsilon) = \frac{c_e e^{ik_{Nz}(\varepsilon)z} + c'_e e^{-ik_{Nz}(\varepsilon)z}}{\sqrt{v_{Nz}(\varepsilon)\mathcal{N}_{e, n_z}}}, \quad (5.13)$$

$$\psi_{\perp h, n_z}(z, \varepsilon) = \frac{c_h e^{-ik_{Nz}^*(-\varepsilon)z} + c'_h e^{ik_{Nz}^*(-\varepsilon)z}}{\sqrt{v_{Nz}(-\varepsilon)\mathcal{N}_{h, n_z}}} \quad (5.14)$$

for  $z < 0$  and

$$\psi_{\perp\tau, n_z}(z) = \frac{d_\tau e^{-i\tau k_{Sz}z} + d'_\tau e^{i\tau k_{Sz}z}}{\sqrt{v_{Sz}\mathcal{N}_{\tau, n_z}}} \quad (5.15)$$

for  $z > 0$ . Here,  $\mathcal{N}_{\tau, n_z}$  are normalization constants such that  $\int dz |\psi_{\perp\tau, n_z}(z)|^2 = 1$ ,

$$k_{Nz}(\varepsilon) = \sqrt{k_N^2 - k_y^2 + \frac{m_N}{m_{Nx}} (k_{Sz}^2 + k_y^2 - k_S^2) + 2m_N \left(1 - \frac{m_S}{m_{Nx}}\right) \varepsilon}, \quad (5.16)$$

$$k_x(\varepsilon) = \sqrt{k_S^2 - k_{Sz}^2 - (n_y\pi/W)^2 + 2m_S\varepsilon/\hbar^2}, \quad (5.17)$$

$$v_{Sz} = k_{Sz}/m_S, \quad (5.18)$$

$$v_{Nz} = k_{Nz}/m_N, \quad (5.19)$$

where, in our notation, we drop the multi-index  $\nu$  for the wavenumbers and velocities. We assume that  $k_S \geq k_N$  and within a semiclassical approximation consider only real  $k_x$ . In this case  $k_{S_z}$  is real, while  $k_{N_z}$  lies either on the real or the imaginary axis and  $n_y$  is bounded from above correspondingly.

Next, we determine the relations between the  $c_\tau$  and  $d_\tau$  coefficients and derive the quantization condition for  $k_{S_z}$ . Upon applying the matching conditions at the interface, continuity in  $\psi$  and the first spatial derivative, similar to [Kupf 09], one finds

$$\begin{pmatrix} c'_e \\ d'_e \\ c'_h \\ d'_h \end{pmatrix} = \begin{pmatrix} r & t' & 0 & 0 \\ t & r' & 0 & 0 \\ 0 & 0 & r^* & (t')^* \\ 0 & 0 & t^* & (r')^* \end{pmatrix} \begin{pmatrix} c_e \\ d_e \\ c_h \\ d_h \end{pmatrix} \quad (5.20)$$

Here, we introduced the interface transmission and reflection amplitudes

$$t = \frac{2\sqrt{v_{S_z}v_{N_z}}}{v_{S_z} + v_{N_z}}, \quad (5.21)$$

$$t' = \frac{2\sqrt{v_{N_z}v_{S_z}}}{v_{S_z} + v_{N_z}}, \quad (5.22)$$

$$r = -1 + t\sqrt{v_{N_z}/v_{S_z}}, \quad (5.23)$$

$$r' = -1 + t'\sqrt{v_{S_z}/v_{N_z}}. \quad (5.24)$$

For our later analysis it is useful to define the transmission amplitude for perpendicular incidence

$$t_\perp = \frac{2\sqrt{v_S v_N}}{v_S + v_N}, \quad (5.25)$$

where  $v_S = \hbar k_S/m_S$  and  $v_N = \hbar k_N/m_N$ .

The amplitudes have to vanish at  $z = -D_N$  and  $z = D_S$ , which gives

$$c'_e = -c_e e^{-2ik_{N_z}(\varepsilon)D_N}, \quad (5.26)$$

$$c'_h = -c_h e^{2ik_{N_z}^*(-\varepsilon)D_N}, \quad (5.27)$$

$$d'_\tau = -d_\tau e^{-2i\tau k_{S_z} D_S}. \quad (5.28)$$

Equations (5.20) and (5.26) to (5.28) fully determine the wavefunction, and yield the transcendental equation

$$0 = v_{N_z} \cot k_{N_z}(\tau\varepsilon)D_N + v_{S_z} \cot k_{S_z}D_S. \quad (5.29)$$

Note that  $k_{N_z}$  depends on  $k_{S_z}$  via equations (5.16). Solving Eq. 5.29 numerically yields the quantized values for  $k_{S_z}(\tau\varepsilon)$  and is now dependent on  $\tau\varepsilon$  via Eq. (5.29). We label the solutions by integer index  $n_z$ . Furthermore, we choose  $c_\tau = 1$  which fixes the remaining  $c$ - and  $d$ -coefficients and leads to

$$\mathcal{N}_{\tau, n_z} = \frac{2D_S}{v_{S_z}} |d_\tau|^2 \left( 1 - \frac{\sin 2k_{S_z} D_S}{2k_{S_z} D_S} \right) + \frac{e^{4D_N \text{Im} k_{N_z}} - 1}{2\text{Im} k_{N_z} |v_{N_z}|} - e^{2D_N \text{Im} k_{N_z}} \frac{\sin 2D_N \text{Re} k_{N_z}}{|v_{N_z}| \text{Re} k_{N_z}}. \quad (5.30)$$

Here we drop the dependence on  $\tau\varepsilon$  for the sake of compactness.

## 5.4. Excitation gap in the absence of disorder

Next, we consider the system described by Eq. (5.3) in the absence of disorder and derive the gap of the system in the presence of a pairing potential  $\Delta$ .

We start by expressing the Hamiltonian (5.3) in the basis of the wavefunctions (5.12). We assume the limit of  $\xi/D_S$ ,  $\xi/W \gg 1$ , such that the transverse modes are well described by the transverse components in Eq. (5.12). Furthermore, when a mode in the superconductor becomes resonant with one in the wire they split due to the tunnel coupling and the presence of the pairing potential. We assume  $\Delta$  to be small enough, such that the splitting is dominated by the tunnel coupling. Finally, we note that in the absence of disorder, Eq. (5.3) is diagonal in  $n_y$ .

The resulting low-energy Hamiltonian for fixed quantum number  $n_y$  reads

$$H_{\text{eff},n_y} = \sum_{\alpha} |\psi_{\perp,\alpha}(\varepsilon_{\alpha,\hat{k}_x})\rangle \varepsilon_{\alpha,\hat{k}_x} \langle \psi_{\perp,\alpha}(\varepsilon_{\alpha,\hat{k}_x})| + |\psi_{\perp,\alpha}(\varepsilon_{\alpha,\hat{k}_x})\rangle \Delta_{\alpha}(\varepsilon_{\alpha,\hat{k}_x}, \varepsilon_{\bar{\alpha},\hat{k}_x}) \langle \psi_{\perp,\bar{\alpha}}(\varepsilon_{\bar{\alpha},\hat{k}_x})|, \quad (5.31)$$

where the sum is over the multi index  $\alpha = (\tau, n_z)$ , and  $\bar{\alpha} = (\bar{\tau}, n_z)$  with a flipped particle-hole index  $\bar{\tau}$ . The wavefunctions  $\psi_{\perp,\alpha}(\varepsilon_{\alpha k_x})$  are defined in Eqs. (5.13) to (5.15). Furthermore, we introduced

$$\varepsilon_{\alpha,k_x} = \tau \frac{k_{S_z}^2 + (n_y \pi / W)^2 + k_x^2 - k_S^2}{2m_S}, \quad (5.32)$$

$$\Delta_{\alpha,k_x} = \Delta \langle \psi_{\perp,\alpha}(\varepsilon_{\alpha k_x}) | \theta(\hat{z}) | \psi_{\perp,\bar{\alpha}}(\varepsilon_{\bar{\alpha} k_x}) \rangle. \quad (5.33)$$

Equation (5.31) describes a multichannel wire along the  $x$  direction, where the modes labeled with different  $n_y$  and  $k_{S_z}$  do not mix, and each mode has its own pairing potential  $\Delta_{\alpha,k_x}$ . We can further simplify this model by noting that the modes localized mostly in the normal region and close to the Fermi level will give the overall gap of the system. For these modes we neglect the dependence on  $\varepsilon_{\alpha,k_x}$  in  $\psi_{\perp}$  and get the  $k_x$ -independent pairing potential

$$\Delta_{\alpha} = \Delta \langle \psi_{\perp,\tau,n_z}(0) | \theta(\hat{z}) | \psi_{\perp,\bar{\tau},n_z}(0) \rangle, \quad (5.34)$$

Within the Andreev approximation,  $\hbar^2(k_x(0))^2/m|\Delta_{\alpha}| \gg 1$ , each mode  $\alpha$  has a gap of magnitude  $|\Delta_{\alpha}|$ , and the overall gap of the system is

$$\Delta_{\text{ind}} = \min_{\alpha} |\Delta_{\alpha}| \quad (5.35)$$

At the Fermi level, the  $\tau$  and  $\bar{\tau}$  wavefunctions are related by particle-hole symmetry, and we find that  $|\Delta_{\alpha}|$  is equal to the overlap of the normalized wavefunction  $|\psi_{\alpha}\rangle$  with the superconductor. This overlap is independent of the extension in the  $y$  direction, and consequently  $\Delta_{\text{ind}}$  does not depend on the width  $W$ .

Upon evaluating Eq. (5.34), we obtain

$$\Delta_{\alpha} = \frac{2D_S\Delta}{v_{S_z}\mathcal{N}_{\alpha}} |d_{\alpha}|^2 \left( 1 - \frac{\sin 2k_{S_z}D_S}{2k_{S_z}D_S} \right), \quad (5.36)$$

where

$$|d_\alpha|^2 = \left| \frac{v_{Nz} \cos k_{Nz} D_N - i v_{Sz} \sin k_{Nz} D_N}{v_{Sz} \cos k_{Sz} D_S - i v_{Nz} \sin k_{Sz} D_S} \right| e^{-\text{Im} k_{Nz} D_N}, \quad (5.37)$$

Due to the exponential factor in Eq. (5.37), which also appears in  $\mathcal{N}_\alpha$ , modes evanescent in the normal region will have  $\Delta_\alpha \approx \Delta$ , with corrections that are exponentially suppressed in  $\text{Im} k_{Nz} D_N$ . (Note that we use the convention  $\text{Im} k_{Nz} < 0$ .) In the following discussion of limiting cases, we focus on modes with real  $k_{Nz}$ . Furthermore, we consider the regime of a single mode inside the normal region below the Fermi level,  $1 \lesssim k_N D_N / \pi < 2$  and  $1 \lesssim k_N W / \pi < 2$ , set  $m_{Nx} = m_N$ , and take the limits  $k_S \gg k_N$ ,  $m_S \gg m_N$  and  $k_S D_S \gg 1$ , which are the relevant parameter regimes of current experiments based on semiconductor-superconductor hybrids.

First, we discuss the case of unit transparency, which corresponds to  $v_{Nz} = v_{Sz}$ . In the limit  $k_S \gg k_N$ , we have  $k_{Sz} \approx k_S$  and since  $v_{Nz}$  lies between 0 and  $v_N$ , we require  $v_N > v_S$  for this to occur. Furthermore, the parameters have to be tuned in order to fulfill Eq. (5.29), which yields

$$k_S D_S + v_S m_N D_N = n\pi, \quad (5.38)$$

for any positive integer  $n$ . In order to obtain  $\Delta_{\text{ind}}$  from Eq. (5.35) we argue that since we consider the regime of a single mode in the wire, and since the remaining modes in the superconductor have an evanescent overlap with the wire, the mode with unit transparency will have the minimum  $|\Delta_\alpha|$ . After evaluating Eq. (5.36), we obtain

$$\Delta_{\text{ind}} = \Delta \left[ 1 + \frac{D_N}{D_S} \left( 1 - \frac{\sin 2k_{Nz} D_N}{2k_{Nz} D_N} \right) \right]^{-1}. \quad (5.39)$$

Equation (5.39) agrees with Eq. (5.1) for matching velocities, up to the interference term in parentheses, which is of order unity. In the derivation of Eq. (5.1), we assumed a classical propagation of electrons and holes, which explains the absence of the interference term.

Next, we derive the induced gap in the limit in the limit  $v_S/v_N \gg 1$  and  $k_S^2/k_N^2 \gg k_S D_S$ . In order to solve Eq. (5.29), we expand around the solution for zero transparency and at the Fermi level,

$$k_{Sz} = \left( n_S + \frac{1}{2} \right) \frac{\pi}{D_S} + \delta q, \quad (5.40)$$

$$k_{Nz} = \frac{\pi}{D_N} + \delta k, \quad (5.41)$$

with

$$n_S = \lfloor k_S D_S / \pi \rfloor, \quad (5.42)$$

$$\delta q = k_S - \left( n_S + \frac{1}{2} \right) \frac{\pi}{D_S}, \quad (5.43)$$

where  $\lfloor \cdot \rfloor$  denotes the floor function. Here, we neglected the contribution of  $\delta k$  to  $k_{Sz}$ , which is justified in the limit  $k_N^2/k_S^2 \gg k_S D_S$ . Expanding Eq. (5.29) to lowest order in  $\delta q$  and  $\delta k$  yields,

$$\frac{\pi}{m_N D_N^2 \delta k} + \frac{1}{m_N D_N} = v_S \delta q, \quad (5.44)$$

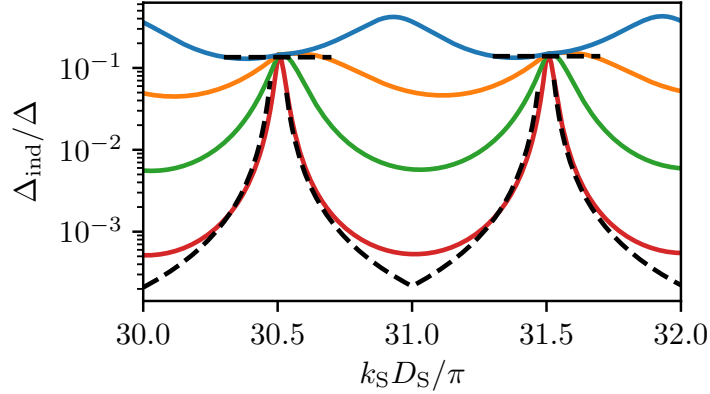


Figure 5.2.: Induced gap in the absence of disorder. We choose a velocity mismatch  $v_N/v_S = 0.1, 0.33, 1, 3.3$  for the lowest (red) to the highest lying solid line (blue), respectively. The dashed lines show the prediction at the peak (5.39), and the tails (5.46). The remaining parameters are  $k_N D_N = 1.8\pi$ ,  $k_S/k_N = 100$ .

which has the solution

$$\delta k = \frac{\pi}{m_N D_N^2 v_S \delta q D_S - D_N}. \quad (5.45)$$

For  $1 \gtrsim \delta q D_S \gg v_N/v_S$ , both  $\delta q$  and  $\delta k$  are sufficiently small to justify the lowest order expansion around the zero transparency case. Finally, we argue that for  $\delta q D_S \gtrsim \frac{v_N D_S}{v_S D_N}$  the remaining propagating modes have evanescent overlap into the wire and can be neglected. Thus, the solution (5.45) is expected to contribute the minimum  $|\Delta_\alpha|$ , and from Eq. (5.35) we obtain the induced gap

$$\Delta_{\text{ind}} = \frac{\Delta \pi^2}{D_N^3 v_S^2 m_N^2 \delta q^2 D_S}. \quad (5.46)$$

Figure 5.2 shows numerical results obtained by solving Eqs. (5.29) and (5.35). The resulting effective gap as a function of  $D_S$  is a series of peaks that is approximately  $\pi$  periodic in  $k_S D_S$ . For a small velocity inside the normal region, we find good agreement with Eq. (5.46). For the parameter range shown and  $v_N \leq v_S$ , the peak of the gap is given by Eq. (5.39) and is approximately constant as a function of  $D_S$ . Once  $v_S > v_N$ , we find that the peak gap increases further and its value of  $k_S D_S/\pi$  shifts away from half-integer values.

## 5.5. Semiclassical approach to disordered systems

Next, we consider the presence of disorder in the bulk or at the top surface of the superconductor in the case of approximately matching Fermi velocities in N and S. As discussed in the introduction, disorder is expected to scatter modes with an overlap in N into modes

with no overlap in N. Consequently, the time spent in N gets smaller, which increases the induced gap.

Within a semiclassical picture, we can derive a formula for the induced gap as a function of the mean free path as follows. We consider the case of a single mode in N, that has unit transparency across the interface,  $|t|^2 = 1$ , and assume that the remaining modes have an evanescent overlap into N. In this case, the mode relevant for the induced gap is the one propagating in N, and we can express the induced gap as

$$\Delta_{\text{ind}} = \frac{1}{\Delta^{-1} + 2t_N/\hbar}. \quad (5.47)$$

Here the denominator is the time it takes an electron to propagate in N and S and to return as a retroflected hole. The fraction of time spent in S is  $\hbar\Delta^{-1}$ , and  $t_N$  is the time an electron spends in N, with a factor of 2 due to the retroflected hole spending the same time in N.

In order to parametrize  $t_N$ , we define the probability  $\bar{P}_{e \rightarrow h}$  for an electron *not* to scatter into a hole when performing a round trip from  $z = 0$  to  $z = D_S$  and back again. It reads

$$\bar{P}_{e \rightarrow h} = e^{-4D_S/\xi - 2D_S/\ell_{\text{eff}}} \quad (5.48)$$

Here, the factor  $e^{-4D_S/\xi}$  is the probability not to be directly reflected into a hole during a round trip, excluding the effects of disorder; and  $e^{-2D_S/\ell_{\text{eff}}}$  is the probability to not scatter from disorder and be subsequently reflected as a hole. For the latter we define the effective mean free path  $\ell_{\text{eff}}$ . In the case of bulk disorder we simply have  $\ell_{\text{eff}} = \ell$ . In the case of surface disorder, disorder might well be strong, leading to the saturation of scattering from the surface. Thus, for surface disorder, we set

$$\ell_{\text{eff}} = \frac{D_S}{D_\ell} \max(\ell, a_{\text{sat}}\pi/k_S), \quad (5.49)$$

where  $a_{\text{sat}}$  is a constant of order one and is determined numerically in Sec. 5.6.3. If we assume that disorder scatters the electrons only into angles that cannot enter back into N,  $\bar{P}_{e \rightarrow h}$  corresponds to the probability of not being retroflected as a hole during a round trip.

Each time the electron is *not* retroflected as a hole, an additional time  $\frac{2D_N}{v_{Nz}}$  has to be spent inside N, and we get

$$t_N = \frac{D_N}{v_{Nz}} + \bar{P}_{e \rightarrow h} \frac{2D_N}{v_{Nz}} + \bar{P}_{e \rightarrow h}^2 \frac{2D_N}{v_{Nz}} \dots \quad (5.50)$$

By summing up the geometric series and evaluating Eq. (5.47), we obtain

$$\Delta_{\text{ind}} = \Delta \left( 1 + \frac{2v_S D_N}{v_{Nz} \xi} \frac{1 + \bar{P}_{e \rightarrow h}}{1 - \bar{P}_{e \rightarrow h}} \right)^{-1} \quad (5.51)$$

Notably, the induced gap does not depend on the width  $W$ .

In the no-disorder limit  $\ell_{\text{eff}} \gg \xi \gg D_S$ , Eq. (5.51) reduces to Eqs. (5.1), and in the limit  $\xi \gg D_S \gg \ell_{\text{eff}}$ , it turns into Eq. (5.2). For intermediate disorder strengths,  $\xi \gg \ell_{\text{eff}} \gg D_S$ , we obtain

$$\Delta_{\text{ind}} = \Delta \left( 1 + \frac{v_S D_N \ell_{\text{eff}}}{v_{Nz} D_S \xi} \right)^{-1}, \quad (5.52)$$

which grows monotonically upon increasing the disorder strength  $\ell_{\text{eff}}^{-1}$ .

In our derivation of Eq. (5.51), we assumed that once an electron scatters from disorder, it does not enter again into N. However, an electron might scatter from disorder and enter N one or multiple times. If  $n_S$  modes are present in the superconductor, we expect these processes to become relevant for  $\xi \gtrsim n_S \ell_{\text{eff}}$  only. This is also the scale at which Anderson localization is expected to occur, and hence we cannot access this regime with our semiclassical approach. We note however, that the width  $W$  can be increased to increase the number of modes and push the onset of this regime to larger coherence lengths.

## 5.6. Numerical scattering approach

We compare the estimate in Eq. (5.51) to a numerical calculation. Our numerics employ the thin-slice concatenation method introduced in Sec. 3.3 in order to calculate the scattering matrix  $S(L, \varepsilon)$  of a wire slab of length  $L$  with a cross section as the one shown in Fig. 5.1. Inside the slab, a pairing potential  $\Delta$  as well as disorder is present, as described by the Hamiltonian (5.3). Two semi-infinite leads are attached to the slab at  $x = 0$  and  $x = L$ . The leads are described by the same Hamiltonian as the slab, but with disorder and pairing potential turned off. Once the scattering matrix is known, quantities such as the conductance or density of states can be calculated to infer the gap of the system.

Our analysis is somewhat complicated by the fact that for a  $z$ -dependence in the kinetic energy term  $p_x^2/2m_x(z)$  of the Hamiltonian (5.3), the transverse components  $\psi_{\perp\tau, n_z}(z)$  can be non-orthogonal with respect to  $n_z$ . (Note that the full wavefunctions in (5.12) including the  $x$  and  $y$  dependencies still form an orthonormal set.) In order to circumvent this, we take  $m_x(z) = m_S$  in which case  $\psi_{\perp\tau, n_z}(z)$  form an orthonormal set with respect to  $n_z$ , and at fixed  $n_y$  and  $\tau$ . We argue that this change does not qualitatively alter the results of our analysis, which considers the regime of a single mode inside the normal region. This is because modes in the superconductor have an evanescent overlap into the wire and hence are not affected by a change in the normal region. Since this leaves only the single mode in the normal region, this corresponds to an energy shift for this mode which can be absorbed into  $k_N$ , and consequently only the value of  $k_N$  has to be adjusted.

### 5.6.1. Implementation details

In order to compute  $S(L, \varepsilon)$  along the lines of Sec. 3.3, we split the Hamiltonian (5.3) into

$$\hat{H} = \hat{H}_\varepsilon + \hat{H}'_\varepsilon, \quad (5.53)$$

where

$$\hat{H}_\varepsilon = [\xi_{\mathbf{p}}(z) + V_{\text{conf}}(\mathbf{y}, z)] \tau_z + \varepsilon \quad (5.54)$$

$$\hat{H}'_\varepsilon = \Delta \tau_x + U(\mathbf{r}) \tau_z - \varepsilon, \quad (5.55)$$

and  $\tau_i$  denotes Pauli matrices in particle-hole space. Our goal is to calculate the scattering matrix of a scattering region  $0 < x < L$  described by  $\hat{H}$ , with attached leads described by the Hamiltonian  $\hat{H}_{\varepsilon=0}$  for  $x < 0$  and  $x > L$ . In order to use the concatenation scheme

described in Sec. 3.3, we would need to calculate the matrix elements  $\mathcal{T}_{\nu'\nu}^{(j)}$  for  $\hat{H}'_{\varepsilon=0}$  and the in- and outgoing modes  $\psi_\nu(\mathbf{r}, \varepsilon)$  defined in Eq. (5.12) at finite energy. By instead including the energy as a constant shift in the scattering potential,  $\hat{H}'_\varepsilon$ , we can evaluate the wavefunctions at zero energy and calculate the  $\mathcal{T}$  matrix as

$$\mathcal{T}_{\nu'\nu}^{(j)} = \int_{x_j < x < x_{j+1}} d\mathbf{r} \psi_{\nu'}^\dagger(\mathbf{r}, 0) \hat{H}'_\varepsilon \psi_\nu(\mathbf{r}, 0), \quad (5.56)$$

for a thin slice  $x_j < x < x_{j+1}$ . Here, we introduce the multi-index  $\nu = (s, \tau, n_y, n_z)$ , with propagating direction  $s = \pm$ .

By using the unitarized Born approximation in Eq. (3.28), and concatenating the scattering matrices of the slices according to Eq. (3.29), we obtain the scattering matrix

$$\tilde{S}(L, \varepsilon) = \lim_{N \rightarrow \infty} S_0 \otimes S_1 \otimes \cdots \otimes S_{N-1}, \quad (5.57)$$

in terms of the in- and outgoing modes  $\psi_\nu(\mathbf{r}, 0)$  at zero energy.

For our later calculation, we require  $S(L, \varepsilon)$  for in- and outgoing modes at finite  $\varepsilon$ . The transformation between  $\tilde{S}(L, \varepsilon)$  and  $S(L, \varepsilon)$  is obtained by matching the in- and outgoing modes at finite energy with those at zero energy, at both ends of the scattering region  $x = 0$  and  $x = L$ . This yields the scattering matrices  $S_{\text{left}}$  and  $S_{\text{right}}$ , and we get

$$S(L, \varepsilon) = S_{\text{left}} \otimes \tilde{S}(L, \varepsilon) \otimes S_{\text{right}}. \quad (5.58)$$

For a detailed derivation of  $S_{\text{left/right}}$  and explicit expressions for  $\mathcal{T}_{\nu'\nu}^{(j)}$ , we refer to appendix B.

### 5.6.2. Results on disordered systems

The density of states per unit energy  $\rho(L, \varepsilon)$  can be obtained from the numerically calculated  $S(L, \varepsilon)$  by using the relation [Soum 02]

$$\rho(\varepsilon) = \sum_\nu \frac{L}{v_x(\nu)\pi} + \frac{1}{2\pi i} \text{Tr} S(L, \varepsilon)^\dagger \frac{dS(L, \varepsilon)}{d\varepsilon}. \quad (5.59)$$

Here  $\text{Tr}$  denotes the trace, the first term represents the density of states of a metal at the Fermi surface, and the second term describes how it changes due to the perturbation  $\hat{H}'$ .

We infer the size of the induced gap by noting that if the system is gapped and  $\varepsilon$  lies above the gap,  $\rho(L, \varepsilon)$  is an extensive quantity in  $L$ . In contrast, for  $\varepsilon$  inside the gap,  $\rho(L, \varepsilon)$  converges to a constant value  $\varepsilon$ , which is non-zero due to an evanescent overlap of modes into the wire. The crossover energy between these two behaviors correspond to the size of the gap.

For a two dimensional system, extended in the  $x$ - $z$  plane, the density of states is shown in Fig. 5.3. For all disorder strengths a gap is visible, indicated by the dark region. For small disorder strengths a Van Hove singularity clearly indicates the edge of the induced gap, and at  $\varepsilon \sim \Delta$  the high density of states reflects the bulk gap. Furthermore, for very weak disorder, the induced gap converges to the value predicted by Eq. (5.39) (white

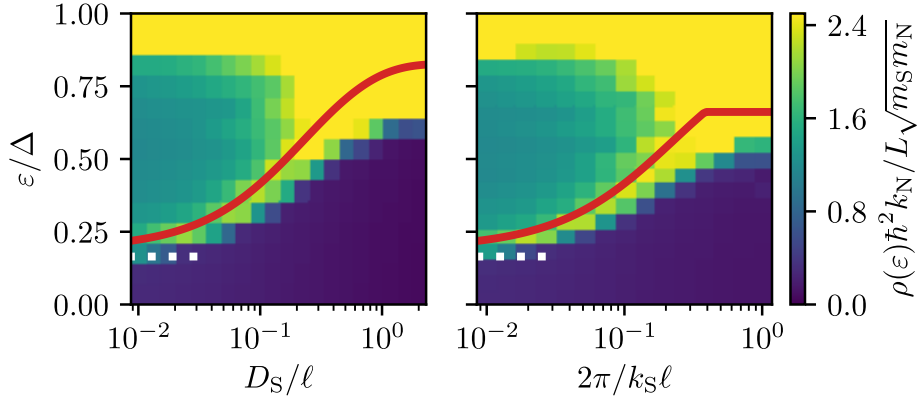


Figure 5.3.: Density of states as a function of energy and disorder strength for a 2d superconductor extended in the  $x - z$  plane. We choose  $\xi/D_S = 40$ ,  $v_N/v_S = 1.5$  and disorder located over the full width of the superconductor (left,  $D_\ell = D_S$ ) and the top surface (right,  $D_\ell = 2\pi/k_S$ ). The white dots show Eq. (5.39) and the red line shows Eq. (5.51) with  $a_{\text{sat}} = 5.2$ . The remaining parameters are  $k_S D_S = 20.4\pi$ ,  $m_S/m_N = 100$ ,  $L/\xi = 8$  and  $k_N D_N = 1.2\pi$ . The density of states is averaged over 5 disorder realizations. Values exceeding the color scale are mapped to the maximum value of the colorbar.

dots). The induced gap starts to increase once the effective mean free path exceeds the coherence length  $\xi$  and shows good agreement with Eq. (5.51) (red line). Finally, for the strongest disorder values shown in Fig. 5.3, the gap reaches values that lie slightly below those predicted by Eq. (5.1). We attribute this smaller value as well as the decrease of the bulk gap visible for large disorder strengths to the onset of Anderson localization. The localization length  $\xi_{\text{loc}}$  is approximately given by the number of transverse modes times  $\ell_{\text{eff}}$ . In Fig. 5.3 about 20 transverse modes are present, leading to  $\xi_{\text{loc}} \sim 20\ell_{\text{eff}}$ . Once,  $\xi_{\text{loc}} < \xi$  Anderson localization is expected to play a role, which is in agreement with Fig. 5.3. We note that moving to three dimensional systems, where a much larger number of transverse modes is accessible, the effects of Anderson localization are expected to become negligible as  $\xi_{\text{loc}}$  becomes large.

Next, we consider a three-dimensional superconductor with a larger number of modes along the  $y$  direction, of which only the mode with  $n_y = 1$  has non-evanescent overlap into the normal region. The results are shown in Fig. 5.4. Clearly, disorder greatly enhances the gap. We attribute this enhancement to the large number of modes along the  $y$  direction ( $n_y \leq 18$ ), since only a small number of modes is present along the  $z$  direction ( $k_S D_S/\pi = 2.4$ ). Furthermore, the results show good agreement with Eqs. (5.39) (red line) and (5.51) (white dots).

### 5.6.3. Saturation of surface disorder scattering

In this section, we discuss the crossover from weak ( $k_S \ell \ll 1$ ) to strong surface disorder ( $k_S \ell \gtrsim 1$ ). We expect that scattering from surface disorder saturates when  $\ell$  becomes

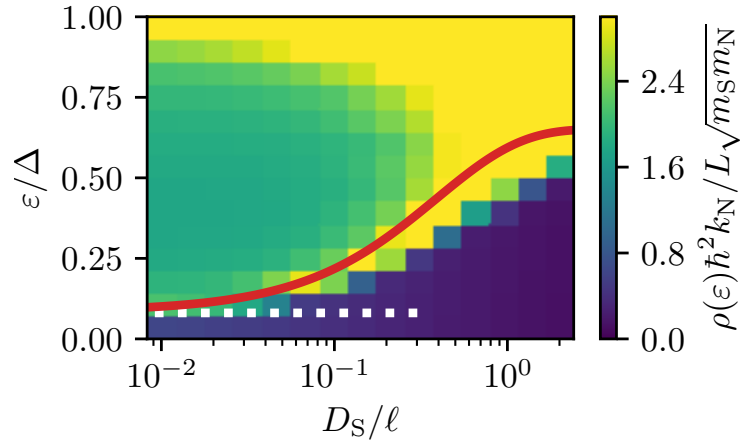


Figure 5.4.: Density of states as a function of energy and disorder strength for a 3d superconductor. We set  $k_S D_S/\pi = 2.4$ ,  $k_S W = 18.7\pi$ ,  $k_N W = 1.4\pi$ , and  $k_N D_N = 1.2\pi$  such that only a single mode has a non-evanescent overlap into N. We choose  $\xi/D_S = 40$ ,  $v_N/v_S = 1.5$  and disorder located over the full width of the superconductor ( $D_\ell = D_S$ ). The white dots show Eq. (5.39) and the red line shows Eq. (5.51). The remaining parameters are  $m_S/m_N = 20$  and  $L/\xi = 22$ . The density of states is averaged over 10 disorder realizations. Values exceeding the color scale are mapped to the maximum value of the colorbar.

small compared to the Fermi wavelength.

We verify this numerically, by considering a two dimensional metal slab of thickness  $D_S$  and length  $L$ , that is connected to two leads. Disorder is present only at one of the surfaces, extending a distance  $D_\ell$  into the superconductor. The system is described by the Hamiltonian (5.3) in the absence of superconductivity and without the additional normal region N.

We access the scattering strength via the conductance at the Fermi level,

$$G(L) = \text{Tr} \left[ \hat{t}^\dagger(L) \hat{t}(L) \right], \quad (5.60)$$

where  $\hat{t}(L)$  is the transmission matrix through the sample, which we obtain by calculating  $S(L, 0)$  according to Sec. 5.6.1, and  $\text{Tr}$  denotes the trace over all scattering channels.

For weak disorder, we approximate the conductance by Ohm's law, which gives

$$G_{\text{ohm}} = \frac{k_S D_S / \pi}{1 + L D_\ell / D_S \ell}. \quad (5.61)$$

Here,  $k_S D_S / \pi$  corresponds to the number of available modes, and we assume that the mean free path in the disorder slab is identical to  $\ell$ . The additional factor  $D_\ell / D_S$  in Eq. (5.61) is the fraction of time an electron spends in the disorder region, when propagating from  $z = 0$  to  $z = D_S$ .

We use the numerical scattering approach described in Sec. (5.6.1) to calculate  $G$ . The results are presented in Fig. 5.5 (a) at a fixed length  $L$ , which is small enough to prevent Anderson localization. For large  $\ell$ , Ohm's law well approximates  $G$ , while for  $\pi / k_S \ell \gtrsim 1$  the conductance saturates. The horizontal lines show the average over the numerically calculated  $G^{-1} - \pi / k_S D_S$  for  $\pi / k_S \ell \geq 1$ .

We now determine the coefficient  $a_{\text{sat}}$  in Eq. (5.49). The mean free path in the saturated region can be approximated by the value  $\ell = \ell_{\text{sat}}$ , at which the inclined and horizontal line in Fig. 5.5 (a) cross. This gives

$$a_{\text{sat}} = \frac{k_S \ell_{\text{sat}}}{\pi}. \quad (5.62)$$

The numerically determined values of  $a_{\text{sat}}$  are shown in Fig. 5.49 (b) and are approximately constant, with a weak dependence on  $D_{\text{ell}} / D_S$ . The marker at  $D_\ell / D_S = 0.1$  corresponds to  $D_\ell = 2\pi / k_S$ , that we use in Fig. 5.3.

The saturation of surface disorder scattering is also visible in the size of the induced gap. Figure 5.6 shows a similar parameter configuration as in Fig. 5.3, but with a smaller coherence length that significantly weakens the impact of Anderson localization at small  $\ell$ . In the case of surface disorder (right), Figure 5.6 shows a clear saturation for small  $\ell$ , which agrees well with Eq. (5.51). In the case of bulk disorder (left), this saturation is not visible, and the induced gap reaches higher values.

## 5.7. Conclusion

In this chapter, we have investigated a normal-metal wire coated by a thin two- or three dimensional superconductor, with disorder in the bulk or at the bare surface of the superconductor.

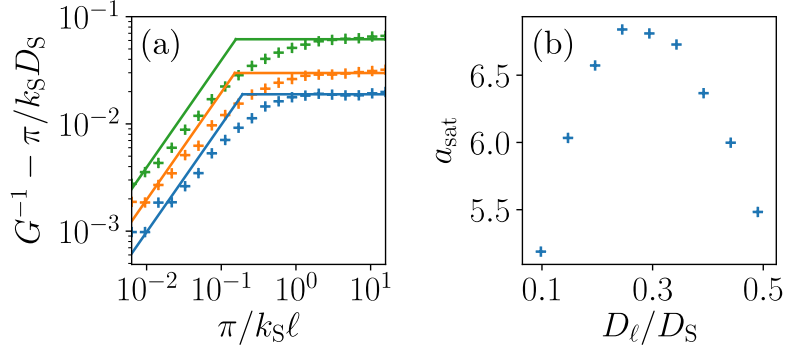


Figure 5.5.: Saturation of scattering for different thicknesses of the disorder region. We choose a normal metal wire of width  $k_S D_S = 20.4\pi$  and  $L = D_S$ . In (a),  $k_S D_\ell/\pi = 2$  (bottom, blue markers), 4, and 8 (top, green markers). The horizontal lines show the average over  $G^{-1} - \pi/k_S D_S$  for  $\pi/k_S \ell \geq 1$ , the inclined lines show Eq. (5.61). The conductance is averaged over 40 disorder realizations. In (b), the coefficient  $a_{\text{sat}}$  is shown, as defined in Eq. (5.62).

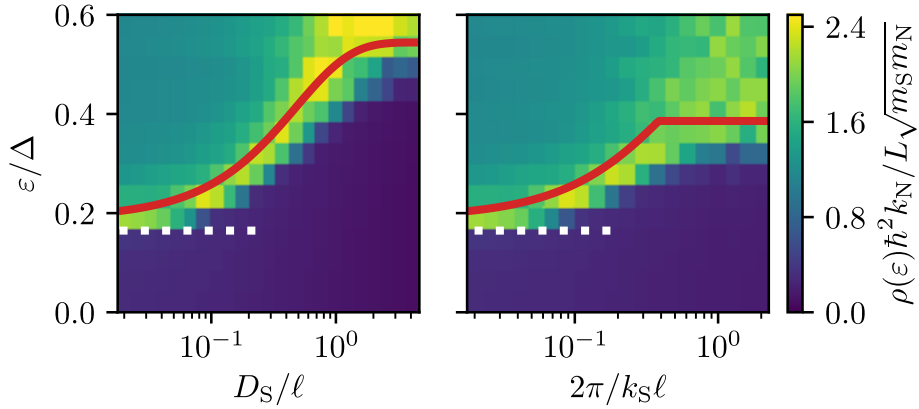


Figure 5.6.: Density of states as a function of energy and disorder strength for a 2d superconductor extended in the  $x - z$  plane. We choose  $\xi/D_S = 10$ ,  $v_N/v_S = 1.5$  and disorder located over the full width of the superconductor (left,  $D_\ell = D_S$ ) and the top surface (right,  $D_\ell = 2\pi/k_S$ ). The white dots show Eq. (5.39) and the red line shows Eq. (5.51) with  $a_{\text{sat}} = 5.2$ . The remaining parameters are  $k_S D_S = 20.4\pi$ ,  $m_S/m_N = 100$ ,  $L/\xi = 8$  and  $k_N D_N = 1.2\pi$ . The density of states is averaged over 8 disorder realizations. Values exceeding the color scale are mapped to the maximum value of the colorbar.

In the absence of disorder and for small interface transparencies, we find that a narrow superconductor leads to a strong suppression of the induced gap, up to resonances that occur periodically when a level in the superconductor passes the wire. For matching Fermi-level velocities in N and S and no interface barrier, which corresponds to the strong-coupling regime, the induced gap is suppressed in the ratio of the material thicknesses,  $D_N/D_S$ , which is large in experiments [Krog 15, Chan 15, Deng 16, Albr 16, Zhan 18].

Our results in the absence of disorder are in qualitative agreement with Ref. [Reeg 17], which studies a one-dimensional wire coupled to a thin superconductor. In their case, the coupling to the superconductor is described by a tunneling energy scale  $\gamma$ , and in our case, the coupling is described by the interface tunneling strength  $|t_\perp|^2$ . In the weak-coupling limit, the two quantities are related by  $\gamma \sim |t_\perp|^2 v_N/D_N$ , and we find that our prediction for the suppression of the induced gap in Eq. (5.46) agree with theirs up to a prefactor of order unity [see Eq. (17) in Ref. [Reeg 17]]. In the case of unit transparency, our results predict a suppression of the induced by a factor  $D_N/D_S$ . In Ref. [Reeg 17], the data with the strongest coupling has  $\Delta_{\text{ind}} \sim \Delta$ , showing no such suppression. We attribute this to the large values of  $\gamma$ , that corresponds to small values of  $D_N/D_S$ .

In the presence of disorder and for approximately matching Fermi velocities, we find that disorder in the bulk or at the surface of the superconductor can significantly enhance the induced gap. We find that this enhancement sets in, when the effective mean free path  $\ell_{\text{eff}}$  in the superconductor becomes smaller than the coherence length  $\xi$ . For the typical case when  $\xi$  is large compared to the thicknesses  $D_N$  and  $D_S$  of N and S, we find an induced gap comparable to  $\Delta$  for  $\ell_{\text{eff}}/\xi \lesssim D_S/D_N$ . In the case of strong disorder at the bare surface of S, which we assume to be present in current experiments,  $\ell_{\text{eff}} \sim D_S$ , and consequently one expects an induced gap of order  $\Delta$ , consistent with experimental observations [Chan 15, Deng 16, Albr 16, Zhan 18].

The authors of Ref. [Reeg 18a] numerically studied a quasi-one-dimensional normal wire coupled to a disordered superconductor. Our results on surface disorder agree with theirs, and they also find that the induced gap is independent of the width  $W$ . In the case of bulk disorder, the authors find only negligible effects of moderate disorder on the induced gap. Our analysis shows that there exists a large regime, where disorder in the bulk of the superconductor can significantly enhance the induced gap.

In conclusion, these findings show that creating thin, superconducting crystals without defects and a flat surfaces is not desirable when trying to induce a sizable gap in semiconductor nanowires. In particular, if the exposed surface of the superconductor would contain no scatterers the induced gap would be strongly suppressed. However, our study shows that this can be counteracted by including impurities in the bulk of the superconductor, which can enhance the induced gap to values close to that of the bare superconductor.



## 6. Effects of nonmagnetic disorder on the energy of Yu-Shiba-Rusinov states

This chapter is based on Ref. [Kien 17] (doi). Copyright remains with ©2017 American Physical Society.

In the previous chapters, we have studied hybrid structures consisting of one-dimensional magnetic materials coupled to two- or three dimensional superconductors in the strong coupling limit. In this section, we reduce the dimensionality of the magnetic materials by one and consider point-like magnetic scatterers. As we discussed in Sec. 2.2, these magnetic scatters can be experimentally realized by for example magnetic adatoms, and will introduce YSR bound states that reside deep inside the gap of the superconductor for a sufficiently strong coupling. Interest in YSR states was recently renewed due to the experimental progress discussed in Sec. 2.2, as well as the possibility to use chains of adatoms to form the Majorana wires that we discussed in chapters 4 and 5. One way to think of the latter is in terms of an effective tight-binding model of hybridized YSR states [Nadj 13, Pien 13, Klin 13, Brau 13, Kim 14, Sche 16].

It is an important question to which degree YSR bound states are sensitive to (nonmagnetic) potential impurities in the superconductor. In the context of individual magnetic impurities, strong sensitivity to potential impurities would make the YSR energies sample and adatom-position specific, reflecting the details of the impurity configuration in the vicinity of the magnetic atom. Similarly, topological superconductivity is known to be sensitive to disorder. Sensitivity of the YSR state to potential scatterers in the superconductor could thus be detrimental to the formation of a topological superconducting phase.

In this chapter, we characterize the sensitivity of YSR states in two and three dimensions to potential scatterers. We find that the YSR states are robust to disorder, even when the mean free path is shorter than the coherence length of the superconductor. The major condition for this robustness is that the disorder induced mean free path is large compared to the Fermi wavelength which is usually satisfied in conventional superconductors. Thus, our findings relax previous claims [Hui 15] that ultraclean superconductors are required for disorder to introduce only a small perturbation. These earlier results do not include a discussion of the Fermi wavelength, which we find to be a crucial parameter when considering the robustness of the YSR energy.

This chapter is structured as follows. In Sec. 6.1 we introduce the model Hamiltonian on which our analysis is based. In Sec. 6.2, we review the YSR wavefunctions in the absence of disorder and present a perturbative analysis of the effect of disorder on the YSR energies. Section 6.3 introduces a scattering approach, which in an approximate analytical approach, allows us to reduce the effects of disorder on the YSR energy to two contributions which can be discussed qualitatively based on symmetry arguments and a random walk model.

In addition, we also employ the scattering approach for a numerical calculation beyond perturbation theory and compare it to the results obtained by perturbation theory. In Sec. 6.4 we discuss the discrepancy of our results and that of [Hui 15]. Finally, we conclude in Sec. 6.5.

## 6.1. Model

The system we consider is described by the BdG Hamiltonian

$$H = \begin{pmatrix} H_0 + V_\uparrow(\mathbf{r}) + U(\mathbf{r}) & \Delta \\ \Delta & -H_0 - V_\downarrow(\mathbf{r}) - U(\mathbf{r}) \end{pmatrix}, \quad (6.1)$$

where  $H_0 = p^2/2m - \hbar^2 k_F^2/2m$ , with  $m$  the (effective) mass and  $k_F$  the Fermi wavenumber,  $\Delta$  the superconducting order parameter, which we choose to be real,  $V_\sigma(\mathbf{r})$  the impurity potential, and  $U(\mathbf{r})$  the disorder potential.

Following Refs. [Yu 65, Shib 68, Rusi 68] we take the impurity to be a classical spin of magnitude  $S$ , located at the origin  $\mathbf{r} = 0$ . Choosing the spin quantization axis along the impurity spin direction, the spin-dependent impurity potential has the form

$$V_\sigma(\mathbf{r}) = (V_0 - JS\sigma)\delta_\lambda(\mathbf{r}). \quad (6.2)$$

Here,  $\delta_\lambda(\mathbf{r})$  represents a short-ranged function with unit integral and range  $\lambda \sim 1/k_F$ ,  $J$  is the exchange coupling strength, and  $V_0$  is the strength of the potential scattering by the impurity.

For the disorder potential  $U(\mathbf{r})$ , we take a Gaussian white noise model, for which  $U(\mathbf{r})$  has zero mean and variance

$$\langle U(\mathbf{r})U(\mathbf{r}') \rangle = \frac{\hbar v_F}{2\pi\nu_0\ell} \delta_\lambda(\mathbf{r} - \mathbf{r}'), \quad (6.3)$$

where  $\ell$  is the elastic mean free path,  $v_F = \hbar k_F/m$  the Fermi velocity, and  $\nu_0$  the density of states per spin direction. [In two dimensions ( $d = 2$ ) and three dimensions ( $d = 3$ ), one has  $\nu_0 = k_F/2\pi\hbar v_F$  and  $\nu_0 = k_F^2/2\pi^2\hbar v_F$ , respectively.] For simplicity, we choose the same short-distance cutoff  $\lambda$  for the disorder potential  $U(\mathbf{r})$  and for the impurity potential  $V_\sigma(\mathbf{r})$ .

The characteristic length scales of the system are illustrated in Fig. 6.1. The superconductor is characterized by the clean-limit superconducting coherence length  $\xi_0 = \hbar v_F/\Delta$ . For weak-coupling superconductors, one has  $k_F\xi_0 \gg 1$ . Also, in superconductors that are good metals in the normal state, one has  $k_F\ell \gg 1$ . We will assume that both inequalities are obeyed in the considerations that follow, but we will not make any assumptions concerning the relative magnitude of the mean free path  $\ell$  and the coherence length  $\xi_0$ . Superconductors with  $\ell \gg \xi_0$  are in the clean limit; superconductors with  $\ell \ll \xi_0$  are in the dirty limit.

## 6.2. Perturbative approach

In the presence of the impurity potential  $V$ , the equation

$$H|\psi\rangle = \varepsilon|\psi\rangle, \quad (6.4)$$

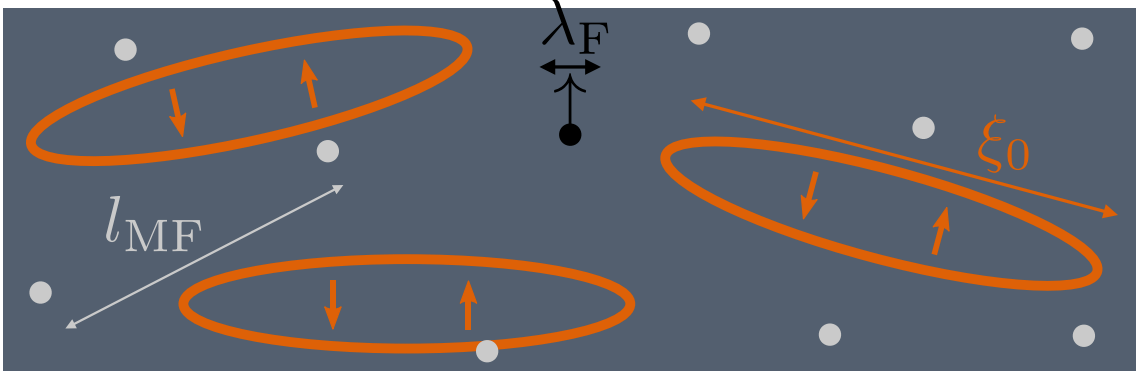


Figure 6.1.: Sketch of the model of this chapter and the relevant length scales. A magnetic adatom (black) with a size comparable to the Fermi wavelength  $\lambda_F$  is placed on top or embedded in a superconductor (dark gray). The superconducting ground state is formed by Cooper pairs, indicated by the orange circles, which have a spatial extension of the order of the coherence length  $\xi_0$ . Nonmagnetic disorder (light gray circles) introduces a mean free path  $\ell$  in the normal state.

with  $H$  given by Eq. (6.1), has a bound-state solution with energy  $|\varepsilon| < \Delta$ . In this section, we review Rusinov's original calculation of the bound-state energy  $\varepsilon_0$  for a clean superconductor [Rusi 68]. We then use this as a starting point to calculate the shift  $\delta\varepsilon = \varepsilon - \varepsilon_0$  to first order in the disorder potential  $U$ .

We start with the general radially symmetric solution of the BdG equation (6.4) for  $r > \lambda$ , where  $\lambda$  is the range of the potential  $V_\sigma(\mathbf{r})$ . For  $k_F \xi_0 \gg 1$ , this reads

$$\psi(\mathbf{r}) = \frac{1}{\sqrt{\xi_\varepsilon}} \sum_{\pm} a_{\pm} \Phi_{\pm}(r) e^{-r/\xi_\varepsilon} \mathbf{b}_{\pm}, \quad (6.5)$$

where  $a_{\pm}$  are complex coefficients,

$$\xi_\varepsilon = \frac{\hbar v_F}{\sqrt{\Delta^2 - \varepsilon^2}} \quad (6.6)$$

is the energy-dependent coherence length,  $\Phi_{\pm}(r)$  solves the radial Schrödinger equation at  $\varepsilon = 0$  in the absence of superconductivity and takes different forms in two and three dimensions,

$$\Phi_{\pm}(r) = \begin{cases} \sqrt{\frac{k_F}{4}} H_0^{\pm}(k_F r) & d = 2, \\ \sqrt{\frac{k_F^2}{4\pi}} h_0^{\pm}(k_F r) & d = 3, \end{cases} \quad (6.7)$$

with  $H^{\pm}$  and  $h^{\pm}$  the Hankel and spherical Hankel functions, respectively, and  $\mathbf{b}_{\pm}$  are two-component spinors,

$$\mathbf{b}_{\pm} = \frac{1}{\sqrt{2}} \begin{pmatrix} 1 \\ e^{\mp i\eta(\varepsilon)} \end{pmatrix}, \quad (6.8)$$

with the Andreev phase

$$\eta(\varepsilon) = \arccos(\varepsilon/\Delta). \quad (6.9)$$

To determine the coefficients  $a_{\pm}$  we use the boundary condition at  $r = \lambda$  imposed by the magnetic impurity. Following Rusinov's original derivation [Rusi 68], we formulate this boundary condition in terms of scattering phase shifts  $\phi_{\sigma}$  for electrons with spin  $\sigma$ . We may neglect the effect of superconductivity on the phase shifts  $\phi_{\sigma}$  since  $\lambda \ll \xi_0$ . The scattering phases  $\phi_{\sigma}$  can be related to the impurity potential (6.2) by [Rusi 68, Clog 62]

$$\tan \phi_{\sigma} = -\pi\nu_0(V_0 - \sigma JS). \quad (6.10)$$

Eq. (6.10) assumes that the range  $\lambda$  of the impurity potential satisfies the inequality  $k_F\lambda \gg 1$ . If  $k_F\lambda \lesssim 1$ , a correction to Eq. (6.10) in the form of a Cauchy principal value integral has to be included into Eq. (6.10), see Ref. [Clog 62]. Since we express our results in terms of the phase shifts  $\phi_{\sigma}$ , these corrections are not important for our considerations.

We note that in the general solution (6.5) the upper component multiplied by  $a_+$  ( $a_-$ ) describes a radial wave for an electron with spin up moving away from (towards) the origin. Hence,

$$a_+ = e^{2i\phi_{\uparrow}} a_-. \quad (6.11)$$

Similarly, the lower component multiplied by  $a_+$  ( $a_-$ ) describes a radial wave moving towards (away from) the origin for a hole in the spin-down band. Taking into account the phase factors  $e^{\pm i\eta(\varepsilon)}$  in the lower component of the spinor (6.8), we find the relation

$$a_- e^{i\eta(\varepsilon)} = e^{-2i\phi_{\downarrow}} a_+ e^{-i\eta(\varepsilon)}. \quad (6.12)$$

Combining these two equations we find the YSR-state energy

$$\varepsilon_0 = \pm\Delta \cos(\phi_{\uparrow} - \phi_{\downarrow}) \quad (6.13)$$

for a magnetic impurity in an (otherwise) clean superconductor. The solution (6.5) is properly normalized if  $|a_+| = |a_-| = 1$  (up to corrections that are small in the limit  $k_F\xi_0, \xi_0/\lambda \gg 1$ ). Note that  $|\varepsilon_0| < \Delta$  if and only if  $\phi_{\uparrow} \neq \phi_{\downarrow}$ , *i.e.*, if the impurity is magnetic.

We now calculate the change  $\delta\varepsilon$  of the energy of the YSR state to first order in the disorder potential  $U(\mathbf{r})$ . We assume that  $U(\mathbf{r}) = 0$  for  $r < \lambda$ , *i.e.*, the disorder potential does not overlap with the potential of the magnetic impurity. To first order in  $U(\mathbf{r})$  the change  $\delta\varepsilon$  is

$$\delta\varepsilon = \int d\mathbf{r} \psi^{\dagger}(\mathbf{r}) U(\mathbf{r}) \tau_z \psi(\mathbf{r}), \quad (6.14)$$

where  $\tau_z$  is the Pauli matrix in particle-hole space and the spinor wavefunction  $\psi(\mathbf{r})$  is given by the general solution (6.5), with the coefficients  $a_{\pm}$  satisfying the relations (6.11) and (6.12). Using the relation  $\Phi_+(k_F r) = [\Phi_-(k_F r)]^*$  this can be simplified as

$$\begin{aligned} \delta\varepsilon &= \sin \eta(\varepsilon_0) \int d\mathbf{r} U(\mathbf{r}) e^{-2r/\xi_{\varepsilon_0}} \\ &\quad \times \text{Im} e^{-i\eta(\varepsilon_0) + 2i\phi_{\uparrow}} [\Phi_+(r)]^2. \end{aligned} \quad (6.15)$$

Using the correlator (6.3), we obtain the variance

$$\begin{aligned} \langle \delta\varepsilon^2 \rangle &= \frac{2\hbar v_F}{\pi\nu_0\ell\xi_{\varepsilon_0}^2} \sin^2 \eta(\varepsilon_0) \\ &\times \int d\mathbf{r} \left\{ \text{Im} e^{-i\eta(\varepsilon_0)+2i\phi_\uparrow} [\Phi_+(r)]^2 \right\}^2 e^{-4r/\xi_{\varepsilon_0}}. \end{aligned} \quad (6.16)$$

In two dimensions the main contribution to the integral (6.16) comes from  $r \sim \xi_{\varepsilon_0}$ . The integral is convergent at the lower limit  $r \downarrow 0$ , so that the short-distance cutoff  $\lambda$  can be taken to zero. We then find

$$\langle \delta\varepsilon^2 \rangle = \frac{\Delta^2(\xi_0/\xi_{\varepsilon_0})^4}{\pi k_F \ell} \log(k_F \xi_{\varepsilon_0}). \quad (6.17)$$

In three dimensions the integral (6.16) is dominated by short distances  $r \sim \lambda \sim k_F^{-1}$  and the short-distance cutoff  $\lambda$  is needed to ensure convergence. In this case we find

$$\langle \delta\varepsilon^2 \rangle \sim \frac{\Delta^2(\xi_0/\xi_{\varepsilon_0})^4}{k_F \ell}, \quad (6.18)$$

where a numerical prefactor depends on the precise way in which the short-distance regularization is implemented. Note that in three dimensions and with  $\varepsilon_0$  well inside the gap such that  $\xi_0/\xi_{\varepsilon_0} \sim 1$ , the variance  $\langle \delta\varepsilon^2 \rangle$  does not depend on  $k_F \xi_{\varepsilon_0}$ .

In two dimensions the root-mean-square fluctuations are parametrically smaller than the superconducting gap  $\Delta$  if the condition  $k_F \ell \gg \log(k_F \xi_0)$  is met. This condition only weakly depends on the superconducting coherence length  $\xi_0$ . In three dimensions the condition is  $k_F \ell \gg 1$ , which is independent of  $\xi_0$ . The latter condition  $k_F \ell \gg 1$  is typically met in superconductors that are good metals in the normal state, such as Pb or Al.

### 6.3. Scattering approach

In this section, we present a numerical calculation of the YSR-state energies that takes higher-order contributions in the disorder potential  $U(\mathbf{r})$  into account. The calculation makes use of a relation between the YSR-state energy  $\varepsilon$  and the scattering matrix  $S(\varepsilon)$  of the superconductor for radial waves moving towards and from the origin  $\mathbf{r} = 0$ . We first describe this relation and the calculation of  $S(\varepsilon)$  separately, and then proceed with a calculation of the variance  $\langle \delta\varepsilon^2 \rangle$ .

#### 6.3.1. Relation between YSR-state energy and scattering amplitudes

To define the scattering matrix  $S$  we introduce a narrow shell  $r_0 < r < r_0 + \delta r$  around the impurity in which the superconducting order parameter  $\Delta$  as well as the potentials  $V$  and  $U$  are set to zero. (At the end of the calculation, we will send the shell width  $\delta r \rightarrow 0$ .) We choose  $r_0 \sim \lambda \lesssim 1/k_F$ . The solution of the BdG equation may be assumed to be radially symmetric, so that it can be expanded as

$$\psi(\mathbf{r}) = \sum_{\pm} [a_{e,\pm} \Phi_{e,\pm}(\mathbf{r}) + a_{h,\pm} \Phi_{h,\pm}(\mathbf{r})], \quad (6.19)$$

where  $\Phi_{e,\pm}$  and  $\Phi_{h,\pm}$  represent flux-normalized electron-like (e) and hole-like (h) waves propagating radially outward (+) or inward (-). In two dimensions one has

$$\begin{aligned}\Phi_{e,\pm}(\mathbf{r}) &= \sqrt{\frac{k_F}{4v_F}} H_0^\pm(k_F r) \begin{pmatrix} 1 \\ 0 \end{pmatrix}, \\ \Phi_{h,\pm}(\mathbf{r}) &= \sqrt{\frac{k_F}{4v_F}} H_0^\mp(k_F r) \begin{pmatrix} 0 \\ 1 \end{pmatrix},\end{aligned}\tag{6.20}$$

whereas in three dimensions

$$\begin{aligned}\Phi_{e,\pm}(\mathbf{r}) &= \sqrt{\frac{k_F^2}{4\pi v_F}} h_0^\pm(k_F r) \begin{pmatrix} 1 \\ 0 \end{pmatrix}, \\ \Phi_{h,\pm}(\mathbf{r}) &= \sqrt{\frac{k_F^2}{4\pi v_F}} h_0^\mp(k_F r) \begin{pmatrix} 0 \\ 1 \end{pmatrix}.\end{aligned}\tag{6.21}$$

The solution of the BdG equation for  $r > r_0 + \delta r$  yields two linear relations for the four amplitudes  $a_{e,\pm}$  and  $a_{h,\pm}$ , which have the general form

$$\begin{pmatrix} a_{e,-} \\ a_{h,-} \end{pmatrix} = S(\varepsilon) \begin{pmatrix} a_{e,+} \\ a_{h,+} \end{pmatrix}, \quad S = \begin{pmatrix} r_{ee} & r_{eh} \\ r_{he} & r_{hh} \end{pmatrix}.\tag{6.22}$$

The matrix  $S$  is the scattering matrix of the superconductor for radial waves around the origin  $\mathbf{r} = 0$ . The coefficients  $r_{ee}$  and  $r_{hh}$  are the amplitudes for normal reflection of electrons and holes, respectively, whereas  $r_{he}$  and  $r_{eh}$  describe Andreev reflection of electrons into holes and vice versa. Time-reversal symmetry and particle-hole symmetry enforce the constraints

$$S(\varepsilon) = S^T(\varepsilon) = \tau_y S(-\varepsilon)^* \tau_y,\tag{6.23}$$

where  $\tau_y$  is a Pauli matrix in particle-hole space.

In the absence of the disorder potential  $U(\mathbf{r})$ , one has  $r_{ee} = r_{hh} = 0$ , and  $r_{eh} = r_{he} = e^{-i\eta(\varepsilon)}$ , with  $\eta(\varepsilon)$  defined in Eq. (6.9). This reproduces Eq. (6.5). In the presence of the disorder potential  $U(\mathbf{r})$ , all four coefficients are in general nonzero. As we will show below, the difference with the clean case is small when  $k_F \ell \gg 1$ , so that we may write

$$S(\varepsilon) = e^{-i\eta(\varepsilon)} \tau_x (\mathbf{1} - i\delta A(\varepsilon)),\tag{6.24}$$

where  $\delta A(\varepsilon)$  is small. The conditions that  $S(\varepsilon)$  be unitary, symmetric, and particle-hole symmetric imply

$$\delta A(\varepsilon) = \delta A(\varepsilon)^\dagger = \tau_x \delta A(\varepsilon)^T \tau_x = -\tau_z \delta A(-\varepsilon) \tau_z.\tag{6.25}$$

We therefore parameterize

$$\delta A(\varepsilon) = \begin{pmatrix} \delta\eta(\varepsilon) & \delta r(\varepsilon) \\ \delta r(\varepsilon)^* & \delta\eta(\varepsilon) \end{pmatrix},\tag{6.26}$$

where  $\delta r(\varepsilon)$  is a complex, symmetric function of energy  $\varepsilon$ , which represents disorder-induced normal reflection, whereas  $\delta\eta(\varepsilon)$  is a real, antisymmetric function of  $\varepsilon$ , which represents a disorder-induced shift of the Andreev reflection phase  $\eta(\varepsilon)$ .

As discussed above, the solution of the BdG equation for  $r < r_0$  yields two additional relations between the amplitudes  $a_{e,\pm}$  and  $a_{h,\pm}$ ,

$$a_{e,+} = e^{2i\phi_\uparrow} a_{e,-}, \quad a_{h,-} = e^{-2i\phi_\downarrow} a_{h,+}. \quad (6.27)$$

Note that in Eq. (6.27), we assumed that the size of the magnetic impurity is small compared to the coherence length, corresponding to  $k_F \xi_0 \gg 1$ . By taking this limit we can neglect scattering from electrons to holes at the position of the impurity.

A nontrivial solution of Eqs. (6.22) and (6.27) exists if

$$\det \left[ \begin{pmatrix} e^{2i\phi_\uparrow} & 0 \\ 0 & e^{-2i\phi_\downarrow} \end{pmatrix} S(\varepsilon) - \begin{pmatrix} 1 & 0 \\ 0 & 1 \end{pmatrix} \right] = 0. \quad (6.28)$$

This gives

$$\begin{aligned} \varepsilon &= \varepsilon_0 + \delta\varepsilon, \\ \delta\varepsilon &= \frac{\xi_0 \Delta}{\xi_{\varepsilon_0}} \left[ \delta\eta(\varepsilon_0) + \text{Re} e^{-i(\phi_\uparrow + \phi_\downarrow)} \delta r(\varepsilon_0) \right], \end{aligned} \quad (6.29)$$

to lowest order in  $\delta A$ . This equation is central to our analysis, since it allows us to calculate the energy shift  $\delta\varepsilon$  from the scattering matrix  $S$ .

### 6.3.2. Qualitative discussion

Next, we employ a semiclassical picture to qualitatively discuss why both  $\delta\eta$  and  $\delta r$  are expected to be small. Within this semiclassical picture, Andreev reflection is retroreflection, *i.e.*, after Andreev reflection a hole retraces the path of the incident electron (or vice versa). Because the phases of electron and hole wavefunctions are correlated, see, *e.g.*, Eq. (6.5), no net phase is accumulated, with the exception of the Andreev phase  $\eta(\varepsilon)$ . If  $k_F \ell \gg 1$  this semiclassical picture remains valid in the presence of a disorder potential  $U(\mathbf{r})$ . This explains why  $\delta\eta$ , corresponding to a shift of the Andreev phase, is small if  $k_F \ell \gg 1$ .

In fact, since  $\delta\eta(\varepsilon)$  is an antisymmetric function of  $\varepsilon$ , one must have  $\delta\eta(0) = 0$ , so that there is no contribution to the YSR-state energy shift from the phase shift  $\delta\eta$  for YSR states with energy near the center of the superconducting gap. Instead, for small YSR-state energies, the residual disorder-induced fluctuations are dominated by the normal reflection amplitude  $\delta r$ . An estimate of the size of the YSR-energy fluctuations can be obtained by estimating  $\delta r$  as the amplitude that a particle returns to the origin  $\mathbf{r} = 0$  (up to a distance  $1/k_F$ ) within a time  $\xi_\varepsilon/v_F$ . In the two-dimensional case we then find for the dirty superconductor limit  $\xi_0 \gg \ell$

$$\begin{aligned} |\delta r(\varepsilon)|^2 &\sim \int_{\lambda/v_F}^{\ell/v_F} dt \frac{1}{k_F \ell t} + \int_{\ell/v_F}^{\xi_\varepsilon/v_F} dt \frac{2}{k_F \ell t} \\ &\sim \frac{1}{k_F \ell} \log(k_F \xi_\varepsilon^2 / \ell). \end{aligned} \quad (6.30)$$

The first integral covers ballistic propagation times  $t \lesssim \tau$  and the second diffusive times  $t \gtrsim \tau$ , where  $\tau = \ell/v_F$  is the elastic mean free time. The integrands give the return

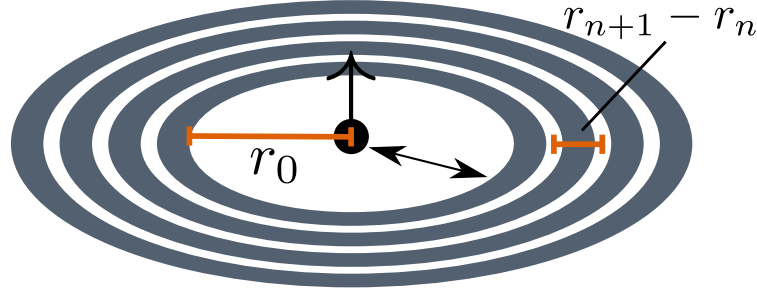


Figure 6.2.: Sketch of the numerical concatenation method in two dimensions. The disordered superconductor is cut into thin circular slices (dark gray), with infinitesimally-thin-disorder-free metallic shells (white) in between the dark gray slices and for  $r < r_0$ . The scattering matrices of the slices are calculated in the narrow limit and concatenated into the full scattering matrix  $S(\varepsilon)$ , which describes the reflection of spherical symmetric waves (black arrows) that are propagating from the magnetic impurity into the bulk.

probabilities per unit time, which, in the diffusive regime, is multiplied by a factor two due to coherent backscattering. In the second line the short-distance cutoff  $\lambda$  was replaced by  $1/k_F$ . In the ultraclean limit  $\xi_0 \ll \ell$  the second term in Eq. (6.30) is absent and the upper integration limit in the first is  $\xi_\varepsilon$ , which gives

$$|\delta r(\varepsilon)|^2 \sim \frac{1}{k_F \ell} \log(k_F \xi_\varepsilon) \quad (6.31)$$

In three dimensions, the return probability is dominated by the ballistic regime  $t \lesssim \tau$  and one finds

$$|\delta r(\varepsilon)|^2 \sim \int_{\lambda/v_F}^{\tau} dt \frac{1}{k_F^2 \ell v_F t^2} \sim \frac{1}{k_F \ell}. \quad (6.32)$$

In three dimensions, the estimate is consistent with the smallness of the first-order perturbation theory results of Sec. 6.2. In two dimensions and in the dirty limit, multiple scattering changes the argument of the logarithm in Eq. (6.30) by a factor  $\xi_\varepsilon/\ell$  compared to the perturbative result (6.17).

### 6.3.3. Numerical calculation of the scattering matrix

Our strategy for an efficient numerical calculation is a generalization of the thin-slice concatenation method for linear geometries, which we discussed in Sec. 3.3. It can be outlined as follows. First, we slice the superconductor into thin circular ( $d = 2$ ) or spherical ( $d = 3$ ) pieces, as illustrated in Fig. (6.2), and calculate the scattering matrix for each piece. Next, we add the pieces together by concatenating their scattering matrices to obtain the total scattering matrix  $S(\varepsilon)$ . Finally, using Eqs. (6.24) and (6.29) we can relate this scattering matrix to the energy of the YSR state.

Note that within this approach, we need to include non-zero angular momentum channels due to two reasons. First, disorder breaks rotational symmetry and thus mixes different angular momentum modes. Second, the modes defined in Eq. (6.21) describe all propagation modes at radii  $k_F r \lesssim 1$ . There, non-zero angular momentum modes are evanescent. This can be seen by considering the spherical representation of the momentum operator, which results in a repulsive potential that diverges  $\sim 1/r^2$  at the origin for all modes but the zero angular momentum one. However, when going to larger radii non-zero angular momentum modes start to propagate and thus cannot be excluded.

Our approach starts, by formally inserting a sequence of  $N + 1$  infinitesimally thin ideal shells into the disordered superconductor at radii  $r_n$ ,  $n = 0, 1, \dots, N$ . Within these shells the superconducting order parameter  $\Delta$  and the impurity potential  $U(\mathbf{r})$  are zero. The distance between the shells is  $r_{n+1} - r_n \ll \ell$ . In each shell the wavefunction can be expanded as [compare with Eq. (6.19)]

$$\psi(\mathbf{r}) = \sum_{\nu} a_{\nu}^{(n)} \Phi_{\nu}(\mathbf{r}), \quad (6.33)$$

where  $\nu$  is a composite index representing particle/hole degrees of freedom (e or h), propagation direction (radially outward, +, or inward, -), and the angular momentum label  $m$  (in two dimensions) or the angular momentum labels  $l, m$  (in three dimensions).

The flux-normalized basis functions  $\Phi_{\nu}$  are

$$\begin{aligned} \Phi_{e,m\pm}(\mathbf{r}) &= \sqrt{\frac{k_F}{4v_F}} H_m^{\pm}(k_F r) e^{im\varphi} \begin{pmatrix} 1 \\ 0 \end{pmatrix}, \\ \Phi_{h,m\pm}(\mathbf{r}) &= \sqrt{\frac{k_F}{4v_F}} H_m^{\mp}(k_F r) e^{im\varphi} \begin{pmatrix} 0 \\ 1 \end{pmatrix} \end{aligned} \quad (6.34)$$

in two dimensions and

$$\begin{aligned} \Phi_{e,lm\pm}(\mathbf{r}) &= \sqrt{\frac{k_F^2}{4\pi v_F}} h_l^{\pm}(k_F r) Y_{lm}(\theta, \varphi) \begin{pmatrix} 1 \\ 0 \end{pmatrix}, \\ \Phi_{h,lm\pm}(\mathbf{r}) &= \sqrt{\frac{k_F^2}{4\pi v_F}} h_l^{\mp}(k_F r) Y_{lm}(\theta, \varphi) \begin{pmatrix} 0 \\ 1 \end{pmatrix} \end{aligned} \quad (6.35)$$

in three dimensions, where the  $Y_{lm}(\theta, \phi)$  are spherical harmonics and the  $H_m$  ( $h_l^{\pm}$ ) are (spherical) Hankel functions. The solution of the BdG equation for  $r_n < r < r_{n+1}$  gives a linear relationship between the coefficients  $a^{(n)}$  and  $a^{(n+1)}$ , which has the form (vector notation is implied for all indices not listed explicitly)

$$\begin{pmatrix} a_{-}^{(n)} \\ a_{+}^{(n+1)} \end{pmatrix} = \mathcal{S}^{(n)}(\varepsilon) \begin{pmatrix} a_{-}^{(n+1)} \\ a_{+}^{(n)} \end{pmatrix} \quad (6.36)$$

where  $\mathcal{S}^{(n)}(\varepsilon)$  is the scattering matrix between the shells at  $r_n$  and  $r_{n+1}$ .

If  $r_{n+1} - r_n$  is much smaller than the mean free path  $\ell$ , the scattering matrix  $\mathcal{S}^{(n)}(\varepsilon)$  can be calculated using the unitarized Born approximation introduced in Sec. 3.3,

$$\mathcal{S}^{(n)} = [\mathbf{1} - i\mathcal{T}^{(n)}/2][\mathbf{1} + i\mathcal{T}^{(n)}/2]^{-1}, \quad (6.37)$$

with

$$\mathcal{T}_{\nu'\nu}^{(n)} = \int_{r_n < r < r_{n+1}} d\mathbf{r} \quad \psi_{\nu'}^\dagger(\mathbf{r}) H'_\varepsilon(\mathbf{r}) \psi_\nu(\mathbf{r}), \quad (6.38)$$

with  $H'_\varepsilon(\mathbf{r}) = \Delta\tau_x + U(\mathbf{r})\tau_z - \varepsilon$ . We refer to the Appendix. C for explicit expressions for the matrices  $\mathcal{T}^{(n)}$ .

To truncate the hierarchy of Eqs. (6.36) we set the disorder potential  $U(\mathbf{r})$  to zero for  $r > r_N$ , which gives the relation

$$a_-^{(N)} = e^{-i\eta(\varepsilon)} \tau_x a_+^{(N)}. \quad (6.39)$$

Further, for nonzero angular momentum indices  $m$  or  $l$  the Hankel functions  $H_m$  and  $h_l$  diverge for  $k_F r \lesssim \pi|m|/2$ ,  $k_F r \lesssim \pi l/2$ , respectively. In that case regularity of  $|\psi(\mathbf{r})\rangle$  imposes that the corresponding coefficients  $a_+^{(n)}$  and  $a_-^{(n)}$  must be equal. In particular, we have

$$a_{e,+}^{(0)} = a_{e,-}^{(0)}, \quad a_{h,+}^{(0)} = a_{h,-}^{(0)} \quad (6.40)$$

for all  $m \neq 0$  ( $d = 2$ ) or  $l > 0$  ( $d = 3$ ). Similarly, this observation allows us to truncate the sum over modes  $l$  and  $m$  to the number of propagating angular momentum modes at the largest distance required for the calculation of  $S(\varepsilon)$ , which is  $r \sim \xi_\varepsilon$ .

Combining Eqs. (6.36), (6.39), and (6.40) we can eliminate all amplitudes  $a^{(n)}$  with  $n \geq 1$  and calculate the scattering matrix  $S(\varepsilon)$  describing the (Andreev) reflection of radially outgoing waves at the origin. The procedure becomes numerically exact in the limit  $r_{n+1} - r_n \rightarrow 0$ ,  $r_N \rightarrow \infty$ . In practice, to achieve convergence it is sufficient that  $r_{n+1} - r_n \lesssim \ell$  and if  $r_N \sim \xi_\varepsilon$  because of the exponential decay of the wavefunction in the superconductor. In the numerical simulations, the short-distance cutoff is fixed to  $r_0 = 0$  in two and  $r_0 = 1/k_F$  in three dimensions.

Figure 6.3 shows examples of the convergence behaviors in two and three dimensions. In two dimensions the numerical scattering matrix calculation converges slowly, in agreement with results from perturbation theory which predicts a logarithmic convergence at a length scale of the order of the coherence length. In contrast, our numerical results for three dimensional systems converge after a few Fermi wavelengths  $2\pi/k_F$  and also agree well with our results derived by perturbation theory.

In Fig. 6.4 we show the variance of the YSR energy for two dimensions. The numerical results confirm that the fluctuations become small in the limit of large  $k_F \ell$ , while keeping  $\ell/\xi_\varepsilon$  constant, quantitatively consistent with the result of lowest-order perturbation theory in the disorder potential  $U(\mathbf{r})$ . Logarithmic corrections to the perturbative results are expected to occur deep in the dirty limit, see Eq. (6.30).

For comparison with the numerical results in three dimensions, we have repeated the perturbative calculation of Sec. 6.2 with the disorder potential set to zero for  $r < r_0 = 1/k_F$ . In this case we find

$$\begin{aligned} \langle \delta\varepsilon^2 \rangle &= \frac{\Delta^2 (\xi_0/\xi_{\varepsilon_0})^4}{k_F \ell} \\ &\times \left( c_0 + \frac{c_1 - 2 \log(k_F \xi_\varepsilon)}{k_F \xi_\varepsilon} - \frac{c_3 + c_4 \cos \eta}{k_F^2 \xi_\varepsilon^2} + \dots \right) \end{aligned} \quad (6.41)$$

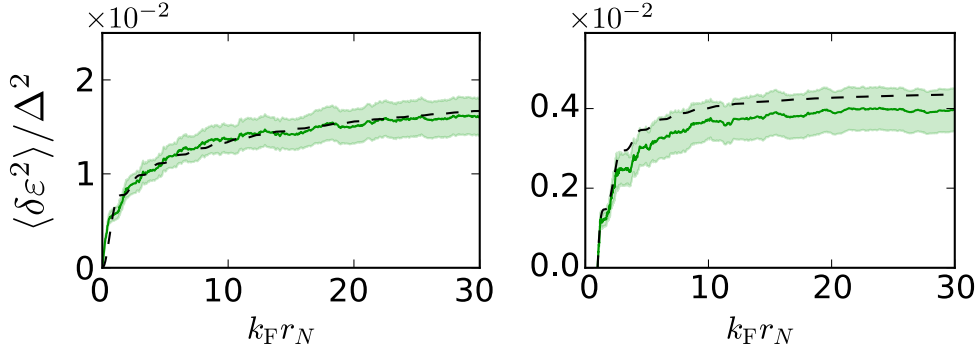


Figure 6.3.: YSR energy shift (solid lines) versus disorder cutoff length  $r_N$  in two dimensions (left panel) and three dimensions (right panel), obtained from the numerical scattering approach. We choose  $\xi/\ell = 10$  with  $k_F\ell = 100$ . When including the cutoff  $r_N$ , our perturbative approach (dashed lines) fits well with the numerical results. The shaded region shows the numerical standard error. Figure taken from Ref. [Kien 17] (doi). ©2017 American Physical Society.

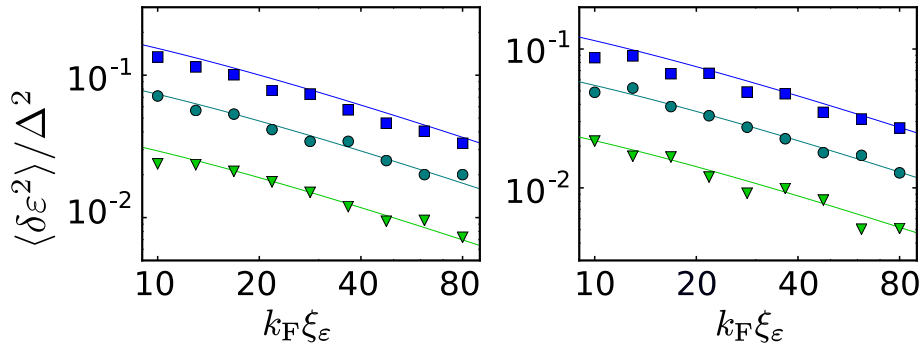


Figure 6.4.: YSR energy variance versus  $k_F \xi_\varepsilon$  in two dimensions. The data points are for  $\xi_\varepsilon/\ell = 0.5$  (triangles), 1 (circles) and 2 (squares). The scattering phase shifts  $\phi_\uparrow = -\phi_\downarrow$  are chosen such that YSR energy in the absence of disorder is  $\varepsilon/\Delta = 0$  (left) and  $\varepsilon/\Delta = 0.37$  (right). The solid lines show the lowest-order perturbation theory result from Eq. (6.17). Error bars are of the size of the markers. Figure taken from Ref. [Kien 17] (doi). ©2017 American Physical Society.

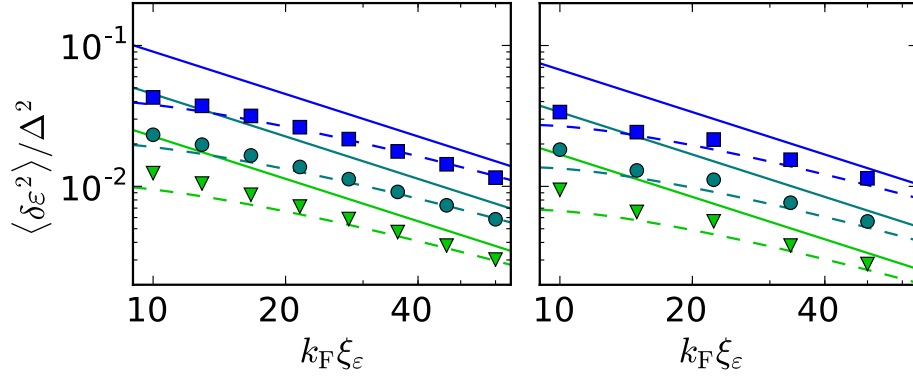


Figure 6.5.: YSR energy variance in three dimensions, as a function of  $k_F \xi_\varepsilon$  at fixed ratios  $\xi_\varepsilon/\ell$ . The parameters are the same as in Fig. 6.4. The dashed and solid curves give the perturbative result (6.41) and its leading term, respectively. Figure taken from Ref. [Kien 17] (doi). ©2017 American Physical Society.

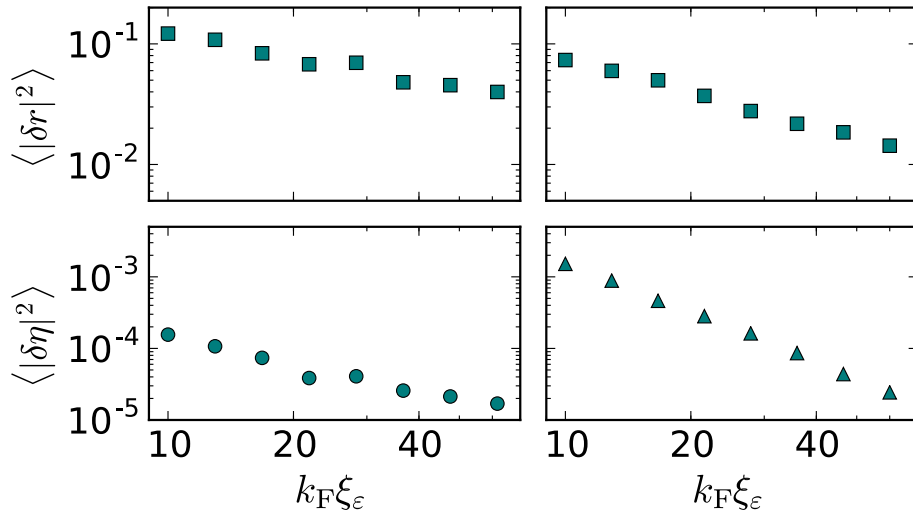


Figure 6.6.: Comparison of the two contributions  $\delta r$  and  $\delta \eta$  to the superconductor scattering matrix  $S(\varepsilon)$ , in two (left) and three (right) dimensions. See Eq. (6.26). We choose a ratio  $\xi_0/\ell = 1$  and energy  $\varepsilon/\Delta = 0.15$ . The contribution from normal reflection dominates in two as well as in three dimensions. Figure taken from Ref. [Kien 17] (doi). ©2017 American Physical Society.

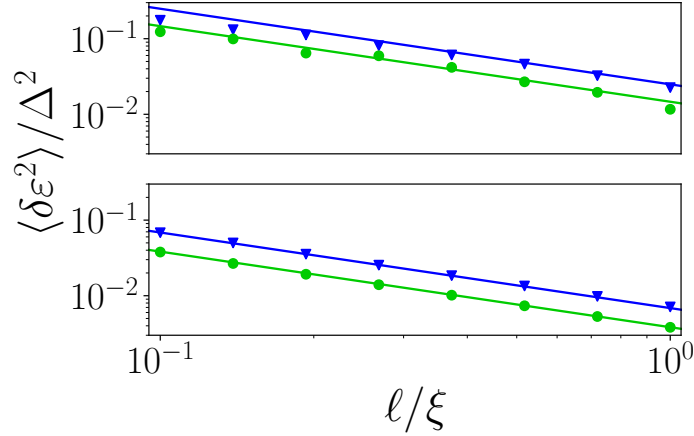


Figure 6.7.: Energy variance over mean free path at fixed  $k_F$  and  $\xi_0$ . The markers show the numerical results in two dimensions (top) and three dimensions (bottom), with  $k_F \xi_0 = 50$  (blue triangles) and  $k_F \xi_0 = 100$  (green circles). The lines correspond to the perturbative results derived in the main text. The scattering phase shifts  $\phi_\uparrow = -\phi_\downarrow$  of the magnetic impurity are chosen such that, in the absence of disorder, a YSR state forms at  $\varepsilon/\Delta = 0$ . Figure taken from Ref. [Kien 17] (doi). ©2017 American Physical Society.

to second order in  $1/k_F \xi_\varepsilon$ . The coefficients read  $c_0 \approx 0.45$ ,  $c_1 \approx 2.59$ ,  $c_3 \approx 5.87$  and  $c_4 \approx 2.71$ . To leading order this simplifies to the asymptotic form in Eq. (6.18). The agreement of the higher order result (6.41) with the numerics is excellent for all values of  $k_F \xi_\varepsilon$  considered; the leading order agrees for large values of  $k_F \xi_\varepsilon$  only, see Fig. 6.5.

Next, we present data in the dirty limit,  $\ell \lesssim \xi_0$ , and for a fixed  $\xi_0$  and  $k_F$  while varying  $\ell$ . The data is shown in Fig. 6.7 with the perturbative results taken from Eqs. (6.17) and (6.41). The energy variance is well approximated by lowest order perturbation theory in disorder. Deviations occur in two dimensions, when  $k_F \ell$  gets close to one.

Additionally, as shown in Fig. 6.3, in order for us to reach convergence in two dimensions we have to let the disorder cutoff flow to a distance far exceeding the Fermi wave length. This supplements Fig. 6.8 by a fully converged plot in the dirty limit. We note especially, that convergence requires distances of the order of multiple mean free paths and thus the final value is expected to contain contributions from multiple scattering.

Our approach also allows us to separate contributions to the YSR energy variance arising from fluctuations of the Andreev phase and normal reflection, see Eq. (6.29). The two contributions to  $\langle \delta \varepsilon^2 \rangle$  are shown in Fig. 6.6 for  $\varepsilon/\Delta = 0.15$ . The figure shows that the main contribution to  $\langle \delta \varepsilon^2 \rangle$  comes from normal reflection. This is consistent with the fact that fluctuations of the Andreev phase  $\eta(\varepsilon)$  have an additional smallness because  $\delta \eta(\varepsilon)$  is an antisymmetric function of energy.

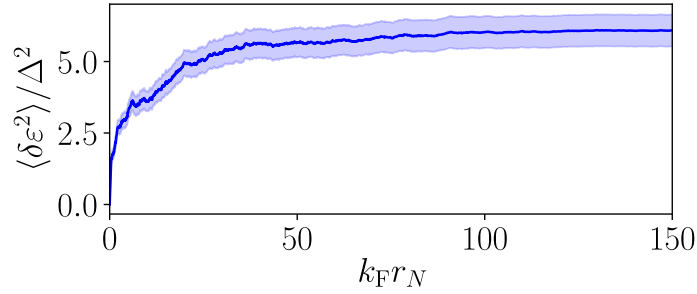


Figure 6.8.: Convergence of the energy variance with disorder cutoff  $r_N$  in the dirty limit and in two dimensions. The parameters are  $k_F \xi_0 = 300$  and  $\xi_0/\ell = 10$ , with the same magnetic impurity parameters as in Fig. 6.7. Figure taken from Ref. [Kien 17] (doi). ©2017 American Physical Society.

#### 6.4. Relation to Ref. [Hui 15]

In this section, we discuss the related Ref. [Hui 15], which reports a much stronger susceptibility of the YSR energy to disorder than we do. We attribute the difference to the two approximations made in Ref. [Hui 15].

Without disorder, the magnetic impurity contributes a delta function  $\delta(\omega - \varepsilon_0)$  to the density of states. Including and averaging over disorder, this contribution is broadened. In Ref. [Hui 15], the width of the peak in the density of states is used as a measure of the disorder-induced variance  $\langle \delta \varepsilon^2 \rangle$  of the YSR energy.

Reference [Hui 15] calculates the Green function  $G(\omega)$  in the presence of the magnetic impurity and non-magnetic disorder in the superconductor and obtains the impurity density of states from the relation

$$\rho(\omega) = -\frac{1}{\pi} \text{TrIm}\langle G(\omega) \rangle, \quad (6.42)$$

where the brackets  $\langle \dots \rangle$  refer to the disorder average. The disorder average  $\langle G(\omega) \rangle$  is then performed with two approximations. First, Ref. [Hui 15] uses the self-consistent Born approximation (SCBA), which yields a self-consistent equation for  $\langle G(\omega) \rangle$ ,

$$\langle G(\omega) \rangle = \left\{ \left[ G^{(0)}(\omega) \right]^{-1} - \Sigma(\omega) \right\}^{-1}, \quad (6.43)$$

where  $G^{(0)}(\omega)$  is the Green function without the non-magnetic disorder (but with the magnetic impurity) and

$$\Sigma_{\mathbf{k},\mathbf{k}'}(\omega) = \frac{v_F}{2\pi\nu_0\ell V} \sum_{\mathbf{p}} \tau_z \langle G_{\mathbf{p}+\mathbf{k},\mathbf{p}+\mathbf{k}'}(\omega) \rangle \tau_z \quad (6.44)$$

is the SCBA self energy (other symbols are defined in Sec. 6.1).

The second approximation in Ref. [Hui 15] is based on the following argument. The main contribution of the summation in the self energy is from momenta  $\mathbf{p} + \mathbf{k}$  and  $\mathbf{p} +$

$\mathbf{k}'$  at the Fermi-level. Hence, approximately, one can restrict the summation over  $\mathbf{p}$  to the manifold defined by  $|\mathbf{p} + \mathbf{k}| = |\mathbf{p} + \mathbf{k}'| = k_F$ . If  $\mathbf{k} \neq \mathbf{k}'$ , these are two independent equations and hence the manifold has two dimensions less than the dimension of  $\mathbf{p}$ . If however  $\mathbf{k} = \mathbf{k}'$ , there is only one constraint and the dimension of the manifold is only one less than the dimension of  $\mathbf{p}$ . From this, the authors of Ref. [Hui 15] concluded that the self energy can be approximated to be diagonal and that it reads

$$\Sigma_{\mathbf{k},\mathbf{k}'} \approx \frac{v_F}{2\pi\nu_0\ell V} \delta_{\mathbf{k},\mathbf{k}'} \sum_{\mathbf{p},\mathbf{q}} \tau_z \langle G_{\mathbf{p},\mathbf{q}} \rangle \tau_z. \quad (6.45)$$

To facilitate the comparison with our own results, we first reformulate these in Green function language. In the limit  $k_F\ell \gg k_F\xi_0 \gg 1$  the YSR state is separated from other states by a finite gap. Hence, only the lowest order contributions in disorder are expected to contribute to a shift in the YSR energy and to a good (controlled) approximation, we can rewrite the low-energy part of Hamiltonian (6.5) as

$$H = (\varepsilon_0 + U_{0,0}) |0\rangle \langle 0|. \quad (6.46)$$

Here,  $|0\rangle$  is the YSR-state derived in the main text, with its wavefunction given by Eq. (6.5). The disorder matrix-element  $U_{0,0} = \langle 0|U(\mathbf{r})\tau_z|0\rangle$  has a Gaussian distribution with zero average and a variance  $\langle U_{0,0}^2 \rangle = \langle \delta\varepsilon^2 \rangle$ , where the latter was derived in Eqs. (6.17) and (6.18) in the main text. Note that, due to particle-hole symmetry being present in the physical problem, there is also a YSR state at  $-\varepsilon_0$ . However, this second state lives in a disjunct sector of the Hilbert space and hence it is sufficient to consider only one of the two states when calculating the spectrum.

The Green function is easily obtained and, within the YSR-state subspace, reads

$$G(\omega) = \frac{1}{\omega - \varepsilon_0 - U_{0,0} + i\eta} \quad (6.47)$$

with  $\eta \downarrow 0$ . The average density of states reads

$$\rho(\omega) = \frac{1}{\sqrt{2\pi\langle\delta\varepsilon^2\rangle}} e^{-(\omega-\varepsilon_0)^2/2\langle\delta\varepsilon^2\rangle}, \quad (6.48)$$

in exact quantitative agreement with the perturbation theory of Sec. 6.2.

We now investigate the effect of the first approximation in [Hui 15]. For the low-energy Hamiltonian (6.46) the expression for the SCBA self energy reads

$$\Sigma(\omega) = \langle \delta\varepsilon^2 \rangle \langle G(\omega) \rangle. \quad (6.49)$$

Solving Eqs. (6.43) and (6.49) one finds

$$\rho(\omega) = \begin{cases} \frac{\sqrt{4\langle\delta\varepsilon^2\rangle - (\omega-\varepsilon_0)^2}}{2\pi\langle\delta\varepsilon^2\rangle} & \text{for } (\omega - \varepsilon_0)^2 < 4\langle\delta\varepsilon^2\rangle, \\ 0 & \text{else.} \end{cases} \quad (6.50)$$

This result disagrees qualitatively from the exact result (6.48), although the order-of-magnitude of the width of the density of states peak is still correct.

The second approximation relies on the assumption that  $\Sigma(\omega)$  and  $\langle G(\omega) \rangle$  are diagonal in momentum space. The latter assumption is clearly questionable, since the presence of the magnetic impurity causes the Green function to be non-diagonal in momentum space. In contrast, replacing the single sum in Eq. (6.44) by the double sum in Eq. (6.45) assumes a diagonal Green function. Taking the double sum greatly increases the impurity contribution to the diagonal part of  $\Sigma(\omega)$ , whereas the approximation (6.45) ignores any impurity-induced off-diagonal contribution to  $\Sigma(\omega)$ . With this second approximation, the momentum sums can be replaced by energy integrations. In this step, the dependence on  $k_F \ell$  as well as system dimensionality drops out, leaving a dependence on the ratio  $\ell/\xi_0$  only, a feature that clearly contradicts the direct perturbative solution (6.48) in the weak-disorder limit  $\xi_0 \ll \ell$ .

To conclude, while both approximation made in Ref. [Hui 15] are uncontrolled, we believe it is the second approximation that is responsible for the stark qualitative difference between that reference and the present results.

## 6.5. Conclusion

In this chapter, we have analyzed the variance of the YSR energy due to nonmagnetic disorder in both two and three dimensions. Mapping this problem to a scattering ansatz for electrons and holes close to the magnetic impurity allowed us to reduce the effects of nonmagnetic disorder to two separate contributions.

First, the Andreev phase, which is picked up when an electron is Andreev reflected as a hole or vice versa, starts fluctuating as a function of disorder configuration. Using time reversal and particle hole symmetry, we have argued that this contribution is expected to be negligible in the limit  $k_F \ell, k_F \xi_\epsilon \gg 1$ . Numerical calculations confirmed this prediction.

Second, disorder can flip the momentum and lead to a finite normal reflection amplitude for electrons or holes propagating from the impurity into the superconductor. We find that the normal reflection probability is small if  $k_F \ell \gg \log[k_F \xi_\epsilon \max(1, \xi_\epsilon/\ell)]$  and  $k_F \ell \gg 1$  in two and three dimensions, respectively. Importantly YSR states can be robust to disorder even in the limit of a dirty superconductor.

Finally, we found that in three dimensions only disorder within a few Fermi wavelengths of the magnetic impurity contributes to the YSR energy variance. This is in contrast to two dimensions, where disorder from distances up to the coherence length contributes.

Our results relax earlier claims [Hui 15], which suggested that at  $\ell$  of the order of  $\xi_0$  the width of YSR energy distribution becomes of the order of the superconducting gap. Our findings show that  $\lambda_F$  is a crucial parameter to be included into the discussion and that this typically leads to a negligible influence of disorder.

Our findings also have implications for one dimensional topological superconductors, that are formed by dilute classical adatom chains. These systems can be described by effective tight-binding models [Pien 15]. (Note, however, that current experiments may well be in a rather different limit in which the hybridization of the adatom d levels plays an important role [Nadj 14, Ruby 15a, Pawl 16, Feld 17, Ruby 17].) The on-site energies in these models are immune to disorder, if the conditions are met that we derived in this chapter for the single Shiba states. This leaves the discussion of the tunneling and pairing

strengths. If the distance  $d$  between the impurities is small compared to  $\ell$ , we expect the influence of disorder on the nearest neighbor hopping and pairing terms to be suppressed by a factor  $d/\ell \sim 1/k_F\ell$ . However, previous studies have shown [Pien 13, Pien 14b], that in a clean system with  $k_F\xi_0 \gg k_Fd \gg 1$ , tunneling is following a long-range,  $1/r$  power law. Thus, strictly speaking, more than nearest-neighbor terms have to be included. If the length of the chain is smaller than the mean free path, the same arguments as for the nearest-neighbor elements apply. For longer chains, further work is required to investigate the influence of disorder on long range tunneling and pairing elements.



## 7. Conclusion

In this thesis, we study low-energy excitations in strongly-coupled superconductor-magnet hybrids. We employ analytical and numerical methods of scattering theory to infer properties of the systems of interest. Much of the motivation of this thesis originates from the goal of realizing a robust phase of topological superconductivity and observing Majorana bound states in quasi-one dimensional systems.

In Chapter 2, we place this thesis into context. We review the theoretical progress that lead to the prediction of topological superconductivity and Majorana bound states in condensed matter systems, and investigate a model for weakly-coupled superconductor-magnet hybrids with a translationally invariant bulk. For this model, we define a topological index and argue based on bulk-boundary correspondence that MBS appear when two systems with a different topological index are connected. We finish our review by discussing two experimental realizations of topological superconductivity that gained much attention in the current decade. These are semiconductor nanowires coupled to an  $s$ -wave superconductor and placed inside a magnetic field, and adatom chains placed on top of an  $s$ -wave superconductor. While signatures of Majorana bound states have been observed in both of these systems, and the quality of these observations has been greatly improved over the past years, these signatures remain ambiguous and it is still contentious whether these experiments really observed Majorana bound states.

In the second part of chapter 2, we review another type of superconductor-magnet heterostructure, a single magnetic impurity coupled to an  $s$ -wave superconductor. For sufficiently strong coupling, it has been predicted that YSR states appear deep inside the bulk superconductor's gap and localized to the magnetic impurity. Besides the possibility to couple multiple YSR states in order to realize a topological superconductor [Nadj 13, Pien 13], isolated YSR states have intriguing properties by themselves and effort is being put into better understanding these properties. Examples include the sudden change of the electronic ground state from having total spin zero to total spin one when the YSR energy crosses zero, the asymmetry of the particle and hole components of the YSR state, and the appearance of multiple YSR states due to the coupling to different orbitals of the magnetic impurity. Progress in control, fabrication and measurement techniques made it possible to observe these states routinely in experiment, to verify theoretical predictions, as well as to uncover new facets of YSR states [Yazd 97, Ji 08, Ji 10, Fran 11, Ruby 15b, Mena 15, Hatt 15, Ruby 16, Choi 17, Hatt 17, Ruby 18, Fari 18, Kezi 18].

In chapter 3, we introduce the basic concepts of scattering theory used in this thesis, based on the central concept of the  $S$ -matrix. We then apply scattering theory to the extensively studied models of a wire with either a  $s$ -wave or a  $p$ -wave pairing potential, where the later corresponds to a continuum version of the Kitaev chain [Kita 01], and show that only for the  $p$ -wave case a bound state appears at the boundary, and that this bound state is of Majorana type. Furthermore, we review a concatenation method

that is used extensively in the later chapters and was previously applied in a variety of contexts. It allows one to calculate the  $S$ -matrix of an elongated region by concatenating the  $S$ -matrices of thin-slices of this elongated scattering region. This has the advantage that one can perturbatively calculate the scattering matrix of the thin-slices and use a concatenation prescription to obtain the  $S$ -matrix of the elongated scattering region.

Chapter 4 studies the low-energy excitations of a spin-polarized metallic wire that is coupled to an  $s$ -wave superconductor, with spin-orbit coupling in either of the materials. On the one hand, in the limit of weak coupling between superconductor and wire, this model has been studied previously [Duck 11]. The low-energy excitations can be described by the large- $B$  limit of the weak-coupling model introduced in Sec. 2.1.2, and thus the model realizes a topological superconductor. On the other hand, previous studies have shown that strong coupling between a superconductor and adatom chains or semiconductor nanowires leads to a renormalization of the properties of the topological phase, such as the quasiparticle velocity, Majorana localization length and induced gap [Peng 15, Das 15, Stic 17, Stan 17].

In this thesis, we investigate these renormalization effects from the point of view of scattering theory in the case of coupling to either a two- and a three dimensional superconductor. Our approach allows us to trace the renormalization of the quasiparticle velocity back to Andreev processes that lead to zero net-displacement along the wire. In the low-transparency limit, these predictions differ from a purely classical derivation due to a  $\pi$  phase-shift that is picked up when quasiparticles are Andreev reflected twice. Furthermore, as a function of interface transparency, our analysis yields the power law dependencies of the induced gap, the localization length, and the velocity in the regimes of very small and intermediate transparencies, and allows us to calculate the same quantities numerically at arbitrary transparencies. We find that large transparencies generically lead to a large induced gap and a small localization length, compared to very small transparencies. For intermediate transparencies, the induced gap is renormalized by the same factor as the velocity, while we find no such renormalization for the localization length of the Majorana bound state. Upon comparing these results with a previously employed Green function approach that accounts for the strong coupling to the superconductor by a local, energy-dependent self-energy, we find good qualitative agreement with our results [Peng 15]. Furthermore, our approach gives a semiclassical understanding of the locality of the self energy in terms of zero net-displacement scattering processes.

Recent experiments on Majorana wires use semiconductor nanowires coupled to thin superconducting coats. These thin coats have a thickness much smaller than the expected coherence length of the superconducting condensate [Chan 15, Deng 16, Albr 16, Zhan 18]. On the one hand, the small thickness reduces the size of the experimental setup, leads to a small magnetic flux through the superconductor for fields parallel to the wire, allows for relatively pristine interfaces with semiconductor nanowires, and has been found to induce a hard gap in the proximitized wire [Krog 15, Chan 15]. On the other hand, it has been suggested that finite size effects play a role and can be detrimental for the induced gap [Reeg 17]. These finite size effects originate in the small thickness of the superconductor compared to its coherence length, and one may pose the question which effects could be included in order to reverse these detrimental effects.

In chapter 5, we investigate the low-energy spectrum of such a normal metal coupled to

---

a thin two- or three-dimensional superconducting coat with disorder present in the bulk or the exposed surface of the superconductor. Based on a semiclassical approximation, we argue that the induced gap is small in the absence of disorder and for typical experimental parameters, even when the interface transparency becomes of order unity. The induced gap is suppressed in the ratio of normal-metal to superconductor thickness. Within our semiclassical approximation and for approximately matching Fermi velocities in the normal metal and superconductor, we argue that this suppression can be lifted by the presence of disorder in the bulk or at the exposed surface of the superconductor. Notably, for a large coherence length compared to the normal-metal thickness, we predict that a mean free path larger than the superconductor thickness is sufficient to enhance the gap towards values close to the bulk gap of the superconductor. These findings are in qualitative agreement with the observation of large induced gaps in recent experiments [Krog 15, Chan 15, Deng 16, Albr 16, Zhan 18], as well as with the results of other theoretical studies that report an enhanced gap due to surface disorder [Reeg 18a].

We back up our prediction by two methods. First, in the absence of disorder, we derive an effective low-energy Hamiltonian in the basis of the normal-state wavefunctions and obtain its low-energy spectrum. These results show good agreement with results obtained within our semiclassical approximation, as well as with previous results from the literature [Reeg 17]. Furthermore, we employ the scattering approach discussed in Sec. 3.3 in order to numerically calculate the low-energy density of states for the full model-Hamiltonian, including disorder effects. Again, our results show good agreements with our semi-classical results for weak-disorder. For large disorder-strengths, deviations occur that we attribute to the onset of Anderson localization.

In chapter 4, we consider the renormalization processes in the case of a superconductor with a thickness large compared to its coherence length, and find that the renormalization of the velocity can be traced back to consecutive Andreev reflection processes that generate zero net-displacement along the wire. Our discussion in chapter 5 begs the question, on whether such renormalization processes are also present in the case of thin superconducting coats that have a sufficiently small mean free path. Our qualitative arguments in chapter 4 relied on processes, where an electron that enters the superconductor is retroreflected as a time-reversed hole with opposite spin. Because Andreev reflection for a time-reversal symmetric superconductor is retroreflection between electrons and holes that are time-reversed partners, these processes also occur if transport inside the superconductor is diffusive due to scattering for example from the surface. Hence, we believe that processes that lead to zero-net displacement are also present in the case of thin superconducting coats, and we expect the presence of renormalization effects similar to those in chapter 4.

Finally, chapter 6 turns from wire-superconductor hybrids to point-like magnetic scatterers coupled to a superconductor and investigates the influence of non-magnetic disorder on the energy of YSR states. Our model considers the case of a magnetic impurity embedded in either a two- or three dimensional superconductor, and the extension of the superconductor is assumed to be large compared to the coherence length in the superconductor. We tackle this problem by calculating the variance of the YSR energy using a perturbative, a semiclassical, and a non-perturbative numerical ansatz. For three dimensions, we find that the energy variance is small in the product of mean free path and Fermi wavenumber. In two dimensions, the energy variance has the same dependence on

the mean free path, but is larger by a logarithmic factor that depends on the coherence length. Our analysis shows that this difference arises from the fact that for three dimensions only weak disorder within a few Fermi-wave lengths around the magnetic impurity contributes to the energy variance. Our results show that the spectral properties of YSR states have a strong robustness to disorder, even for moderate amounts of disorder, and relax findings of a previous study that found a strong susceptibility to disorder once the mean free path becomes small compared to the coherence length [Hui 15].

In conclusion, this thesis discusses superconductor-magnet hybrids of various geometries, with a focus on the strong coupling regime between both materials. Much attention is paid to the relation with current developments towards realizing robust phases of topological superconductivity. While many research paths can be followed that use a topological superconductor as a basic building block, in this thesis we commit ourselves to improving the basic understanding of the building block itself, as well as related hybrid structures. Throughout this thesis we use scattering theory as a tool to achieve this understanding and aim at reducing effects to basic scattering processes. For example, in chapter 4 we have shown that the renormalization of the quasiparticle velocity can be traced back to successive Andreev reflections that create zero net-displacement along the wire, chapter 5 shows how to deduce the gap induced by a thin superconductor from basic scattering processes within a semiclassical approximation, and in chapter 6, we related the variance of the YSR energy to scattering processes reminiscent of those of a random walk.

# Appendix



## A. Scattering matrix and born approximation

In this chapter, we give a derivation of the scattering matrix in a more general context than that of chapter 3, and derive the Born approximation, which is used at several occasions in this thesis. The contents of this chapter are not new and have been covered in the literature before in many places, see for example Refs. [Lipp 50, Saku 94, Thom 15].

To start, consider the Hamiltonian

$$\hat{H}(t) = \hat{H}_0 + \hat{V}e^{-\eta|t|} \quad (\text{A.1})$$

where we call  $\hat{H}_0$  the free Hamiltonian with the complete set of free solutions

$$\varepsilon |\phi_\alpha(\varepsilon)\rangle = \hat{H}_0 |\phi_\alpha(\varepsilon)\rangle, \quad (\text{A.2})$$

normalized to

$$\langle \phi_\alpha(\varepsilon) | \phi_\beta(\varepsilon') \rangle = 2\pi\hbar\delta(\varepsilon - \varepsilon')\delta_{\alpha\beta}, \quad (\text{A.3})$$

and  $\hat{V}$  is scattering potential that is slowly turned on and off at a rate  $\eta \rightarrow 0$ . In a typical scattering problem we take an initial state  $|\phi_\alpha\rangle$  at  $t \rightarrow -\infty$ , let it scatter from  $\hat{V}$ , and asks: What are the scattering amplitudes  $S_{\beta\alpha}$  into the final states  $|\phi_\beta\rangle$  at  $t \rightarrow \infty$ ? The matrix  $S_{\beta\alpha}$  is called the S-matrix or scattering matrix.

More formally, we define the retarded and advanced wave functions  $|\psi^R(t, \varepsilon)\rangle$  and  $|\psi^A(t, \varepsilon)\rangle$  that solve the time-dependent Schrödinger equation

$$i\hbar\partial_t |\psi_\alpha^{R/A}(t, \varepsilon)\rangle = \hat{H}(t) |\psi_\alpha^{R/A}(t, \varepsilon)\rangle, \quad (\text{A.4})$$

such that

$$\lim_{t \rightarrow \mp\infty} |\psi_\alpha^{R/A}(t, \varepsilon)\rangle = \lim_{t \rightarrow \mp\infty} e^{-i\varepsilon t} |\phi_\alpha(\varepsilon)\rangle. \quad (\text{A.5})$$

That is, the retarded solution is the forward propagation of the initial state  $|\phi_\alpha(\varepsilon)\rangle$  from  $t \rightarrow -\infty$  to a finite time, and the advanced solution is the backward propagation of the final state from  $t \rightarrow \infty$  to a finite time.

In terms of the retarded wavefunctions, we then define the scattering amplitudes via the expansion

$$\lim_{t \rightarrow \infty} |\psi_\alpha^R(t, \varepsilon)\rangle = \lim_{t \rightarrow \infty} \sum_{\beta} S_{\beta\alpha}(\varepsilon) e^{-i\varepsilon t} |\phi_\beta(\varepsilon)\rangle. \quad (\text{A.6})$$

Next, we transform Eq. (A.6) into a more accessible form. First, we apply the bra  $\lim_{t \rightarrow \infty} \langle \phi_\beta(\varepsilon') | e^{i\varepsilon' t}$  to Eq. (A.6) and obtain

$$S_{\beta\alpha}(\varepsilon) 2\pi\hbar\delta(\varepsilon' - \varepsilon) = \langle \psi_\beta^A(0, \varepsilon') | \psi_\alpha^R(0, \varepsilon) \rangle. \quad (\text{A.7})$$

Here, we kept the bracket on the left-hand side to keep the choice of normalization open and on the right-hand side we evolved the bra and ket back in time to  $t = 0$ , which leaves the bracket invariant. An implicit solution to Eq. (A.1) at  $t = 0$  and for  $\eta \rightarrow 0$  is given by the Lippmann-Schwinger equation [Lipp 50]

$$|\psi_\alpha^{R/A}(\varepsilon)\rangle = \left(1 + \frac{1}{\varepsilon - \hat{H} \pm i\eta} \hat{V}\right) |\phi_\alpha(\varepsilon)\rangle, \quad (\text{A.8})$$

where we dropped the time-argument for  $\psi_\alpha^{R/A}$ . We can use Eq. (A.8) to transform Eq. (A.7),

$$\begin{aligned} S_{\beta\alpha} 2\pi\hbar\delta(\varepsilon - \varepsilon') &= (\langle\psi_\beta^R(\varepsilon')| + \langle\psi_\beta^A(\varepsilon')| - \langle\psi_\beta^R(\varepsilon')|) |\psi_\alpha^R(\varepsilon)\rangle \\ &= 2\pi\hbar\delta(\varepsilon - \varepsilon')\delta_{\alpha\beta} + \langle\phi_\beta(\varepsilon')| \hat{V} \left( \frac{1}{\varepsilon' - \hat{H} + i\eta} - \frac{1}{\varepsilon' - \hat{H} - i\eta} \right) |\psi_\alpha^R(\varepsilon)\rangle \\ &= 2\pi\hbar\delta(\varepsilon - \varepsilon') \left( \delta_{\alpha\beta} - i \langle\phi_\beta(\varepsilon)| \hat{V} |\psi_\alpha^R(0, \varepsilon)\rangle / \hbar \right). \end{aligned} \quad (\text{A.9})$$

In principle, one can solve the Lippmann-Schwinger and then obtain the scattering matrix from Eq. (A.9). However, the former is an implicit equation and the lack of a general solution makes this a non-trivial problem.

An explicit solution for the scattering-matrix can be obtained using the lowest-order Born approximation, which evaluates Eq. (A.9) to lowest order in  $\hat{V}$ . In this case,

$$S_{\beta\alpha} = \delta_{\alpha\beta} - \frac{i}{\hbar} \langle\phi_\beta(\varepsilon)| \hat{V} |\phi_\alpha(\varepsilon)\rangle. \quad (\text{A.10})$$

We will make extensive use of this equation in this thesis.

## B. Details on the numerics of the thin superconductor setup

In this appendix, we supplement the discussion of Sec. 5.6.1 by presenting an explicit derivation of  $S_{\text{left/right}}$  and explicit expressions for  $\mathcal{T}_{\nu'\nu}^{(j)}$ .

The scattering matrices between zero-energy and finite-energy modes  $S_{\text{left/right}}$  are obtained as follows. For  $m_{Nx} = m_S$ , the transverse modes  $\psi_{\perp}$  and  $\sin n_y \pi y / W$  are independent of energy and orthogonal. Hence, the scattering matrices  $S_{\text{left/right}}$  become block diagonal, with each block  $S_{\text{left/right},\alpha}$  corresponding to multi-index  $\alpha = (\tau, n_y, n_z)$ . By matching the wavefunction

$$\Lambda_{\alpha}(\mathbf{r}, \varepsilon) = A_{+,\alpha}^{(\varepsilon)} \psi_{+,\alpha}(\mathbf{r}, \varepsilon) + A_{-,\alpha}^{(\varepsilon)} \psi_{-,\alpha}(\mathbf{r}, \varepsilon) \quad (\text{B.1})$$

for  $x \uparrow 0$  with  $\Lambda_{\alpha}(\mathbf{r}, 0)$  for  $x \downarrow 0$ , we obtain

$$\begin{pmatrix} A_{+,\alpha}^{(0)} \\ A_{-,\alpha}^{(\varepsilon)} \end{pmatrix} = \underbrace{\begin{pmatrix} \frac{2\sqrt{k_x(\varepsilon)k_x(0)}}{k_x(\varepsilon)+k_x(0)} & \frac{k_x(0)-k_x(\varepsilon)}{k_x(\varepsilon)+k_x(0)} \\ -\frac{k_x(0)-k_x(\varepsilon)}{k_x(\varepsilon)+k_x(0)} & \frac{2\sqrt{k_x(\varepsilon)k_x(0)}}{k_x(\varepsilon)+k_x(0)} \end{pmatrix}}_{S_{\text{left},\alpha}} \begin{pmatrix} A_{+,\alpha}^{(\varepsilon)} \\ A_{-,\alpha}^{(0)} \end{pmatrix}. \quad (\text{B.2})$$

Note that in our notation we dropped the dependence on  $\alpha$  in  $k_x(\varepsilon)$ . Similarly, by matching the wavefunction

$$\Lambda_{\alpha}(\mathbf{r}, \varepsilon) = B_{+,\alpha}^{(\varepsilon)} \psi_{+,\alpha}(\mathbf{r}, \varepsilon) + B_{-,\alpha}^{(\varepsilon)} \psi_{-,\alpha}(\mathbf{r}, \varepsilon) \quad (\text{B.3})$$

for  $x \downarrow L$  with  $\Lambda_{\alpha}(\mathbf{r}, 0)$  for  $x \uparrow L$ , we obtain

$$\begin{pmatrix} B_{+,\alpha}^{(\varepsilon)} \\ B_{-,\alpha}^{(0)} \end{pmatrix} = \underbrace{\begin{pmatrix} \frac{2\sqrt{k_x(\varepsilon)k_x(0)}}{k_x(\varepsilon)+k_x(0)} e^{i\tau[k_x(0)-k_x(\varepsilon)]L} & \frac{k_x(\varepsilon)-k_x(0)}{k_x(\varepsilon)+k_x(0)} e^{-2i\tau k_x(\varepsilon)L} \\ -\frac{k_x(\varepsilon)-k_x(0)}{k_x(\varepsilon)+k_x(0)} e^{2i\tau k_x(0)L} & \frac{2\sqrt{k_x(\varepsilon)k_x(0)}}{k_x(\varepsilon)+k_x(0)} e^{i\tau[k_x(0)-k_x(\varepsilon)]L} \end{pmatrix}}_{S_{\text{right},\alpha}} \begin{pmatrix} B_{+,\alpha}^{(0)} \\ B_{-,\alpha}^{(\varepsilon)} \end{pmatrix}. \quad (\text{B.4})$$

Next, we present explicit expressions for Eq. (5.56) in chapter (5). These split into

$$\mathcal{T}_{\nu'\nu}^{(j)} = \mathcal{T}_{\varepsilon,\nu'\nu}^{(j)} + \mathcal{T}_{\Delta,\nu'\nu}^{(j)} + \mathcal{T}_{\gamma,\nu'\nu}^{(j)}, \quad (\text{B.5})$$

where

$$\mathcal{T}_{\varepsilon,\nu'\nu}^{(j)} = -\varepsilon \delta_{\nu',\nu} \chi_{\nu',\nu}, \quad (\text{B.6})$$

$$\mathcal{T}_{\Delta,\nu'\nu}^{(j)} = \Delta \chi_{\nu',\nu} \Theta_{\nu',\nu}, \quad (\text{B.7})$$

$$\chi_{\nu',\nu} = -i \frac{e^{iq_{\nu',\nu}x} [e^{iq_{\nu',\nu}\delta L} - 1]}{\hbar q_{\nu',\nu} \sqrt{v'_x v_x}}, \quad (\text{B.8})$$

$$q_{\nu',\nu} = \tau s k_x - \tau' s' k'_x, \quad (\text{B.9})$$

$$\Theta_{\nu',\nu} = \frac{2D_S \tau' \tau d_{\tau'}^* d_{\tau} e^{i(\tau' k'_{S_z} - \tau k_{S_z}) D_S}}{\sqrt{\mathcal{N}_{\nu'} \mathcal{N}_{\nu} v'_{S_z} v_{S_z}}} \times [\text{sinc } D_{\ell}(k'_{S_z} - k_{S_z}) - \text{sinc } D_{\ell}(k'_{S_z} + k_{S_z})], \quad (\text{B.10})$$

where  $k_x = k_x(0)$ . The disorder contribution takes the form

$$\mathcal{T}_{\gamma,\nu'\nu}^{(j)} = 4\tau \sqrt{\gamma} \delta_{\tau',\tau} e^{iq_{\nu',\nu} x_i} (X_{\nu',\nu}^{(i)} + iY_{\nu',\nu}^{(i)}) \times \quad (\text{B.11})$$

$$\frac{d_{\tau'}^* d_{\tau} e^{-i\tau(k_{S_z} - k'_{S_z}) D_S}}{\sqrt{\mathcal{N}_{\nu'} \mathcal{N}_{\nu} v_{S_z} v'_{S_z} v_x v'_x}} \quad (\text{B.12})$$

Here  $\gamma = \hbar v_S / 2\pi\nu_0 \ell$ , and  $X_{\nu',\nu}^{(i)}$  and  $Y_{\nu',\nu}^{(i)}$  are correlated Gaussian random variables with zero mean. The covariance matrix of  $(X_{\nu',\nu}, Y_{\nu',\nu})^T$  reads

$$C = \begin{pmatrix} C_{XX}^{(x)} & C_{XY}^{(x)} \\ (C_{XY}^{(x)})^T & C_{YY}^{(x)} \end{pmatrix} C^{(y)} C^{(z)}. \quad (\text{B.13})$$

In Eq. (B.13), we dropped the indices  $(\nu'_1, \nu_1), (\nu'_2, \nu_2)$  that are attached to each  $C$  and the  $C^{(x)}$ ,  $C^{(y)}$ , and  $C^{(z)}$  are multiplied element wise. Together with the fact that  $X^{(i)}$  and  $Y^{(i)}$  have zero mean and are multivariate Gaussian random variables, the knowledge of the covariance matrix  $C$  allows us to draw the random numbers for each slice in our numerics.

For three dimensions, the explicit forms of the  $C$ 's are

---


$$C_{XX,(\nu'_1,\nu_1),(\nu'_2,\nu_2)}^{(x)} = \frac{\delta L}{2} [\text{sinc } \delta L(q_1 - q_2) + \text{sinc } \delta L(q_1 + q_2)], \quad (\text{B.14})$$

$$C_{XY,(\nu'_1,\nu_1),(\nu'_2,\nu_2)}^{(x)} = \frac{q_2 - q_1}{4} \delta L^2 [\text{sinc } \delta L(q_1 - q_2)/2]^2 + \frac{q_2 + q_1}{4} \delta L^2 [\text{sinc } \delta L(q_1 + q_2)/2]^2, \quad (\text{B.15})$$

$$C_{YY,(\nu'_1,\nu_1),(\nu'_2,\nu_2)}^{(x)} = \frac{\delta L}{2} [\text{sinc } \delta L(q_1 - q_2) - \text{sinc } \delta L(q_1 + q_2)], \quad (\text{B.16})$$

$$C_{(\nu'_1,\nu_1),(\nu'_2,\nu_2)}^{(y)} = \frac{1}{2D_N} \left[ \delta_{0,n'_{y,1}+n_{y,1}-n'_{y,2}-n_{y,2}} + \delta_{0,n'_{y,1}-n_{y,1}-n'_{y,2}+n_{y,2}} + \delta_{0,n'_{y,1}-n_{y,1}+n'_{y,2}-n_{y,2}} \right. \\ \left. - \delta_{0,n'_{y,1}-n_{y,1}-n'_{y,2}-n_{y,2}} - \delta_{0,n'_{y,1}-n_{y,1}+n'_{y,2}+n_{y,2}} - \delta_{0,n'_{y,1}+n_{y,1}-n'_{y,2}+n_{y,2}} \right. \\ \left. - \delta_{0,n'_{y,1}+n_{y,1}+n'_{y,2}-n_{y,2}} \right], \quad (\text{B.17})$$

$$C_{(\nu'_1,\nu_1),(\nu'_2,\nu_2)}^{(z)} = \frac{D_S}{8} [\text{sinc } D_\ell(k'_{S_{z1}} + k_{S_{z1}} + k'_{S_{z2}} + k_{S_{z2}}) + \text{sinc } D_\ell(k'_{S_{z1}} + k_{S_{z1}} - k'_{S_{z2}} - k_{S_{z2}}) \\ + \text{sinc } D_\ell(k'_{S_{z1}} - k_{S_{z1}} - k'_{S_{z2}} + k_{S_{z2}}) + \text{sinc } D_\ell(k'_{S_{z1}} - k_{S_{z1}} + k'_{S_{z2}} - k_{S_{z2}}) \\ - \text{sinc } D_\ell(k'_{S_{z1}} - k_{S_{z1}} - k'_{S_{z2}} - k_{S_{z2}}) - \text{sinc } D_\ell(k'_{S_{z1}} - k_{S_{z1}} + k'_{S_{z2}} + k_{S_{z2}}) \\ - \text{sinc } D_\ell(k'_{S_{z1}} + k_{S_{z1}} - k'_{S_{z2}} + k_{S_{z2}}) - \text{sinc } D_\ell(k'_{S_{z1}} + k_{S_{z1}} + k'_{S_{z2}} - k_{S_{z2}})], \quad (\text{B.18})$$

where  $q_i = q_{\nu'_i,\nu_i}$ ,  $\delta_{n,m}$  is the Kronecker delta and  $\text{sinc } x = (\sin x)/x$ . For two dimensions the  $C^{(x)}$  and  $C^{(y)}$  are the same as in three dimension. For the  $y$  direction we restrict the multi-index  $\nu$  to  $n_y = 1$  and set  $C^{(y)}$  equal to the identity matrix.



## C. Transfer matrix for the YSR problem

This appendix is based on the appendix of Ref. [Kien 17] (doi), copyright remains with ©2017 American Physical Society.

In this appendix, we present explicit expressions for the transfer matrix of a thin, disordered and superconducting slice that has a circular or a spherical shape. Using Eq. (6.37) this enables one to calculate the corresponding scattering matrix of the thin slice.

### C.1. Circular slice

First we consider a circular slice of a two-dimensional superconductor. In this case, we define the radial part of the propagating waves in Eq. (6.34) as

$$\mathcal{R}_{em\pm}(r) = \sqrt{\frac{k_F}{4v_F}} H_m^{(\pm)}(k_F r) \begin{pmatrix} 1 \\ 0 \end{pmatrix},$$

for electrons and

$$\mathcal{R}_{hm\pm}(r) = \sqrt{\frac{k_F}{4v_F}} H_m^{(\mp)}(k_F r) \begin{pmatrix} 0 \\ 1 \end{pmatrix},$$

for holes.

Within first order Born approximation, for a slice of width  $dr$ , at an energy  $\varepsilon$  and at a radius  $r_n$  from the origin, we obtain the transfer matrix

$$\mathcal{T}_{\nu'\nu}^{(n)} = \mathcal{R}_{\nu'}^\dagger(r_n) \left( d\hat{T}^{(n)} \delta_{m',m} + d\hat{\Gamma}_{m',m}^{(n)} \right) \mathcal{R}_\nu(r_n),$$

with the same multi-index  $\nu$  as in the main text. The term diagonal in angular momentum reads

$$d\hat{T}^{(n)} = (\Delta\tau_x - \epsilon) 2\pi r_n dr.$$

For the disorder element we get

$$d\hat{\Gamma}_{m',m}^{(n)} = \sqrt{\gamma 2\pi r_n dr} X_{m'-m}^{(n)} \tau_z.$$

The random part is absorbed into

$$X_{m'-m}^{(n)} = \begin{cases} Y_0^{(n)} & \text{for } m=m' \\ \frac{Y_{|m'-m|}^{(n)} + i \text{sign}(m'-m) Z_{|m'-m|}^{(n)}}{\sqrt{2}} & \text{else} \end{cases}$$

corresponding to the Fourier transform of white noise. Here  $Y_m^{(n)}$  and  $Z_m^{(n)}$  are independent, normally distributed random variables with zero mean and variance one. Note that not all elements of  $X^{(n)}$  are independent since  $X_{m'-m} = X_{m-m'}^*$ .

## C.2. Spherical slice

Next we calculate the transfer matrix of a thin, spherical slice in three dimensions. In this case, the radial modes are defined as

$$\mathcal{R}_{em\pm}(r) = \sqrt{\frac{k_F^2}{4\pi v_F}} h_l^{(\pm)}(k_F r) \begin{pmatrix} 1 \\ 0 \end{pmatrix}$$

for electrons and

$$\mathcal{R}_{hm\pm}(r) = \sqrt{\frac{k_F^2}{4\pi v_F}} h_l^{(\mp)}(k_F r) \begin{pmatrix} 0 \\ 1 \end{pmatrix}$$

for holes, with a total angular momentum quantum number  $l$ .

Within first order Born approximation and for a spherical slice of width  $dr$  at a radius  $r_n$ , the transfer matrix reads

$$\mathcal{T}_{\nu'\nu}^{(n)} = \mathcal{R}_{\nu'}^\dagger(r_n) \left( d\hat{T}^{(n)} \delta_{l'l} \delta_{m'm} + d\hat{\Gamma}_{l'm'lm}^{(n)} \right) \mathcal{R}_\nu(r_n)$$

similar to Eq. (C.1).

The term diagonal in the angular momentum quantum numbers reads

$$d\hat{T}^{(n)} = (\Delta\tau_x - \varepsilon) 4\pi r_n^2 dr$$

and the disorder element is

$$d\hat{\Gamma}_{l'm'lm}^{(n)} = \tau_z \sqrt{\gamma 4\pi r_n^2} dr \Xi_{l'm'lm}.$$

The random variable  $\Xi_{l'm'lm}$  takes a more complicated form in three than in two dimensions, due to the involvement of the product of two spherical harmonics in the calculation of the matrix elements in Eq. (6.38). These products can be expressed as a sum over single spherical harmonics for which explicit expressions are known [Vars 88]. For these single spherical harmonics we can calculate the overlap with the Gaussian disorder potential. Following this strategy we obtain

$$\Xi_{l'm'lm} = \sum_{L=0}^{\infty} c_{l'm'lm}^{L, \Delta m} X_{L, \Delta m}$$

where the coefficients for the transformation between a single and the product of two spherical harmonics are

$$c_{l'm'lm}^{L, \Delta m} = (-1)^m \sqrt{\frac{(2l'+1)(2l+1)}{4\pi(2L+1)}} \quad (\text{C.1})$$

$$\times C_{l',0,l,0}^{L,0} C_{l',m',l,m}^{L,\Delta m}. \quad (\text{C.2})$$

Here

$$C_{l',m',l,m}^{L,\Delta m} = \langle l', m', l, m | L, \Delta m \rangle$$

are the Clebsch Gordan coefficients [Vars 88]. Additionally, the overlap of the single spherical harmonics with the angular part of the Gaussian disorder potential yields the random numbers [Lang 15]

$$X_{L,\Delta m}^{(n)} = \begin{cases} \frac{Y_{L,\Delta m}^{(n)} + iZ_{L,\Delta m}^{(n)}}{\sqrt{2}} & \text{for } \Delta m > 0 \\ Y_{L,0}^{(n)} & \text{for } \Delta m = 0 \\ (-1)^{\Delta m} X_{L,-\Delta m}^{(n)} & \text{for } \Delta m < 0 \end{cases}$$

Here, similar to the two dimensional case,  $Y_{L,\Delta m}$  and  $Z_{L,\Delta m}$  are independent, normally distributed random variables with zero mean and variance one.



## Bibliography

- [Akhm 11] A. R. Akhmerov, J. P. Dahlhaus, F. Hassler, M. Wimmer, and C. W. J. Beenakker, “*Quantized Conductance at the Majorana Phase Transition in a Disordered Superconducting Wire*”, Phys. Rev. Lett. **106**, 057001 (2011).
- [Albr 16] S. M. Albrecht, A. P. Higginbotham, M. Madsen, F. Kuemmeth, T. S. Jespersen, J. Nygård, P. Krogstrup, and C. M. Marcus, “*Exponential protection of zero modes in Majorana islands*”, Nature **531**, 206 (2016).
- [Alic 12] J. Alicea, “*New directions in the pursuit of Majorana fermions in solid state systems*”, Rep. Prog. Phys. **75**, 076501 (2012).
- [Ande 59] P. W. Anderson, “*Theory of dirty superconductors*”, J. Phys. Chem. Solids **11**, 26–30 (1959).
- [Ando 13] Y. Ando, “*Topological Insulator Materials*”, J. Phys. Soc. Jpn. **82**, 102001 (2013).
- [Andr 64] A. F. Andreev, “*The Thermal Conductivity of the Intermediate State in Superconductors*”, Zh. Eksp. Teor. Fiz. **46**, 1823 (1964). [Sov. Phys. JETP **19**, 1228 (1964)].
- [Anti 18] A. E. Antipov, A. Bargerbos, G. W. Winkler, B. Bauer, E. Rossi, and R. M. Lutchyn, “*Effects of Gate-Induced Electric Fields on Semiconductor Majorana Nanowires*”, Phys. Rev. X **8**, 031041 (2018).
- [Ashc 76] N. Ashcroft and N. D. Mermin. *Solid state physics*. Holt, Rinehart and Winston, New York (1976).
- [Bagr 12] D. Bagrets and A. Altland, “*Class D Spectral Peak in Majorana Quantum Wires*”, Phys. Rev. Lett. **109**, 227005 (2012).
- [Bard 07] J. H. Bardarson, J. Tworzydło, P. W. Brouwer, and C. W. J. Beenakker, “*One-Parameter Scaling at the Dirac Point in Graphene*”, Phys. Rev. Lett. **99**, 106801 (2007).
- [Bard 57] J. Bardeen, L. N. Cooper, and J. R. Schrieffer, “*Theory of Superconductivity*”, Physical Review **108**, 1175–1204 (1957).
- [Berg 03] C. Bergemann, A. P. Mackenzie, S. R. Julian, D. Forsythe, and E. Ohmichi, “*Quasi-two-dimensional Fermi liquid properties of the unconventional superconductor Sr<sub>2</sub>RuO<sub>4</sub>*”, Adv. Phys. **52**, 639–725 (2003).

- [Binn 83] G. Binnig and H. Rohrer, “*Scanning tunneling microscopy*”, Surf. Sci. **126**, 236 – 244 (1983).
- [Brau 13] B. Braunecker and P. Simon, “*Interplay between Classical Magnetic Moments and Superconductivity in Quantum One-Dimensional Conductors: Toward a Self-Sustained Topological Majorana Phase*”, Phys. Rev. Lett. **111**, 147202 (2013).
- [Brou 03] P. W. Brouwer, A. Furusaki, and C. Mudry, “*Universality of delocalization in unconventional dirty superconducting wires with broken spin-rotation symmetry*”, Phys. Rev. B **67**, 014530 (2003).
- [Brou 11a] P. W. Brouwer, M. Duckheim, A. Romito, and F. von Oppen, “*Probability Distribution of Majorana End-State Energies in Disordered Wires*”, Phys. Rev. Lett. **107**, 196804 (2011).
- [Brou 11b] P. W. Brouwer, M. Duckheim, A. Romito, and F. von Oppen, “*Topological superconducting phases in disordered quantum wires with strong spin-orbit coupling*”, Phys. Rev. B **84**, 144526 (2011).
- [Chan 15] W. Chang, S. M. Albrecht, T. S. Jespersen, F. Kuemmeth, P. Krogstrup, J. Nygård, and C. M. Marcus, “*Hard gap in epitaxial semiconductor-superconductor nanowires*”, Nat. Nanotechnol. **10**, 232 (2015).
- [Chen 17] J. Chen, P. Yu, J. Stenger, M. Hoeschele, D. Car, S. R. Plissard, E. P. A. M. Bakkers, T. D. Stanescu, and S. M. Frolov, “*Experimental phase diagram of zero-bias conductance peaks in superconductor/semiconductor nanowire devices*”, Sci. Adv. **3**, e1701476 (2017).
- [Choi 17] D.-J. Choi, C. R.-V., J. de Bruijckere, M. M. Ugeda, N. Lorente, and J. I. Pascual, “*Mapping the orbital structure of impurity bound states in a superconductor*”, Nat. Comm. **8**, 15175 (2017).
- [Choi 18] D.-J. Choi, C. G. Fernández, E. Herrera, C. Rubio-Verdú, M. M. Ugeda, I. Guillamón, H. Suderow, J. I. Pascual, and N. Lorente, “*Influence of Magnetic Ordering between Cr Adatoms on the Yu-Shiba-Rusinov States of the  $\beta$ -Bi<sub>2</sub>Pd Superconductor*”, Phys. Rev. Lett. **120**, 167001 (2018).
- [Chun 11] S. B. Chung, H.-J. Zhang, X.-L. Qi, and S.-C. Zhang, “*Topological superconducting phase and Majorana fermions in half-metal/superconductor heterostructures*”, Phys. Rev. B **84**, 060510 (2011).
- [Chur 13] H. O. H. Churchill, V. Fatemi, K. Grove-Rasmussen, M. T. Deng, P. Caroff, H. Q. Xu, and C. M. Marcus, “*Superconductor-nanowire devices from tunneling to the multichannel regime: Zero-bias oscillations and magnetoconductance crossover*”, Phys. Rev. B **87**, 241401 (2013).
- [Clog 62] A. M. Clogston, “*Impurity States in Metals*”, Phys. Rev. **125**, 439–443 (1962).

- 
- [Cole 16] W. S. Cole, J. D. Sau, and S. Das Sarma, “Proximity effect and Majorana bound states in clean semiconductor nanowires coupled to disordered superconductors”, *Phys. Rev. B* **94**, 140505 (2016).
- [Das 15] S. Das Sarma, H.-Y. Hui, P. M. R. Brydon, and J. D. Sau, “Substrate-induced Majorana renormalization in topological nanowires”, *New J. Phys.* **17**, 075001 (2015).
- [Das 12] A. Das, Y. Ronen, Y. Most, Y. Oreg, M. Heiblum, and H. Shtrikman, “Zero-bias peaks and splitting in an Al-InAs nanowire topological superconductor as a signature of Majorana fermions”, *Nat. Phys.* **8**, 887–895 (2012).
- [Datt 97] S. Datta. *Electronic Transport in Mesoscopic Systems. Cambridge Studies in Semiconductor Physics and Microelectronic Engineering*, Cambridge University Press (1997).
- [Deng 12] M. T. Deng, C. L. Yu, G. Y. Huang, M. Larsson, P. Caroff, and H. Q. Xu, “Anomalous Zero-Bias Conductance Peak in a Nb-InSb Nanowire-Nb Hybrid Device”, *Nano Lett.* **12**, 6414–6419 (2012).
- [Deng 16] M. T. Deng, S. Vaitiekenas, E. B. Hansen, J. Danon, M. Leijnse, K. Flensberg, J. Nygård, P. Krogstrup, and C. M. Marcus, “Majorana bound state in a coupled quantum-dot hybrid-nanowire system”, *Science* **354**, 1557–1562 (2016).
- [Diez 12] M. Diez, J. P. Dahlhaus, M. Wimmer, and C. W. J. Beenakker, “Andreev reflection from a topological superconductor with chiral symmetry”, *Phys. Rev. B* **86**, 094501 (2012).
- [Duck 11] M. Duckheim and P. W. Brouwer, “Andreev reflection from noncentrosymmetric superconductors and Majorana bound-state generation in half-metallic ferromagnets”, *Phys. Rev. B* **83**, 054513 (2011).
- [Dumi 15] E. Dumitrescu, B. Roberts, S. Tewari, J. D. Sau, and S. Das Sarma, “Majorana fermions in chiral topological ferromagnetic nanowires”, *Phys. Rev. B* **91**, 094505 (2015).
- [Elli 15] S. R. Elliott and M. Franz, “Colloquium: Majorana fermions in nuclear, particle, and solid-state physics”, *Rev. Mod. Phys.* **87**, 137–163 (2015).
- [Fari 18] L. Farinacci, G. Ahmadi, G. Reecht, M. Ruby, N. Bogdanoff, O. Peters, B. W. Heinrich, F. von Oppen, and K. J. Franke, “Tuning the coupling of an individual magnetic impurity to a superconductor: quantum phase transition and transport”, arxiv:1807.01344 (2018).
- [Feld 17] B. E. Feldman, M. T. Randeria, J. Li, S. Jeon, Y. Xie, Z. Wang, I. K. Drozdov, B. A. Bernevig, and A. Yazdani, “High-resolution studies of the Majorana atomic chain platform”, *Nat. Phys.* **13**, 286–291 (2017).

- [Flen 10] K. Flensberg, “*Tunneling characteristics of a chain of Majorana bound states*”, Phys. Rev. B **82**, 180516 (2010).
- [Fran 11] K. J. Franke, G. Schulze, and J. I. Pascual, “*Competition of Superconducting Phenomena and Kondo Screening at the Nanoscale*”, Science **332**, 940–944 (2011).
- [Fu 07] L. Fu, C. L. Kane, and E. J. Mele, “*Topological Insulators in Three Dimensions*”, Phys. Rev. Lett. **98**, 106803 (2007).
- [Fu 08] L. Fu and C. L. Kane, “*Superconducting Proximity Effect and Majorana Fermions at the Surface of a Topological Insulator*”, Phys. Rev. Lett. **100**, 096407 (2008).
- [Fu 09] L. Fu and C. L. Kane, “*Josephson current and noise at a superconductor/quantum-spin-Hall-insulator/superconductor junction*”, Phys. Rev. B **79**, 161408 (2009).
- [Groo 83] R. A. de Groot, F. M. Mueller, P. G. v. Engen, and K. H. J. Buschow, “*New Class of Materials: Half-Metallic Ferromagnets*”, Phys. Rev. Lett. **50**, 2024–2027 (1983).
- [Gul 17] O. Gül, H. Zhang, F. K. de Vries, J. van Veen, K. Zuo, V. Mourik, S. Conesa-Boj, M. P. Nowak, D. J. van Woerkom, M. Quintero-Pérez, M. C. Cassidy, A. Geresdi, S. Koelling, D. Car, S. R. Plissard, E. P. A. M. Bakkers, and L. P. Kouwenhoven, “*Hard Superconducting Gap in InSb Nanowires*”, Nano Lett. **17**, 2690–2696 (2017).
- [Gul 18] O. Gül, H. Zhang, J. D. S. Bommer, M. W. A. de Moor, D. Car, S. R. Plissard, E. P. A. M. Bakkers, A. Geresdi, K. Watanabe, T. Taniguchi, and L. P. Kouwenhoven, “*Ballistic Majorana nanowire devices*”, Nature Nanotechnology **13**, 192–197 (2018).
- [Hatt 15] N. Hatter, B. W. Heinrich, M. Ruby, J. I. Pascual, and K. J. Franke, “*Magnetic anisotropy in Shiba bound states across a quantum phase transition*”, Nat. Commun. **6**, 8988 (2015).
- [Hatt 17] N. Hatter, B. W. Heinrich, D. Rolf, and K. J. Franke, “*Scaling of Yu-Shiba-Rusinov energies in the weak-coupling Kondo regime*”, Nat. Comm. **8**, 2016 (2017).
- [Heck 16] B. van Heck, R. M. Lutchyn, and L. I. Glazman, “*Conductance of a proximitized nanowire in the Coulomb blockade regime*”, Phys. Rev. B **93**, 235431 (2016).
- [Hein 18] B. W. Heinrich, J. I. Pascual, and K. J. Franke, “*Single magnetic adsorbates on s-wave superconductors*”, Progr. Surf. Sci. **93**, 1–19 (2018).

- 
- [Hoff 15] S. Hoffman, J. Klinovaja, T. Meng, and D. Loss, “*Impurity-induced quantum phase transitions and magnetic order in conventional superconductors: Competition between bound and quasiparticle states*”, Phys. Rev. B **92**, 125422 (2015).
- [Hui 15] H.-Y. Hui, J. D. Sau, and S. Das Sarma, “*Bulk disorder in the superconductor affects proximity-induced topological superconductivity*”, Phys. Rev. B **92**, 174512 (2015).
- [Ivan 01] D. A. Ivanov, “*Non-Abelian Statistics of Half-Quantum Vortices in p-Wave Superconductors*”, Phys. Rev. Lett. **86**, 268–271 (2001).
- [Ji 08] S.-H. Ji, T. Zhang, Y.-S. Fu, X. Chen, X.-C. Ma, J. Li, W.-H. Duan, J.-F. Jia, and Q.-K. Xue, “*High-Resolution Scanning Tunneling Spectroscopy of Magnetic Impurity Induced Bound States in the Superconducting Gap of Pb Thin Films*”, Phys. Rev. Lett. **100**, 226801 (2008).
- [Ji 10] S.-H. Ji, T. Zhang, Y.-S. Fu, X. Chen, J.-F. Jia, Q.-K. Xue, and X.-C. Ma, “*Application of magnetic atom induced bound states in superconducting gap for chemical identification of single magnetic atoms*”, Appl. Phys. Lett. **96**, 073113 (2010).
- [Kane 05] C. L. Kane and E. J. Mele, “ *$Z_2$  Topological Order and the Quantum Spin Hall Effect*”, Phys. Rev. Lett. **95**, 146802 (2005).
- [Kezi 18] S. Kezilebieke, M. Dvorak, T. Ojanen, and P. Liljeroth, “*Coupled Yu-Shiba-Rusinov States in Molecular Dimers on NbSe<sub>2</sub>*”, Nano Lett. **18**, 2311–2315 (2018).
- [Kien 17] T. Kiendl, F. von Oppen, and P. W. Brouwer, “*Effects of nonmagnetic disorder on the energy of Yu-Shiba-Rusinov states*”, Phys. Rev. B **96**, 134501 (2017).
- [Kien 18] T. Kiendl, F. von Oppen, and P. W. Brouwer, “*Renormalization effects in spin-polarized metallic wires proximitized by a superconductor: A scattering approach*”, arXiv:1809.08023 (2018).
- [Kim 14] Y. Kim, M. Cheng, B. Bauer, R. M. Lutchyn, and S. Das Sarma, “*Helical order in one-dimensional magnetic atom chains and possible emergence of Majorana bound states*”, Phys. Rev. B **90**, 060401 (2014).
- [Kim 18] H. Kim, A. Palacio-Morales, T. Posske, L. Rózsa, K. Palotás, L. Szunyogh, M. Thorwart, and R. Wiesendanger, “*Toward tailoring Majorana bound states in artificially constructed magnetic atom chains on elemental superconductors*”, Sci. Adv. **4** (2018).
- [Kita 01] A. Y. Kitaev, “*Unpaired Majorana fermions in quantum wires*”, Phys. Usp. **44**, 131 (2001).
-

- [Kita 03] A. Y. Kitaev, “*Fault-tolerant quantum computation by anyons*”, Ann. Phys. **303**, 2 – 30 (2003).
- [Kita 09] A. Y. Kitaev, “*Periodic table for topological insulators and superconductors*”, AIP Conf. Proc. **1134**, 22–30 (2009).
- [Kjae 17] M. Kjaergaard, H. J. Suominen, M. P. Nowak, A. R. Akhmerov, J. Shabani, C. J. Palmström, F. Nichele, and C. M. Marcus, “*Transparent Semiconductor-Superconductor Interface and Induced Gap in an Epitaxial Heterostructure Josephson Junction*”, Phys. Rev. Applied **7**, 034029 (2017).
- [Klin 13] J. Klinovaja, P. Stano, A. Yazdani, and D. Loss, “*Topological Superconductivity and Majorana Fermions in RKKY Systems*”, Phys. Rev. Lett. **111**, 186805 (2013).
- [Klit 80] K. v. Klitzing, G. Dorda, and M. Pepper, “*New Method for High-Accuracy Determination of the Fine-Structure Constant Based on Quantized Hall Resistance*”, Phys. Rev. Lett. **45**, 494–497 (1980).
- [Kohm 85] M. Kohmoto, “*Topological invariant and the quantization of the Hall conductance*”, Ann. Physics **160**, 343–354 (1985).
- [Krog 15] P. Krogstrup, N. L. B. Ziino, W. Chang, S. M. Albrecht, M. H. Madsen, E. Johnson, J. Nygård, C. Marcus, and T. S. Jespersen, “*Epitaxy of semiconductor-superconductor nanowires*”, Nature Materials **14**, 400 (2015).
- [Kupf 09] J. N. Kupferschmidt and P. W. Brouwer, “*Enhanced triplet Andreev reflection off a domain wall in a lateral geometry*”, Physical Review B **80** (2009).
- [Kupf 11] J. N. Kupferschmidt and P. W. Brouwer, “*Andreev reflection at half-metal/superconductor interfaces with nonuniform magnetization*”, Phys. Rev. B **83**, 014512 (2011).
- [Lang 15] A. Lang and C. Schwab, “*Isotropic Gaussian random fields on the sphere: Regularity, fast simulation and stochastic partial differential equations*”, Ann. Appl. Probab. **25**, 3047–3094 (2015).
- [Law 09] K. T. Law, P. A. Lee, and T. K. Ng, “*Majorana Fermion Induced Resonant Andreev Reflection*”, Phys. Rev. Lett. **103**, 237001 (2009).
- [Lin 12] C.-H. Lin, J. D. Sau, and S. Das Sarma, “*Zero-bias conductance peak in Majorana wires made of semiconductor/superconductor hybrid structures*”, Phys. Rev. B **86**, 224511 (2012).
- [Lipp 50] B. A. Lippmann and J. Schwinger, “*Variational Principles for Scattering Processes. I*”, Phys. Rev. **79**, 469–480 (1950).
- [Liu 12] J. Liu, A. C. Potter, K. T. Law, and P. A. Lee, “*Zero-Bias Peaks in the Tunneling Conductance of Spin-Orbit-Coupled Superconducting Wires with and without Majorana End-States*”, Phys. Rev. Lett. **109**, 267002 (2012).

- 
- [Liu 17] C.-X. Liu, J. D. Sau, and S. Das Sarma, “*Role of dissipation in realistic Majorana nanowires*”, *Phys. Rev. B* **95**, 054502 (2017).
- [Lutc 10] R. M. Lutchyn, J. D. Sau, and S. Das Sarma, “*Majorana Fermions and a Topological Phase Transition in Semiconductor-Superconductor Heterostructures*”, *Phys. Rev. Lett.* **105**, 077001 (2010).
- [Mack 03] A. P. Mackenzie and Y. Maeno, “*The superconductivity of Sr<sub>2</sub>RuO<sub>4</sub> and the physics of spin-triplet pairing*”, *Rev. Mod. Phys.* **75**, 657–712 (2003).
- [Majo 37] E. Majorana, “*Teoria simmetrica dell’elettrone e del positrone*”, *Il Nuovo Cimento* (1924-1942) **14**, 171 (1937).
- [Meis 33] W. Meissner and R. Ochsenfeld, “*Ein neuer Effekt bei Eintritt der Supraleitfähigkeit*”, *Naturwissenschaften* **21**, 787–788 (1933).
- [Mena 15] G. C. Ménard, S. Guissart, C. Brun, S. Pons, V. S. Stolyarov, F. Debontridder, M. V. Leclerc, E. Janod, L. Cario, D. Roditchev, P. Simon, and T. Cren, “*Coherent long-range magnetic bound states in a superconductor*”, *Nat. Phys.* **11**, 1013–1016 (2015).
- [Meng 15] T. Meng, J. Klinovaja, S. Hoffman, P. Simon, and D. Loss, “*Superconducting gap renormalization around two magnetic impurities: From Shiba to Andreev bound states*”, *Phys. Rev. B* **92**, 064503 (2015).
- [Mikk 18] A. E. G. Mikkelsen, P. Kotetes, P. Krogstrup, and K. Flensberg, “*Hybridization at superconductor-semiconductor interfaces*”, arXiv 1801.03439 (2018).
- [Moca 08] C. P. Moca, E. Demler, B. Jankó, and G. Zaránd, “*Spin-resolved spectra of Shiba multiplets from Mn impurities in MgB<sub>2</sub>*”, *Phys. Rev. B* **77**, 174516 (2008).
- [Moor 07] J. E. Moore and L. Balents, “*Topological invariants of time-reversal-invariant band structures*”, *Phys. Rev. B* **75**, 121306 (2007).
- [Morr 06] D. K. Morr and J. Y., “*Impurities, quantum interference, and quantum phase transitions in s-wave superconductors*”, *Phys. Rev. B* **73**, 224511 (2006).
- [Mour 12] V. Mourik, K. Zuo, S. M. Frolov, S. R. Plissard, E. P. A. M. Bakkers, and L. P. Kouwenhoven, “*Signatures of Majorana Fermions in Hybrid Superconductor-Semiconductor Nanowire Devices*”, *Science* **336**, 1003–1007 (2012).
- [Nadj 13] S. Nadj-Perge, I. K. Drozdov, B. A. Bernevig, and A. Yazdani, “*Proposal for realizing Majorana fermions in chains of magnetic atoms on a superconductor*”, *Phys. Rev. B* **88**, 020407 (2013).
- [Nadj 14] S. Nadj-Perge, I. K. Drozdov, J. Li, H. Chen, S. Jeon, J. Seo, A. H. MacDonald, B. A. Bernevig, and A. Yazdani, “*Observation of Majorana fermions in ferromagnetic atomic chains on a superconductor*”, *Science* **346**, 602–607 (2014).
-

- [Naya 08] C. Nayak, S. H. Simon, A. Stern, M. Freedman, and S. Das Sarma, “*Non-Abelian anyons and topological quantum computation*”, *Rev. Mod. Phys.* **80**, 1083–1159 (2008).
- [Nich 17] F. Nichele, A. C. C. Drachmann, A. M. Whiticar, E. C. T. O’Farrell, H. J. Suominen, A. Fornieri, T. Wang, G. C. Gardner, C. Thomas, A. T. Hatke, P. Krogstrup, M. J. Manfra, K. Flensberg, and C. M. Marcus, “*Scaling of Majorana Zero-Bias Conductance Peaks*”, *Phys. Rev. Lett.* **119**, 136803 (2017).
- [Nils 08] J. Nilsson, A. R. Akhmerov, and C. W. J. Beenakker, “*Splitting of a Cooper Pair by a Pair of Majorana Bound States*”, *Phys. Rev. Lett.* **101**, 120403 (2008).
- [Olve 10] F. W. Olver, D. W. Lozier, R. F. Boisvert, and C. W. Clark. *NIST Handbook of Mathematical Functions*. Cambridge University Press, New York (2010).
- [Oreg 10] Y. Oreg, G. Refael, and F. von Oppen, “*Helical Liquids and Majorana Bound States in Quantum Wires*”, *Phys. Rev. Lett.* **105**, 177002 (2010).
- [Park 98] J.-H. Park, E. Vescovo, H.-J. Kim, C. Kwon, R. Ramesh, and T. Venkatesan, “*Direct evidence for a half-metallic ferromagnet*”, *Nature* **392**, 794–796 (1998).
- [Pawl 16] R. Pawlak, M. Kisiel, J. Klinovaja, T. Meier, S. Kawai, T. Glatzel, D. Loss, and E. Meyer, “*Probing atomic structure and Majorana wavefunctions in mono-atomic Fe chains on superconducting Pb surface*”, *NPJ Quantum Inf.* **2**, 16035 (2016).
- [Peng 15] Y. Peng, F. Pientka, L. I. Glazman, and F. von Oppen, “*Strong Localization of Majorana End States in Chains of Magnetic Adatoms*”, *Phys. Rev. Lett.* **114**, 106801 (2015).
- [Pien 12] F. Pientka, G. Kells, A. Romito, P. W. Brouwer, and F. von Oppen, “*Enhanced Zero-Bias Majorana Peak in the Differential Tunneling Conductance of Disordered Multisubband Quantum-Wire/Superconductor Junctions*”, *Phys. Rev. Lett.* **109**, 227006 (2012).
- [Pien 13] F. Pientka, L. I. Glazman, and F. von Oppen, “*Topological superconducting phase in helical Shiba chains*”, *Phys. Rev. B* **88**, 155420 (2013).
- [Pien 14a] F. Pientka. *Signatures of Majorana bound states in one-dimensional topological superconductors*. PhD thesis, Freie Universität Berlin (2014).
- [Pien 14b] F. Pientka, L. I. Glazman, and F. von Oppen, “*Unconventional topological phase transitions in helical Shiba chains*”, *Phys. Rev. B* **89**, 180505 (2014).
- [Pien 15] F. Pientka, Y. Peng, L. Glazman, and F. von Oppen, “*Topological superconducting phase and Majorana bound states in Shiba chains*”, *Physica Scripta* **2015**, 014008 (2015).

- [Rain 13] D. Rainis, L. Trifunovic, J. Klinovaja, and D. Loss, “Towards a realistic transport modeling in a superconducting nanowire with Majorana fermions”, Phys. Rev. B **87**, 024515 (2013).
- [Read 00] N. Read and D. Green, “Paired states of fermions in two dimensions with breaking of parity and time-reversal symmetries and the fractional quantum Hall effect”, Phys. Rev. B **61**, 10267–10297 (2000).
- [Reeg 17] C. Reeg, D. Loss, and J. Klinovaja, “Finite-size effects in a nanowire strongly coupled to a thin superconducting shell”, Phys. Rev. B **96**, 125426 (2017).
- [Reeg 18a] C. Reeg, D. Loss, and J. Klinovaja, “Metallization of a Rashba wire by a superconducting layer in the strong-proximity regime”, Phys. Rev. B **97**, 165425 (2018).
- [Reeg 18b] C. Reeg, D. Loss, and J. Klinovaja, “Proximity effect in a two-dimensional electron gas coupled to a thin superconducting layer”, Beilstein J. of Nanotechnol. **9**, 1263–1271 (2018).
- [Rokh 12] L. P. Rokhinson, X. Liu, and J. K. Furdyna, “The fractional a.c. Josephson effect in a semiconductor-superconductor nanowire as a signature of Majorana particles”, Nat. Phys. **8**, 795 (2012).
- [Ruby 15a] M. Ruby, F. Pientka, Y. Peng, F. von Oppen, B. W. Heinrich, and K. J. Franke, “End States and Subgap Structure in Proximity-Coupled Chains of Magnetic Adatoms”, Phys. Rev. Lett. **115**, 197204 (2015).
- [Ruby 15b] M. Ruby, F. Pientka, Y. Peng, F. von Oppen, B. W. Heinrich, and K. J. Franke, “Tunneling Processes into Localized Subgap States in Superconductors”, Phys. Rev. Lett. **115**, 087001 (2015).
- [Ruby 16] M. Ruby, Y. Peng, F. von Oppen, B. W. Heinrich, and K. J. Franke, “Orbital Picture of Yu-Shiba-Rusinov Multiplets”, Phys. Rev. Lett. **117**, 186801 (2016).
- [Ruby 17] M. Ruby, B. W. Heinrich, Y. Peng, F. von Oppen, and K. J. Franke, “Exploring a proximity-coupled Co chain on Pb(110) as a possible Majorana platform”, arXiv:1704.05756 (2017).
- [Ruby 18] M. Ruby, B. W. Heinrich, Y. Peng, F. von Oppen, and K. J. Franke, “Wave-Function Hybridization in Yu-Shiba-Rusinov Dimers”, Phys. Rev. Lett. **120**, 156803 (2018).
- [Rusi 68] A. I. Rusinov, “Superconductivity near a Paramagnetic Impurity”, Zh. Eksp. Teor. Fiz. Pisma Red. **9**, 146 (1968). [JETP Lett. **9**, 85 (1969)].
- [Rusi 69] A. I. Rusinov, “On the Theory of Gapless Superconductivity in Alloys Containing Paramagnetic Impurities”, Zh. Eksp. Teor. Fiz. Pisma Red. **56**, 2047 (1969). [JETP Lett. **29**, 1101 (1969)].

- [Ryu 10] S. Ryu, A. P. Schnyder, A. Furusaki, and A. W. W. Ludwig, “*Topological insulators and superconductors: tenfold way and dimensional hierarchy*”, *New J. Phys.* **12**, 065010–065010 (2010).
- [Saku 70] A. Sakurai, “*Comments on Superconductors with Magnetic Impurities*”, *Prog. Theor. Phys.* **44**, 1472–1476 (1970).
- [Saku 94] J. J. Sakurai. *Modern quantum mechanics; rev. ed.* Addison-Wesley, Reading, MA (1994).
- [Sato 17] M. Sato and Y. Ando, “*Topological superconductors: a review*”, *Rep. Prog. Phys.* **80**, 076501–076501 (2017).
- [Sau 10] J. D. Sau, R. M. Lutchyn, S. Tewari, and S. Das Sarma, “*Generic New Platform for Topological Quantum Computation Using Semiconductor Heterostructures*”, *Phys. Rev. Lett.* **104**, 040502 (2010).
- [Sau 12] J. D. Sau, S. Tewari, and S. Das Sarma, “*Experimental and materials considerations for the topological superconducting state in electron- and hole-doped semiconductors: Searching for non-Abelian Majorana modes in 1D nanowires and 2D heterostructures*”, *Phys. Rev. B* **85**, 064512 (2012).
- [Sbie 14] B. Sbierski, G. Pohl, E. J. Bergholtz, and P. W. Brouwer, “*Quantum Transport of Disordered Weyl Semimetals at the Nodal Point*”, *Phys. Rev. Lett.* **113**, 026602 (2014).
- [Sbie 16] B. Sbierski. *On disorder effects in topological insulators and semimetals.* PhD thesis, Freie Universität Berlin (2016).
- [Sche 16] M. Schechter, K. Flensberg, M. H. Christensen, B. M. Andersen, and J. Paaske, “*Self-organized topological superconductivity in a Yu-Shiba-Rusinov chain*”, *Phys. Rev. B* **93**, 140503 (2016).
- [Schr 67] J. R. Schrieffer, “*The Kondo Effect—The Link Between Magnetic and Non-magnetic Impurities in Metals?*”, *J. Appl. Phys.* **38**, 1143–1150 (1967).
- [Schw 86] K. Schwarz, “*CrO<sub>2</sub> predicted as a half-metallic ferromagnet*”, *J. Phys. F.* **16**, L211 (1986).
- [Seng 01] K. Sengupta, I. Žutić, H.-J. Kwon, V. M. Yakovenko, and S. das Sarma, “*Midgap edge states and pairing symmetry of quasi-one-dimensional organic superconductors*”, *Phys. Rev. B* **63**, 144531 (2001).
- [Shib 68] H. Shiba, “*Classical Spins in Superconductors*”, *Prog. Theor. Phys.* **40**, 435–451 (1968).
- [Sila 10] M. A. Silaev and G. E. Volovik, “*Topological Superfluid <sup>3</sup>He-B: Fermion Zero Modes on Interfaces and in the Vortex Core*”, *J. Low Temp. Phys.* **161**, 460–473 (2010).

- 
- [Son 06] Y.-W. Son, M. L. Cohen, and S. G. Louie, “*Half-metallic graphene nanoribbons*”, *Nature* **444**, 347–349 (2006).
- [Soum 02] S. Souma and A. Suzuki, “*Local density of states and scattering matrix in quasi-one-dimensional systems*”, *Phys. Rev. B* **65**, 115307 (2002).
- [Stan 11] T. D. Stanescu, R. M. Lutchyn, and S. Das Sarma, “*Majorana fermions in semiconductor nanowires*”, *Phys. Rev. B* **84**, 144522 (2011).
- [Stan 12] T. D. Stanescu, S. Tewari, J. D. Sau, and S. Das Sarma, “*To Close or Not to Close: The Fate of the Superconducting Gap Across the Topological Quantum Phase Transition in Majorana-Carrying Semiconductor Nanowires*”, *Phys. Rev. Lett.* **109**, 266402 (2012).
- [Stan 17] T. D. Stanescu and S. Das Sarma, “*Proximity-induced low-energy renormalization in hybrid semiconductor-superconductor Majorana structures*”, *Phys. Rev. B* **96**, 014510 (2017).
- [Stic 17] D. Sticlet, B. Nijholt, and A. Akhmerov, “*Robustness of Majorana bound states in the short-junction limit*”, *Phys. Rev. B* **95**, 115421 (2017).
- [Take 13] S. Takei, B. M. Fregoso, H.-Y. Hui, A. M. Lobos, and S. Das Sarma, “*Soft Superconducting Gap in Semiconductor Majorana Nanowires*”, *Phys. Rev. Lett.* **110**, 186803 (2013).
- [Thom 15] M. G. Thomas. *Theory of Nanoelectromechanical Systems: From Nanostructures to Molecules*. PhD thesis, Freie Universität Berlin (2015).
- [Thou 82] D. J. Thouless, M. Kohmoto, M. P. Nightingale, and M. den Nijs, “*Quantized Hall Conductance in a Two-Dimensional Periodic Potential*”, *Phys. Rev. Lett.* **49**, 405–408 (1982).
- [Vars 88] D. A. Varshalovich, A. N. Moskalev, and V. K. Khersonskii. *Quantum theory of angular momentum*. World scientific (1988).
- [Volo 03] G. Volovik. *The Universe in a Helium Droplet*. Clarendon Press ; Oxford University Press (2003).
- [Vurg 11] I. Vurgaftman, J. R. Meyer, and L. R. Ram-Mohan, “*Band parameters for III-V compound semiconductors and their alloys*”, *J. Appl. Phys.* **89**, 5815–5875 (2011).
- [Wepe 13] I. van Weperen, S. R. Plissard, E. P. A. M. Bakkers, S. M. Frolov, and L. P. Kouwenhoven, “*Quantized Conductance in an InSb Nanowire*”, *Nano Lett.* **13**, 387–391 (2013).
- [Will 12] J. R. Williams, A. J. Bestwick, P. Gallagher, S. S. Hong, Y. Cui, A. S. Bleich, J. G. Analytis, I. R. Fisher, and D. Goldhaber-Gordon, “*Unconventional Josephson Effect in Hybrid Superconductor-Topological Insulator Devices*”, *Phys. Rev. Lett.* **109**, 056803 (2012).

- [Wood 18] B. D. Woods, T. D. Stanescu, and S. Das Sarma, “*Effective theory approach to the Schrödinger-Poisson problem in semiconductor Majorana devices*”, Phys. Rev. B **98**, 035428 (2018).
- [Yao 14] N. Yao, L. Glazman, E. Demler, M. Lukin, and J. Sau, “*Enhanced Antiferromagnetic Exchange between Magnetic Impurities in a Superconducting Host*”, Phys. Rev. Lett. **113**, 087202 (2014).
- [Yazd 97] A. Yazdani, B. A. Jones, C. P. Lutz, M. F. Crommie, and D. M. Eigler, “*Probing the Local Effects of Magnetic Impurities on Superconductivity*”, Science **275**, 1767–1770 (1997).
- [Yu 65] L. Yu, “*Bound state in superconductors with paramagnetic impurities*”, Acta Phys. Sin. **21**, 75 (1965).
- [Zhan 18] H. Zhang, C.-X. Liu, S. Gazibegovic, D. Xu, J. A. Logan, G. Wang, N. van Loo, J. D. S. Bommer, M. W. A. de Moor, D. Car, R. L. M. Op het Veld, P. J. van Veldhoven, S. Koelling, M. A. Verheijen, M. Pendharkar, D. J. Pennachio, B. Shojaei, J. S. Lee, C. J. Palmstrøm, E. P. A. M. Bakkers, S. das Sarma, and L. P. Kouwenhoven, “*Quantized Majorana conductance*”, Nature **556**, 74 (2018).
- [Žitk 11] R. Žitko, O. Bodensiek, and T. Pruschke, “*Effects of magnetic anisotropy on the subgap excitations induced by quantum impurities in a superconducting host*”, Phys. Rev. B **83**, 054512 (2011).
- [Zyuz 13] A. A. Zyuzin, D. Rainis, J. Klinovaja, and D. Loss, “*Correlations between Majorana Fermions Through a Superconductor*”, Phys. Rev. Lett. **111**, 056802 (2013).

## Acknowledgements

I would like to thank both of my supervisors Piet W. Brouwer and Felix von Oppen for their patience and trust. I thank them for their support and encouragement to not forget the details, to explore new avenues, and to look for the big picture. I appreciate to have worked with two amazing physicists, who both have a strong intuition for physics, a quick mind, and who taught me how to tackle difficult problems, to think critically, and to solve problems.

I am very grateful to Felix for setting up contact with Gil Refael and giving me the great opportunity to stay and research at California Institute for Technology for a few months. I thank Gil Refael for enabling my stay, for the many discussions, and the many things that he taught me.

I thank Gabriele Herrmann and Marietta Wissmann for their amazing work. Together with Piet and Felix, I especially thank them for their dedication and the many hours that must have been spent when working contracts had to change.

My time at the Dahlem Center has been an amazing time. I thank my colleagues for the many discussions at the roof top, the board game evenings, our bouldering evenings, discussions about the many good and not so good things of python, the Volleyball games in the early days, and everything else. I will especially miss the swimming rounds at Finckensteinallee and Krumme Lanke. I thank Björn Sbierski, Christian Klöckner, Sergio Gonzalez, Max Hering, Elina Locane, Zhao Liu, Flore Kunst, Laura Baez, Max Geier, Max Trescher, Michele Filippone, Kevin Madsen, Jonas Sonnenschein, Christian Fräßdorf and Maresa Rieder.

I am thankful to my friends Fabian and Jens Merkle for their great support throughout the past years and for distracting me when my thoughts revolved too much around physics.

I am indebted to my whole family. Without them, my work would not have been possible.

Finally, I would like to thank Bettina, my better half, who went with me through day and night, and always finds the right words to keep my motivation high.



# Curriculum Vitae

Mein Lebenslauf wird aus Gründen des Datenschutzes in der elektronischen Fassung meiner Arbeit nicht veröffentlicht.



# Publications

List of publications that are a central part of this thesis:

- T. Kiendl, F. von Oppen, and P. W. Brouwer,  
"Renormalization effects in spin-polarized metallic wires proximitized by a superconductor: A scattering approach"  
arXiv:1809.08023 (2018)  
[Chapter 4.]  
The initial idea of the project was proposed by P. W. Brouwer and F. von Oppen. I contributed in performing the numerical and the majority of the analytical calculations, and creating the figures. I wrote the original manuscript, which was revised together with the co-authors.
- T. Kiendl, F. von Oppen, and P. W. Brouwer,  
"Proximity induced gap in nanowires with a thin superconducting coating"  
In preparation.  
[Chapter 5.]  
The initial idea of the project was proposed by P. W. Brouwer and F. von Oppen. I contributed in performing the analytical and numerical calculations, and creating the figures. I wrote the original manuscript, which was revised together with the co-authors.
- T. Kiendl, F. von Oppen, and P. W. Brouwer,  
"Effects of nonmagnetic disorder on the energy of Yu-Shiba-Rusinov states"  
Phys. Rev. B **96**, 134501 (2017)  
[Chapter 6.]  
The initial idea of the project was proposed by P. W. Brouwer and F. von Oppen. I contributed in performing the analytical and numerical calculations, and creating the figures. I wrote the original manuscript, which was revised together with the co-authors.

Other publications:

- T. Kiendl and F. Marquardt  
"Many-Particle Dephasing after a Quench"  
Phys. Rev. Lett. **118**, 130601 (2017)